Thesis

CHANNELLING INVESTIGATION OF THE BEHAVIOUR OF URANIA UNDER LOW-ENERGY ION IRRADIATION

presented by

Tien Hien NGUYEN

to fulfill the requirements for the grade of doctor in physics

at the

UNIVERSITY PARIS-SUD

in front of the jury comprising

President of jury:	Vincent JI	Professor, University Paris-Sud
Referees:	Nathalie MONCOFFRE	CNRS Research Director, IPNL Lyon
	Aurelio CLIMENT FONT	Professor, University Autonome Madrid, Spain
Examiners:	Pascal DANNUS	Professor INSTN, CEA Saclay
	Pierre DESGARDIN	CNRS Researcher, CEMHTI Orléans
Supervisor:	Frédérico GARRIDO	Professor, University Paris-Sud

Date of defence: December 05th, 2013

UNIVERSITÉ PARIS-SUD

ÉCOLE DOCTORALE MIPEGE

LABORATOIRE CSNSM

DISCIPLINE : PHYSIQUE

THÈSE DE DOCTORAT

Soutenue le 05 décembre 2013 par

Tien Hien NGUYEN

Étude par canalisation du comportement du dioxyde d'uranium irradié avec des ions de basse énergie

Directeur de thèse:	Frédérico GARRIDO	Professeur, Université Paris-Sud

Composition du jury:

Président du jury:	Vincent JI	Professeur, Université Paris-Sud
Rapporteurs:	Nathalie MONCOFFRE	Directrice de Recherche CNRS, IPNL de Lyon
	Aurelio CLIMENT FONT	Professeur, Université Autonome de Madrid
Examinateurs:	Pascal DANNUS	Professeur INSTN, CEA Saclay
	Pierre DESGARDIN	Chargé de Recherche CNRS, CEMHTI Orléans

Acknowledgments

First of all, I would like to express the most profound gratitude to my advisor Prof. Frédérico GARRIDO for the continuous support of my Ph.D study and research, for his patience, motivation, enthusiasm, and immense knowledge. His guidance helped me in all the time of research and writing of this thesis. Through my PhD, I am very much benefited from his guidance and knowledge. More important, he always has strong faith on students even long before they realize what they can really achieve. His vision on science always motivates me to explore more in the field. In every sense, none of this work would have been completed without him.

I am deeply grateful to Dr. Aurélien DEBELLE and research director, Dr. Lionel Thomé for their insightful suggestions, encouragement discussion and times. Dr. Aurélien DEBELLE answered many of my questions regarding the X-ray diffraction analysis, taught me how to use the techniques, explained me and helped me a lots in analysing the data. All these are invaluable not only for this thesis but also for my future career. Dr. Lionel THOMÉ was always available to answer any of my questions whether they concern the theory, the experimental technique or the results that I have. It is a huge pleasure for me to work with them. Their enthusiasm towards the research and kindness to people are something I really much long for.

I would like to address my sincere thank to Dr. Stamatis MYLONAS for his kind helps and interesting discussions with TEM images. He taught me how to polish a sample especially a so fragile material like uranium dioxide, and helped me a lots in recording these images.

Many thanks go to the JANNuS staffs for their kind assistance during my experiments. Special thanks are due to Cyril BACHELET, he has always managed to give me beam time to finish my experiments.

I thank the direction of the CSNSM laboratory for welcoming me in this laboratory, for helping me with the administrations during my time working at the laboratory and for giving me the opportunity to attend several conferences. I thank the high graduate school “MIPEGE” for the financial support for my thesis.

Last but not the least, I would like to thank my family, escpecially my parents for supporting me spiritually throughout my life. Thanks all my friends in Orsay, who have always been with me during my stay in France.

A big thank to whom I forgot to mention!

Abstract

This thesis is dedicated to the investigation of the structural destabilisation of UO_2 single crystal. Irradiations with 470-keV Xe, 500-keV Ce and 500-keV La ions (with corresponding ion range of $Rp \sim 85$ nm and range straggling of $\Delta Rp \sim 40$ nm according to SRIM calculation) have been performed to investigate the destabilisation of UO_2 single crystals induce by (i) the radiation damage effects due to the nuclear stopping process of a fission fragment at the end of their trajectories (ballistic contribution) and by (ii) the incorporation of a fission product at high concentration (chemical contribution). The energies and masses of bombarding ions were deliberately chosen so that they would have very similar projected range in UO_2 in order to compare the effects induced by solubles (La and Ce) versus non soluble Xe species in UO_2. Rutherford Backscattering Spectrometry in channelling geometry (RBS/C) was applied to study the defects induced. Channelling data were analysed afterwards by Monte-Carlo simulation with McChasy code assuming a two-class model of defects comprising (i) the randomly displaced atoms (RDA) and the bent channels (BC) defects. The accumulation of RDA with increasing ion fluence leads to a steep increase (build-up of defects) observed from 4 to 7 *dpa* regardless of nature of ions and a dramatic increase observed from 300 *dpa* (corresponding to ≥ 5 at. % of implanted ions) only for $Xe-$irradiated crystal. The difference due to the soluble versus insoluble species was clearly observed. Such a difference was observed *via* the dramatic increase of RDA when the crystal is implanted at very high concentration only for crystal implanted with insoluble species. Moreover, the difference is also observed *via* the higher fraction of RDA created in the crystal irradiated with insoluble element. This phenomenon is mostly due to the size of implanted species in the matrix. Insoluble Xe atoms have the atomic radius which is larger than twice the atomic radius of U sub-lattice while soluble La and Ce atoms have the atomic radii of similar size as compared to U atom. Xe creates a much stronger stress field in UO_2 crystal in comparison to La or Ce; a higher fraction of RDA is thus created. Conversely, the accumulation of BC with increasing ion fluence leads to very similar evolution versus ion fluence in all crystals implanted with the three elements. A regular increase of BC versus fluence which reveal the dramatic structural modification is observed. Such a modification is hidden according to the evolution of RDA.

Résumé

Cette thèse est consacrée à l'étude de la déstabilisation structurale du dioxyde d'uranium monocristallin. L'irradiation avec des ions Xe de 470 keV, Ce de 500 keV et La de 500 keV (correspondant à un parcours projeté $Rp \sim 85$ nm et à l'écart type $\Delta Rp \sim 40$ nm selon le code de calcul SRIM) ont été réalisées pour étudier la déstabilisation du monocristal, induit, d'une part, par la création de défauts dû au processus de ralentissement nucléaire des fragments de fission à la fin de leur parcours (contribution balistique), et, d'autre part, par l'incorporation de produits de fission à forte concentration (contribution chimique). L'énergie cinétique des éléments incorporés a été choisie de sorte que leurs parcours dans le solide soient identiques afin de comparer directement les effets induits par des espèces solubles (La et Ce) et insolubles (Xe) dans le dioxyde d'uranium. La Spectrométrie de Rétrodiffusion Rutherford en canalisation (RBS/C) a été appliquée pour caractériser et quantifier les défauts générés par l'irradiation. Les données ont été analysées par simulation Monte-Carlo en considérant un modèle original comportant de deux-type de défauts (i) des atomes aléatoirement déplacés dans le cristal (RDA) et (ii) des distorsions des rangés atomiques (BC). L'accumulation de la fraction d'atomes déplacés RDA avec l'augmentation de la fluence conduit à une forte augmentation du nombre de défauts observé entre 4 et 7 *dpa*, indépendamment de la nature des ions. Une seconde augmentation spectaculaire est observée à partir de 300 *dpa* (correspondant à une concentration excédant 5 % atomique d'ions implantés) pour le cas spécifique des cristaux irradiés avec des ions Xe. Un comportement différentié est clairement observé pour les espèces solubles par rapport à leurs homologues insolubles. Cette différence se traduit d'une part par l'augmentation spectaculaire de RDA lorsque le cristal est implanté à très haute concentration dans le cas d'espèce insolubles, et, d'autre part, par un endommagement plus prononcé entre 7 et 300 *dpa*. Ce phénomène est notamment la conséquence des différences de taille entre les rayons atomiques de La et de Ce, très inférieure à celles du Xe. A contrario, l'accumulation de défauts de type distorsion des rangées atomiques BC avec l'augmentation de la fluence conduit à une évolution très similaire quelle que soit la nature de l'élément incorporé. Cette augmentation se produit principalement entre 10 et 100 *dpa* - correspondant à un plateau pour l'évolution des défauts de type RDA - et traduit une importante évolution structurale du dioxyde d'uranium irradié, explorée pour la première fois dans ce travail de thèse.

Contents

Introduction **3**

1 Radiation effects on materials for nuclear energy **9**

1.1 Materials for nuclear energy 9

1.1.1 Urania 10

1.1.2 Zirconia 11

1.1.3 Spinel 12

1.2 Radiation effects on ceramic materials 14

1.2.1 Ions-materials interaction: processes at the atomic scale 14

1.2.2 The stopping power 18

1.2.3 Radiation induced defects 21

1.2.4 Behaviour of ceramics under irradiation 25

2 Methodology **41**

2.1 Experimental simulation of the radiation effects in nuclear fuel 41

2.2 Samples preparation 42

2.3 Experiments 42

2.4 Techniques for characterisation 44

2.4.1 Rutherford Backscattering Spectrometry 44

2.4.2 X-Ray diffraction 48

2.4.3 Transmission Electron Microscopy 53

2.5 Computer tool 55

2.5.1 Principle of Monte-Carlo simulation of channelling phenomenon . . 56

2.5.2 McChasy 57

3 Irradiation effects on the urania structure **59**

3.1 Irradiation with noble gas ions . . . 59
3.2 Irradiation with lanthanide ions (La and Ce) . . . 67
3.3 Microstructural evolution under irradiation . . . 73
3.4 TEM observation of the radiation damage . . . 80
3.5 Summary . . . 85

4 Towards an advanced description of the evolution of the urania structure under irradiation: a two-defect class model 87

4.1 Description of the model of defects . . . 88
4.2 Simulation of axial channelling spectra by Monte-Carlo . . . 90
4.2.1 Definition of the structural parameters . . . 90
4.2.2 The role played by randomly displaced atoms (RDA) to channelling spectra . . . 91
4.2.3 The role played by the bent channel (BC) class of defects . . . 93
4.2.4 Monte Carlo simulations with the complete model of defects: RDA- and BC-type . . . 96
4.3 Damage evolution . . . 98
4.3.1 Analysis of channelling spectra . . . 98
4.3.2 Evolution of the randomly displaced atoms defects . . . 102
4.3.3 Evolution of the bent channels defects . . . 108
4.3.4 Choice of BC parameters, choice of L and η . . . 109
4.3.5 Estimation of uncertainties in the fraction of RDA and BC type defects . . . 111
4.3.6 Kinetics of damage accumulation . . . 112
4.4 General discussion . . . 117

Conclusions and perspectives 127

Introduction

Nuclear energy, as for over 50 year, has proved to be one of the most important and the most used $non - CO_2$ energy source for the human being. During that period, many types of nuclear fuels making use of Uranium fissile isotope (^{235}U) were studied and used as the main fuel material in the majority of the commercial nuclear reactors all over the world.

At the present time, there are over 400 nuclear reactors in operation all over the world which provide a non-negligible contribution of about 14 % of the world's electricity. Moreover, the nuclear energy continues to be the first choice of new energy resources in the future especially when the fossil fuels are coming to an end. According to the recent report on application of nuclear source for generating electricity of IAEA,[1] about 60 reactors are under construction and about 20 countries plan for nuclear power programs.

As the world's population is increasing the consumption of energy and electricity increases. In addition, the worldwide development of industry necessitates an increase in production of the electricity. Because of that, scientists all over the world have to search for every available sources of energy so as to meet the demand of not only the energy (in general) but also the need of electricity for the global development. Therefore, energy and particularly electricity always presents as one the biggest challenges to the mankind that force the scientific community to look for all possible sources of energy and electricity for the world's development amongst which nuclear energy is still the most promising candidate.

During the last 50 year, nuclear energy has been intensively used in nuclear reactors for the purpose of generating electricity all over the world. During that time, many types of nuclear reactor technologies have been studied, tested and applied. At the present time, the pressurized water reactor (PWR) - the nuclear reactor of generation II - presents as the most used nuclear reactor type. This technology, which has been widely used with great success, uses UOX[2] and MOX[3] fuels as the heat source for driving the electrical generator's turbine. However, due to the strict regulation on the safety and due to the economical requirements, the new generation of advanced nuclear reactors (generation III and IV) that are safer and more powerful are being developed. Along with the appearances of nuclear reactors generation III and IV, scientist has to come back to the research on the nuclear fuel so as to find out the advanced fuel that can be used in these newly

[1] International Atomic Energy Agency
[2] Fuel made of uranium dioxide UO_2 (Uranium Oxide)
[3] Fuel made of the mixture UO_2 and PuO_2, $(U, Pu)O_2$ (Mixed Oxide)

designed reactors. In particular, the problem arises in the nuclear reactor generation IV where fast neutrons at high flux are used for the two purposes: (i) fast neutrons are used to trigger the fragmentation of fissile isotopes so as to generate heat sources and to produce secondary neutrons in a chain fission reaction and (ii) they are also used in the second application in order to transform fertile into fissile isotopes via the neutron capture reaction followed by the β^- emissions, e.g. $^{238}U(n, 2\beta^-)^{239}Pu$. With the presence of neutron at high flux, the fuel is submitted to an extremely deleterious environment where continuous bombardments by neutrons, fission fragments, alpha particles and heavy recoil nuclei lead to the strong destabilisation of the fuel's structure. In addition, in the new generation of nuclear reactor, the aim is not only to increase the safety of the reactor but also to increase the burn-up[4] so as to increase the production of electricity for economical purposes. The increase of burn-up leads to the increase of number of energetic fission fragments created which consequently gives more contribution to the irradiation damaging sources to the fuel structure. Moreover, due to the long time operation, the fuel is literally poisoned by the created fission products (FP). The incorporation of the FP modifies the chemical composition of genuine fuel, which eventually changes the physical and mechanical properties (thermal conductivity, structural stability, hardness...) of the fuel. Finding new form of nuclear fuel that possesses high stability and resistance to irradiation and possesses a high capability of accommodating large fraction of FP is therefore one crucial challenge to the application of future generation of nuclear reactor.

Besides the success of the nuclear industry, the nuclear security issue still remains as one of the biggest challenges to mankind. Over the time, human has witnessed several disasters due to the failure of a nuclear facility. Those disasters caused thousands of death (direct effect) and hundred thousands of severe diseases years latter (indirect effect). Along with the effects on people's healths, the release of radioactive materials leads to the abandon of a wide area and destroys the entire environments within. Learning from those disasters, many researches have been being conducted in order to minimize the risk of a nuclear accident in which the research on the nuclear fuel is one important subject.

As stated here before, the stability of the fuel is affected principally by two elements: (i) the radiation effects and (ii) the incorporation of impurities leading to the modification of the chemical composition. Nuclear fuel figures a quite rich source of radioactive radiations including the high flux neutron particles, the created fission fragments, the alpha particles and heavy recoil nuclei (daughter nuclei produced in a disintegration of Uranium atom and minor actinides). The fuel materials themselves figure as non-negligible source of radiation because they are radioactive element with long half-life of millions of

[4]Burn-up is measured as the percentage of fuel atoms that have undergone fission reaction in unit of %FIMA (fissions per initial metal atom) and/or as the actual energy released per mass of initial fuel in gigawatt-days/metric ton of heavy metal (GWd/tHM)

years. In operation, after capturing a neutron (thermal neutron in thermal reactor or fast neutron in fast reactor), fissile isotope of U in UOX fuel or U and Pu in MOX fuel fission and give birth to two fission fragments and gamma radiation (one of radioactive radiation) and some neutrons along with. The fission fragments are, in general, unstable nuclei. This means that they are radioactive, they decay (or follow a chain decays) and emit α, β^- or energetic γ radiations and finally become stable elements (known as fission products).

Not only fission fragments presenting as sources of radiation in nuclear fuel, minor actinides are also found as part of the radioactive sources. During operation, ^{238}U isotope captures one neutron and does not pass afterwards a fission. It becomes ^{239}U which is unstable and β^- radioactive with half-life of 23.47 minutes. It emits quickly one β^- particle and becomes ^{239}Np or it can otherwise capture one more neutron to become ^{240}U which is another β^- radioactive isotope with half-life of 14.1 hours. ^{239}Np and ^{240}Np (daughter nuclei of ^{239}U and ^{240}U) are themselves β^- radioactive nuclei. They emit one β^- particle to become Pu isotopes. The chain of neutron capturing and β^- decays continue and a series of minor actinides (Am, Cm, ...) nuclei are produced (see the figure below). Those minor actinides are also long-live sources of α radiation that lead to the storage of nuclear waste to thousands of year before reaching the normal level of radioactive radiation.

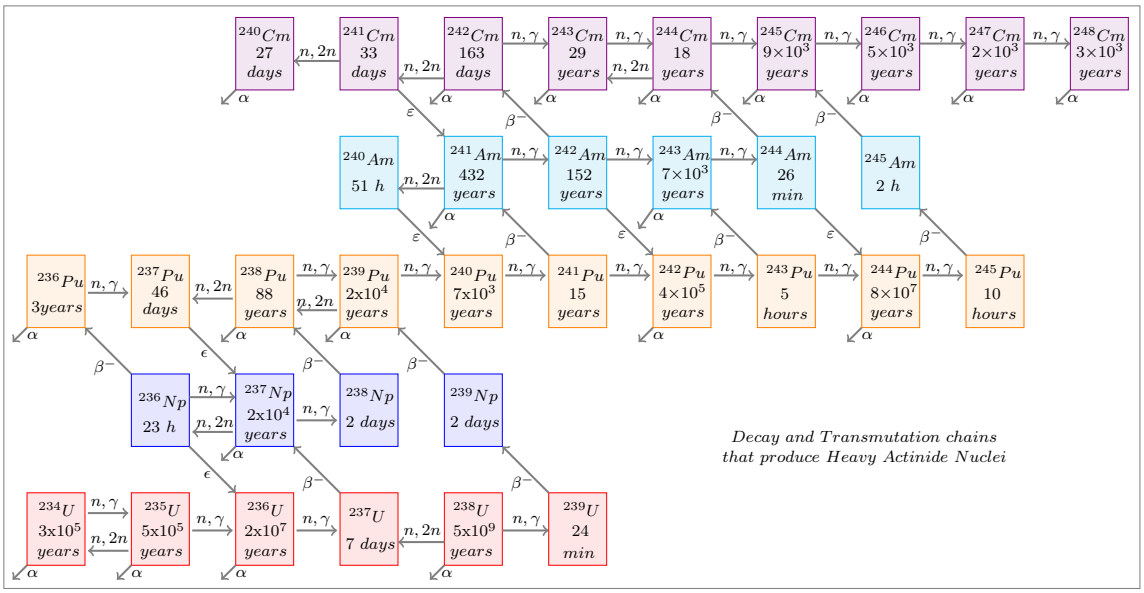

Decays and transmutation chains that produce minor actinides

Beside fission products, α and β particles, there is a non-negligible amount of uncharged particle radiation in the nuclear reactor core: neutron, gamma radiation and neutrino. Every fission reaction results in the production of 2 fission fragments of typical energy in between 70 to 100 MeV. Also, an average of 2.5 free neutrons are emitted

along with the two fission fragments. Each of them has the energy of $\sim 2\ MeV$ (total of $\sim 4.8\ MeV$). This fission reaction also releases about $7\ MeV$ in prompt gamma radiation. In operation, the flux of neutron particles varies (due to the reactor controlling action to meet the demand) around $10^{14}\ cm^{-2}s^{-1}$ which gives a high level of neutron radiation over whole life time of a reactor core. Every atom that make up the reactor vessel displace twice in average due to the bombardment of neutron radiation. All the concerning information around one fission reaction confirm the fact that nuclear fuel is of the highest level of radioactive radiations.

Since nuclear fuel is submitted to such a rich source of radioactive radiations, its structure will therefore be affected. A thorough investigation of its structural stabilisation due to (i) the radiation effect and (ii) the modification of the chemical composition of the genuine fuel is necessary to understand the stability of fuel in this environment so as to help finding out the suitable fuel for the new generation of nuclear reactors. Knowledge of the fundamental process plays an important role and hence in this work, we investigate the fundamental mechanism of the fuel's structural destabilisation due to both the radiation and chemical contribution

Investigating the nuclear real fuel taken out from a nuclear reactor core presents as a big challenge to scientist since it requires a lot of special safety conditions as well as special equipment. Experiments on the real fuel are difficult to perform and interpret because of the high radioactivity and because of the mixing of the various contributions coming from the several radiation sources (e.g. neutrons, gamma and fission fragments). Conversely, the use of external beams of mono-energetic ions allows one to perform screening studies in well-defined conditions (choice of ions, energy, fluence, flux, temperature of sample, etc). In this work, the destabilisation of UO_2 single crystals due to the irradiation and due to the incorporation of foreign elements is investigated as a model system to the real fuel. Moreover, by using specified ion, the modification of the chemical composition (leading to the modification of chemical and physical properties of nuclear fuel) due to the incorporation of an impurity will be parallelly investigated. The results obtained from this work are not going to be the complete knowledge but will be useful to explain the structural modification of nuclear fuel submitted to the bombardment of high neutron flux and of internal radiation (energetic fission products).

This thesis will therefore be organised in the following 4-chapter structure. In the first chapter, introductions will be given to the materials that can be used in the nuclear industry that have to submit to the high irradiation environments . These material can be used as the fuel, potential matrix for incinerating long-live isotopes and waste storage matrix. Afterwards, the theory of the interaction between a charged particles with material will be discussed. The processes of creation of defect due to this interaction will

be made clear and then a bibliography on investigations of the radiation effects on these material will be summarised. The second chapter discusses in details the experiments and experimental techniques applied to characterise the irradiated crystalline structure. The third chapter presents the results of the experiments concerning the investigations of the structural modification of uranium dioxide single crystal under irradiation. Chapter 4 discusses the measurement of the radiation effects on UO_2 single crystal by the channelling technique where the data are analysed in more details with the help of Monte-Carlo simulation. The discussion to the whole picture about the investigation of the destabilisation of the UO_2 single crystal submitted to irradiation made in this work will be rised. The thesis ends with the conclusion to this work and future orientation for further investigation.

Chapter 1

Radiation effects on materials for nuclear energy

This chapter gives some descriptions of materials used for nuclear industry in which oxide-based materials such as urania, zirconia (ceramics of fluorite-type structure) and magnesium spinel will be mentioned and analyzed as examples of investigated materials. To explain the radiation-induced effects, the fundamental (physical) processes occurring at atomic scale when bombarding a solid by a charged particle will be discussed. In the end, the chapter presents a summary of investigation on the behaviour of a solid's structure submitted to the irradiation of an ion beam (process of reorganization of defects and the structural transformation).

1.1 Materials for nuclear energy

Materials used for nuclear energy production refer not only to the nuclear fuel but also other materials for the claddings, the reactor vessels, the inert matrix for transmutation of minor actinides that are created during operation and for storage of nuclear wastes and other equipments. Amongst them, the choices for the fuel, cladding, reactor vessel and storage matrix seem to be the most important because those materials have to bear an extremely high irradiation condition during their life time in operation and in long-term storage.

Many classes of materials were investigated and applied into the commercial market depending on the varieties types and on different generations of nuclear reactors. Fuels of oxide-based materials such as UOX and MOX are basically used in PWR (the most popular nuclear reactor - Generation II). Other carbide or nitride based materials are being investigated for the application as advanced fuels in the future reactors (Generation III and IV). Stainless steel and zirconium based alloys are both investigated and used as fuel cladding but zirconium based alloy (zircaloy) is mostly used in the present generation of nuclear reactor since they are transparent to neutrons. As for transmutation matrices and for long time storage containers, other ceramics such as Yttria Stabilized Zirconia (YSZ) and magnesia spinel ($MgAl_2O_4$) are currently investigated as potential candidate since they possess a high resistance to radiation and a high capability of accommodating

a large fraction of radioactive elements. However, even though being studied for a long time these material need to be carefully investigated for final application.

1.1.1 Urania

Amongst the possible materials, ceramic materials for instance, the oxide-based ceramics (such as UO_2, ZrO_2) figure the most popular for nuclear energy production. Uranium dioxide exhibits a fluorite-type crystalline structure in which uranium atoms form a *fcc* structure with uranium atoms occupy the 8 vertices and 6 centres of the cube [1]. Urania is used mainly as nuclear fuel for fuel rods in nuclear reactors, specifically as UO_2 (UOX) or as a mixture of UO_2 and PuO_2 (plutonium dioxide). $(U, Pu)O_2$ is called a mixed oxide (MOX fuel) in which PuO_2 exhibits the same fluorite-type structure and the mixture $(U, Pu)O_2$ also exhibits the fluorite-type structure. UO_2 is used as nuclear fuel since it possesses several relevant properties such as a high melting temperature (see table 1.1) and a high resistance to irradiation. Moreover, UO_2 also emerges as a good "trap" of fission products and minor actinides. During operations, a certain amount of fission products and minor actinides are produced. Those elements are mostly highly radioactive and chemically toxic. But thanks to the UO_2, those elements are confined within the crystalline structure of UO_2 without being released. Though having very interesting aforementioned characteristics, UO_2 still has some disadvantages as being the choice for fuel. The first disadvantage is that its thermal conductivity is low and this leads to the high gradient of temperature of the fuel pin. The temperature of the fuel pellet is always higher at the center than the edge ($\Delta T \sim 600°\text{C}$ from the center to the surface of the fuel pellet). This difference in temperature could result in the destruction of the fuel pellet and hence the fuel rod. Another disadvantage of Urania is that it is not stable in a rich-oxygen environment. Urania quickly interacts with oxygen and becomes U_4O_9, U_3O_7 or U_3O_8 giving the risk of destroying the UO_2 structure. To avoid the contact of UO_2 with oxygen in a reactor, the fuel rod are usually filled with Helium gas at typical pressure of 20 $bars$. Inside the reactor, uranium dioxide is used in a sintered form in which it has been sintered into a pellet of dimension $0,82$ cm in diameter and $1,3$ cm in height (as in French reactor). Beside that most valuable application, depleted UO_2 (DUO_2) can also be used as a material for radiation shielding due to the high atomic number.

Apart from uranium, plutonium (created during operation by the neutron capture reaction of uranium followed by the β^- emissions) can be as well used as nuclear fuel. But the risk of the proliferation requires that the plutonium produced has to be burned (incinerated or consumed) for electricity generating (peaceful) purposes. In order to consume the plutonium, MOX fuel has been used as one of the alternative solutions. But the used of the MOX fuel has its own disadvantages. It can help using plutonium as one of the fissile isotopes for the fission reaction but an equivalent amount of plutonium

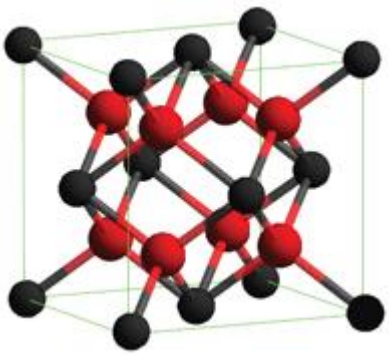

Figure 1-1: Uranium dioxide crystal with uranium atoms located at fcc positions (black) and oxygen atoms located at tetrahedral positions (red).

can be reproduced again since there is uranium in the fuel. This means that the amount of plutonium stays almost unchanged. To solve the problem, several other materials have been investigated to be used as the host transmutation matrices. Those transmutation matrices are used so that they can keep plutonium inside the matrix to be burned without being recreated. Among the potential candidates used as transmutation matrix, Zirconia and Spinel are two of the most promising.

1.1.2 Zirconia

Zirconium dioxide or Zirconia (ZrO_2) is found in natural form of rare baddeleyite mineral but it is mostly produced from zirconium silicates sand ($ZrSiO_4$) by thermal treatment at high temperature followed by chemical treatment. Zirconia has high melting temperature and a low thermal conductivity (see table 1.1). Pure zirconia undergoes two crystallographic transformations between room temperature and its melting point: monoclinic to tetragonal at roughly 1170°C and tetragonal to cubic at about 2370°C. The volume changes associated with these transformations are sufficiently high so that the thermal deviations through the transformations tend to break objects made of pure zirconia and that makes it quite impossible to be used in many applications. The high-temperature tetragonal and cubic forms can be stabilized with a variety of oxide additions (dopant) such as CaO, MgO, TiO_2, Y_2O_3... For instance, doping Yttria allows the zirconia to be stabilized in the cubic form in a large domain of composition and temperature. Once the process completes, a FSZ (Fully Stabilized Zirconia) is obtained. Yttria-dopped zirconia gives the YSZ - "Yttria Stabilized Zirconia" which exibits an oxygen-deficient fluorite-type structure. The zirconium and yttrium atoms are located in an *fcc* lattice, i.e., at the corners of the cubic elementary cell as well as at the halves of the $\langle 110 \rangle$ directions. Oxygen atoms lie at the quarters of $\langle 111 \rangle$ directions. The structure obeys the $P\bar{4}3m$ space group. The doping of Y_2O_3 into ZrO_2 consist of the substitution of Zr^{4+} cations by a Y^{3+} cation. For conserving the electro-neutrality of the crystal, this substitution results

Molecular formula	UO_2 [2, 3, 4, 5, 6]	ZrO_2 [7, 8, 9]	$MgAl_2O_4$ [10, 11, 12, 13]
Molar mass ($g.mol^{-1}$)	270.03	223.218	142.27
Density ($g.cm^{-3}$)			
Solid state	10.96	5.68	3.64
Liquid state	9.6		
Melting temperature (K)	3140	2988	2408
Thermal conductivity $W/m.K$			
Solid state (298 K)	8.89	2.3 to 3	2.7
Liquid state	2.5		
Specific heat C_p ($J/kg.K$)			
298 (K)	230	420 to 540	$\sim$ 857
2500 (K)	500		
3000 (K)	650		
4000 (K)	310		
6000 (K)	360		
8000 (K)	460		
Latent heat of fusion (kJ/kg)	289	700 to 820	
Latent heat of vaporization (kJ/kg)	1990		
Crystal structure	Cubic $Fm\bar{3}m$	Cubic $Fm\bar{3}m$	Cubic $Fd\bar{3}m$
Cell parameter (pm)	547	509	808.3
Displacement threshold energy (eV)	$E_d(U) = 40$ $E_d(O) = 20$	$E_d(Zr) = 40$ $E_d(O) = 40$	$E_d(Mg) = 30$ $E_d(Al) = 30$ $E_d(O) = 60$

Table 1.1: Some selected physical properties.

in the formation of an oxygen vacancy. The concentration of the oxygen vacancy is fixed by the doping fraction. The actual chemical composition of YSZ is hence $Y_xZr_{1-x}O_{2-x/2}$. The relevant phase diagram is shown in figure 1-2. According to the diagram, cubic zirconium dioxide exists down to room temperatures when the concentration of yttria is higher than 8 mol %. In the nuclear industry, YSZ is a good candidate for inert matrix for transmutation due to its high radiation resistance and the ability to confine radio-toxic elements.

1.1.3 Spinel

Magnesium aluminate spinel or magnesia spinel ($MgAl_2O_4$) is a member of the spinel family of general chemical composition AB_2X_4 in which A and B are suitable combination of respectively the 2+, 3+ or 4+ cations and X is an anion such as O, S, Se or Te [15]. Its crystalline structure is formed by the stacking of 8 cubic fcc arrays of O^{2-} in which Mg^{2+} cations occupy 1/8 of the tetrahedral sites and Al^{3+} cations occupy 1/2 of the octahedral sites (there are 64 tetrahedral sites and 32 octahedral sites present in a unit cell) [16]. The spinel structure is classified into normal structure, inverse structure and partially inverse structure following the occupation of those tetrahedral and octahedral sites. In a normal spinel structure, Mg^{2+} occupies the tetrahedral sites while Al^{3+} occupies the octahedral sites. In an inverse spinel structure, half of Al^{3+} cations occupy the tetrahedral sites and all the Mg^{2+} cations move to the octahedral positions. In a partially inverse case, some of Al^{3+} cations moves to the tetrahedral positions while the same number of Mg^{2+}

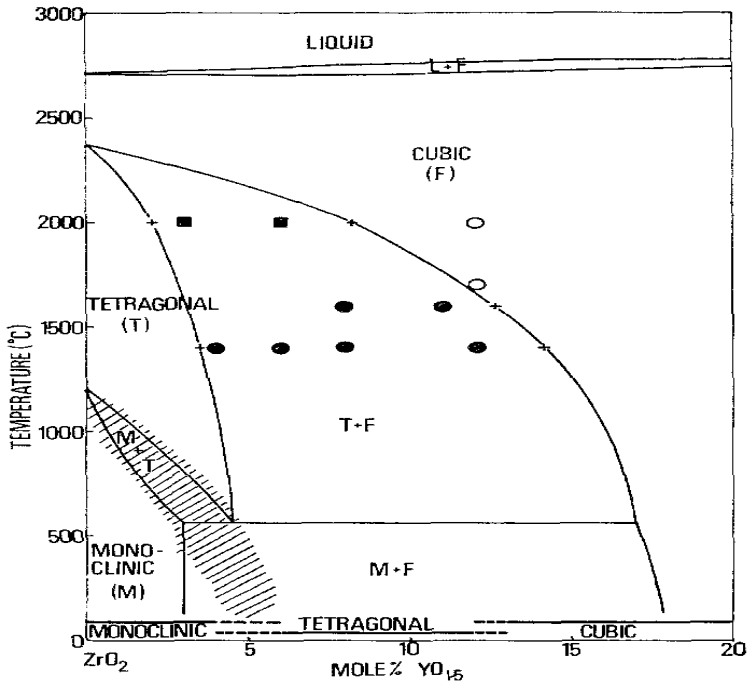

Figure 1-2: Equilibrium diagram of zirconia [14].

cations moves to octahedral positions. To characterize for a partially inverse structure the inversion parameter i, which represents the fraction of Al^{3+} cations in tetrahedral sites, is used. The structure formula for a partially inverse magnesia spinel ($MgAl_2O_4$) may be then written as:

$$[Mg^{2+}_{1-i}Al^{3+}_{i}]^{tetra}[Mg^{2+}_{i}Al^{3+}_{2-i}]^{octa}O_4[15]$$

The first square bracket represents the mean occupancy of tetrahedral sites while the second one represents the mean occupancy of octahedral sites by Mg^{2+} cations. For a normal spinel, $i = 0$; in a spinel where cations arrange randomly, $i = 2/3$, and for a total inverse spinel, $i = 1$. The crystalline structure spinel of obeys the $Fd\bar{3}m$ space group. Mg^{2+} cations occupy $8a$ Wyckoff positions, while Al^{3+} cations occupy $16d$ sites. The O^{2-} anions are displaced from ideal $48f$ sites in $\langle 111 \rangle$ directions away from the tetrahedral Mg^{2+} cations and towards the Al^{3+} cations [16, 17].

The natural sources of spinel have never been discovered, therefore spinel has to be produced synthetically [18]. There exists two main methods to produce spinel: sintering and fusion. Synthesis is made either in a vertical furnace for sintered spinel or in an electric arc furnace for fusion. Each of the two method has its own advantages. Sintering is a continuous process with controlled feed-rate and homogeneous temperature distribution in the furnace and this leads to a very homogeneous product with crystal sizes of $30 - 80$ μm. On the other hand, spinel synthesized by fusion is often produced in a batch. For obtaining a large ingot, an extended cooling time is required which results in the inhomogeneities in micro-structure. At the outside, spinel crystals are smaller due to the faster

cooling. In the center, the impurities are concentrated due to the lowest melting point. Thus, homogeneous fused spinel can only be made by very careful process. Magnesia spinel possesses some excellent chemical properties, i.e., high chemical inertness, thermal, dielectrical, mechanical and optical properties. Along with the above properties, it has the high melting temperature, high chemical inertness as well as the good thermal shock resistance that makes it a good usability in radio-technical applications.

1.2 Radiation effects on ceramic materials

This section discusses the interactions between a charged particle with materials and the possible defects created when a charged particle travels through the materials. First of all, the main interactions between ion and a solid (consequently the process of transferring energy from ion to a solid including the nuclei and orbital electrons) will be first mentioned. The notation of *"Stopping power"*[1] will be then defined as the quantity characterizing for the energy transferred of interaction between ion and materials: the quantity which represents the energy loss of ion per unit of materials' thickness traversed. Finally, the process of creation of randomly displaced atom defect and vacancy (Frenkel pair), and then the reorganization into extended defects, dislocation loop, grain division, ion track... resulting from the passing of an ion will be discussed.

1.2.1 Ions-materials interaction: processes at the atomic scale

Charged particles refer to ions (heavy charged particles), electrons or positrons and other particles. All the mentioned particles cause their own effects while travelling through a solid but this research focuses only on the effects of ion irradiation on materials since ions are of the most deleterious cause to the materials' structure (while the effects of other charged particles are almost negligible). For that reason, the concept of "charged particle" mentioned in this section could be restricted to the notation of "ion" only.

Physically, charged particles interact with materials by two interactions: inelastic (electronic) and elastic (nuclear) interactions. The former one refers to the continuous coulomb interaction of ions with the orbital electrons surrounding the nucleus while the latter one refers to the nuclear collisions with the atomic nuclei. When interacting with materials, ion loses part of its energy by collision and hence slows down inside the materials. Depending upon its energy (or its velocity), the interactions of charged particles with a solid differs. At high energy, the inelastic interaction is dominant while at low energy the elastic interaction is dominant. Due to interactions with a solid, charged particles lose part of the initial energy and slow down and finally stop inside a solid. The energy loss in the inelastic interaction is due to interaction with the electrons via electronic processes

[1] Usually used in literature but has the nature of a stopping force.

such as the excitation or the ionization an atom or electronic capture. In an elastic interaction, the energy loss is due to the ballistic collision with the atomic nucleus. The two interactions both result in the loss of energy of charged particles but at different rates with different mechanisms. The energy loss due to electronic collision is continuous through the presence of the electrical fields created by both ion and atoms (mostly the electronic cloud) whilst that due to nuclear collision is not continuous because it happens only when ion gets close enough to the atomic nucleus. For an energetic particle ($\sim 100\ MeV$), the major part of energy loss is due to the electronic interaction (about 90 %).

The elastic collision

The basic assumptions of elastic collisions are the conservation of kinetic energy and momentum of the system. Suppose that we have two particles, particle 1 having the mass m_1 moves at velocity $\overrightarrow{v}$ towards particle 2 having the mass m_2 at rest (as in the usual situation of irradiating a material, the ions move and the sample is supposed to be a target at rest).[2] After collision, m_1 moves at velocity v_1, in the direction making an angle θ with the incident direction; while m_2 moves at velocity v_2, in the direction forming an angle φ with the incident direction.

Applying the laws of conservation of kinetic energy and momentum to the system of elastic collision between two bodies, we have:

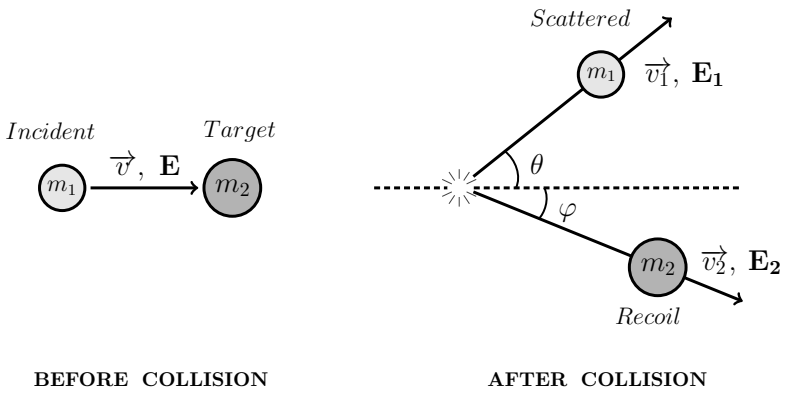

Figure 1-3: Schematic drawing of the two-bodies elastic collision.

$$E_{sys} = E_1 + E_2 = \frac{m_1 v^2}{2} + 0 = E_1' + E_2' = \frac{m_1 v_1^2}{2} + \frac{m_2 v_2^2}{2} \tag{1.1}$$

$$\overrightarrow{P_{sys}} = \overrightarrow{P_1} + \overrightarrow{P_2} = m_1 \overrightarrow{v} + \overrightarrow{0} = \overrightarrow{P_1'} + \overrightarrow{P_2'} = m_1 \overrightarrow{v_1} + m_2 \overrightarrow{v_2} \tag{1.2}$$

In projected form on the inter-bodies axis direction and on the direction perpendic-

[2]The thermal vibration of atoms is assumed to be negligible compared to the velocity of ions

ular to the inter-bodies axis, the conservation of momentum is written:

$$m_1 v = m_1 v_1 \cos\theta + m_2 v_2 \cos\varphi$$

and

$$m_1 v_1 \sin\theta = m_2 v_2 \sin\varphi$$

Supposing that T is the energy transferred from m_1 to m_2, by solving the system of equations (1.1) and (1.2) we finally obtain the expression of energy transferred in a binary elastic collision:

$$T(\varphi) = \frac{4m_1 m_2}{(m_1+m_2)^2} \frac{m_1 v^2}{2} \cos^2(\varphi)$$

or

$$T(\varphi) = \frac{4m_1 m_2}{(m_1+m_2)^2} E_1 \cos^2(\varphi)$$

and the maximum energy transferred is given by:

$$T_{max} = \frac{4m_1 m_2}{(m_1+m_2)^2} E_1 \tag{1.3}$$

After transferring part of energy to the target, the incident ion slows down and the energy left is expressed as:

$$E_1' = E_1 - T = K \cdot E_1$$

in which K is called the kinematic factor of the collision.

$$K = \left[\frac{\left(m_2^2 - m_1^2 \sin^2\theta\right)^{1/2} + m_1 \cos\theta}{m_1 + m_2} \right]^2 \tag{1.4}$$

In a special case in which the interacting angle $\varphi = 0$, the energy transferred from the incident ion to the target is maximum (T_{max}). If $m_1 < m_2$, the collision with angle $\varphi = 0$ results in the backscattering of incident ion. If $m_1 = m_2$ the transfer of kinetic energy is maximum and if $m_1 > m_2$ the incident ion will only scatter in the area with $\varphi \leq 90°$. Finally, in case that $m_1 \gg m_2$, the energy transferred is very small and is negligible. This is the case of collision between ion and an electron. The energy transferred to electron is so small and becomes negligible so that the collision between ion and atom at low energy is usually considered as a binary elastic collision.

Figure 1-4 shows the ratio of maximum energy transferred over the initial energy of the projectile as a function of the ratio of the masses of colliding partners. The maximum of energy transferred becomes higher if the mass of the projectile gets closer to the mass of target atom. When the mass of the projectile equals the mass of the target the maximum

of energy transferred reaches 100 %. In this condition, the projectile can lose all of it energy by a single collision with the target atom.

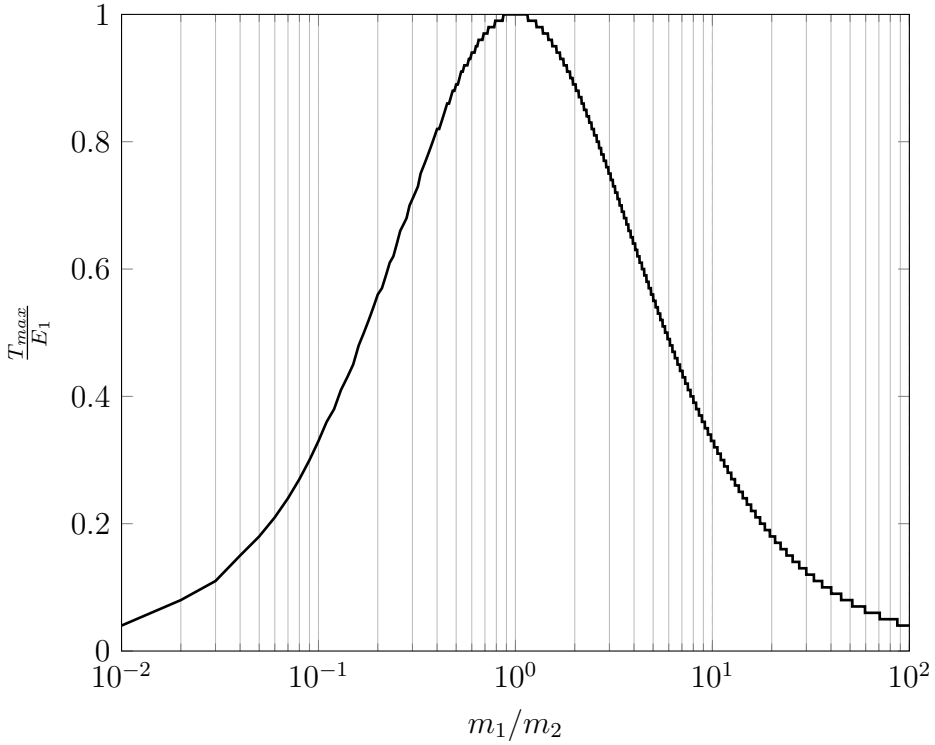

Figure 1-4: Maximum energy transferred versus m_1/m_2.

The inelastic collision

The inelastic collision refers to the Coulomb interactions between ion (nucleus and surrounding electrons) with the solid (the cloud of electrons and the nuclei). It is a complex process due to the accumulation of attractive (ion-electron) and repulsive (ion-ion or electron-electron) forces. Unlike the elastic collision, the internal energy of colliding parters may change as well and so the kinetic energy of a collision system does not conserve in an inelastic collision.

Once entering into a solid, charged particles interact immediately and simultaneously with many electrons. In such single interaction, the electron "feels" the attractive Coulomb force as the particle passes by the electron's vicinity. Depending on the distance of interaction, this attractive Coulomb force may be sufficient to either raise the electron to a high shell level (*excitation*) or kick it completely off from the atom (*ionization*). The energy that has been transferred to the electron originates from the particle and therefore the particle decelerates as a result of the interaction. This amount of energy transferred is very small in a single interaction compared to the initial energy. The primary particle must lose its energy in many such interactions during its passage in the solid. At any time, the particle interacts with many electrons and decelerates continuously until the particle is stopped.

Evolution of the charge state of moving ion

While crossing a solid, the population of the surrounding electrons of an ion varies depending on its velocity. This change in the electronic population results in the modification of the equilibrium charge state of ion and therefore it affects the electronic interactions of ion along its path [19].

Practically, the slowing down process of ion can be divided into three velocity domains with respect to the mean quadratic velocity ($v_e = \langle v_e^2 \rangle^{1/2}$) of orbital electron: the high, intermediate and low velocity domains. When ion cross the material at high velocity ($v \gg v_e$), ion is fully stripped. All the surrounding electrons are removed and the ion exists only as a bare nucleus. The charge of ion at high velocity (fully stripped) is equal to the atomic number ($Z_{eff} = Z$). In the intermediate domain, the speed of ion is comparable with the speed of electron ($v \sim v_e$). In this domain, the process of continuous capture and emission of electron occurs and ion is partially stripped. The effective charge of ion (Z_{eff}) is introduced as being proportional to the velocity of ion (for $v \leq v_{Bohr} Z^{2/3}$)

$$Z_{eff} = Z^{1/3} \frac{v}{v_{Bohr}} \quad \text{where} \quad v_{Bohr} = \frac{e^2}{4\pi\varepsilon_0 \hbar} = \alpha c = 2.2 \times 10^6 \ m/s \tag{1.5}$$

At low velocity domain ($v \ll v_e$), the process of electron capture becomes more and more probable. The practical charge state of ion decreases as ion slows down in the material. At the end, ion becomes slightly charged and enters into the domain in which nuclear interaction starts.

1.2.2 The stopping power

While traveling through solids, ion gradually transfers energy to orbital electrons and nuclei (constituents of the material) and therefore loses energy along their path. This amount of energy transferred is not constant and depends on collisions to collisions. In addition, it depends instantly on several parameters such as the characteristics of the ion (the nature and the initial energy of ion), the constituents of the material through which it passes... In order to characterize for the energy loss of ion in interaction with materials, the stopping power is introduced. The stopping power (usually measured in $MeV.\mu m^{-1}$, $keV.nm^{-1}$ or $eV.\mathring{A}^{-1}$) is defined as the energy loss of the charged particle per unit of thickness of material covered. The stopping power depends on the nature and energy of particle and on the composition of materials through which it crosses (see, for example, Table 1.2). It is, therefore, treated as one property of the material (even it describes what happens to the charged particle). Mathematically, the stopping power is expressed as:

$$-\frac{dE}{dx}(E)$$

where the minus sign expresses the loss of energy of ion.

Ion's energy (MeV)	Xe (keV/nm)	Ce (keV/nm)	La (keV/nm)
100	25.5	21.2	21.2
10	6.3	5.7	5.7
1	4.2	4.4	4.3
0.5	4.3	4.5	4.4

Table 1.2: Stopping power in UO_2 calculated by SRIM.

Since ion interacts with materials via two mechanisms, the stopping power is also separated in two terms: electronic and nuclear stopping powers. The electronic stopping power is defined as the amount of energy loss via electronic interaction per unit of distance covered, while the nuclear stopping power is specified as the amount of energy loss per unit of distance covered via elastic nuclear collision between ion and nuclei:

$$-\left(\frac{dE}{dx}(E)\right)_{electronic} \quad \text{due to electronic collision}$$

and

$$-\left(\frac{dE}{dx}(E)\right)_{nuclear} \quad \text{due to nuclear collision}$$

The overall stopping power is then the sum of the two contributions:

$$-\left(\frac{dE}{dx}(E)\right)_{electronic} - \left(\frac{dE}{dx}(E)\right)_{nuclear} \tag{1.6}$$

Practically, the stopping power depends on many parameters. But for a defined ion and material, the stopping power depends only on the energy of ion. Figure 1-5 shows the evolution of stopping power of Cerium ion in UO_2 as a function of its energy. The data are obtained by using SRIM simulation code for both electronic and nuclear stopping power in the range from 10^{-2} keV to 10^{9} keV. Typically, the diagram of electronic stopping of Cerium can be dived into 4 domain with the energy corresponds to: (i) above 50 GeV (ii) between 2 GeV and 50 GeV (iii) between 0.4 GeV and 2 GeV and (iv) below 0.4 GeV. For ions having energy higher than 50 GeV, it is governed by the the theory of relativity since its velocity is fairly comparable to the velocity of light. The electronic stopping in this domain is estimated following the Bethe and Bloch theory taking into account the relativistic correction [20]. For ions with energy in the domain from 2 GeV to 50 GeV, it is totally stripped, i.e. all the orbital electrons surrounding the ion are removed and ion has the charge state of 58+. The energy lost via electronic interaction is described by the

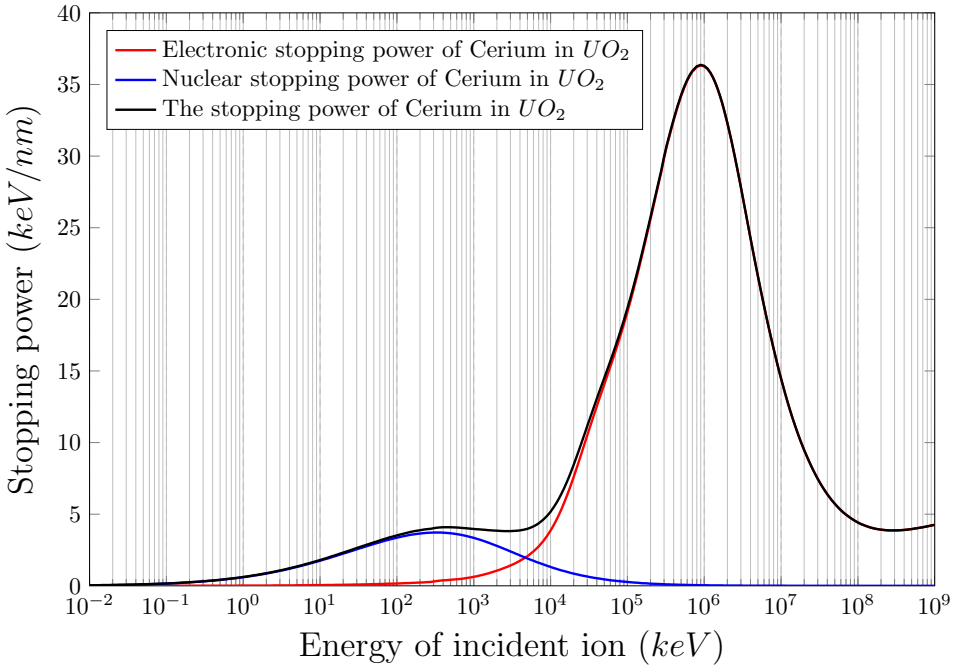

Figure 1-5: Stopping power of Cerium ions in UO_2 calculated according to the SRIM code.

theory proposed by Bethe [21] and Bloch [22]:

$$-\frac{dE}{dx} = \frac{4\pi}{m_e c^2} \cdot \frac{NZ^2}{\beta^2} \cdot \left(\frac{e^2}{4\pi\varepsilon_0}\right)^2 \cdot \left[\ln\left(\frac{2m_e c^2\beta^2}{I\cdot(1-\beta^2)}\right) - \beta^2 - \sum_i \frac{c_i}{Z_2} - \delta\right] \tag{1.7}$$

where v, E, Z are respectively the velocity, the energy and the charge of the particle;
c is the speed of light;
$\beta = v/c$;
e and m_e are the charge and the mass of the electron;
N is the electron density of the target;
I is the mean excitation potential of the target;
ε is the vacuum permittivity;
$\sum_i \frac{c_i}{Z_2}$ is the shell correction;
δ is the Fermi's density correction.

According to this formula, the electronic stopping power of Cerium ion at high energy is inversely proportional to the square of the its velocity. That explains why we observe the increasing electronic stopping while ions slow down in material over this energy range. When ions enter into the domain from 0.4 GeV to 2 GeV, the velocity of ion becomes comparable to the velocity of orbital electrons. In this domain, the Bethe and Bloch formula is no longer valid. The electronic stopping reaches the maximum value (Bragg peak observed around $v_{Bohr}Z^{2/3}$ which corresponds to the energy of projectile of 1 GeV) and tends to fall down after. It is quite complicated to estimate theoretically

the electronic stopping in this case because the process of capture of electron becomes more and more important. Ion is no longer considered as fully stripped. To calculate the electronic stopping, the practical approach is to extend the validity of the Bethe and Bloch theory to this domain by introducing the concept of effective charge (Z_{eff}) [23]. It was first introduced by Bohr [24, 25] and Lamb [26]. This very first model supposed that the effective charge of ion is directly proportional to the speed of ion (see formula 1.5). In 1982, Brandt [27] proposed himself a theory with which a large summary of stopping power data for heavy ions was successfully established. Once overcoming this domain, ions enter into the domain of low velocity in which the speed of orbital electrons is higher than the speed of incident ions and ions. After successfully capturing many electrons during its passage, ion return back to its actual ionization state. At low velocity, the electronic stopping of ions is supposed to be proportional to the speed of projectile ions. This theory was proposed by Lindhard and Scharff [28] and independently by Firsov [29, 30, 31, 32] in which the electronic stopping of ions is expressed as:

$$-\frac{dE}{dx} = 8\pi N \left(\frac{e^2}{4\pi\varepsilon_0}\right) a_0 \frac{Z_1^{7/6} Z_2}{(Z_1^{2/3} + Z_2^{2/3})^{3/2}} \cdot \frac{v}{v_{Bohr}}$$

where $a_0 = 4\pi\varepsilon_0\hbar^2/me^2 = 5.29\times10^{-11}\ m$ is the Bohr radius.

By the end of the path inside the solid, ions slows down into the domain of energy below few MeV. In this energy range, the electronic interaction becomes less important and the main interaction is the elastic nuclear collision between ions and nuclei. The nuclear stopping is practically 100 times greater compared to the electronic stopping.

The introduction of the effective charge has helped us to join the domain of high and low speed together with the maximum of the electronic stopping power. A full picture of electronic stopping has been well established.

1.2.3 Radiation induced defects

During passage inside the material, ion transfers part of its energy to atoms and this process could lead to the formation of structural defects. The types and the number of defects created depend on the nature of interactions and on the quantity of energy transferred. The accumulation of effects for a material submitted to a long time irradiation could result in significant modification of the material's properties. These properties include physical dimensions, strength and hardness, thermal and electrical conductivity, corrosion resistance and many others. Knowledge of effects of ion bombardment is therefore necessary in order to understand the behaviour of the material submitted to highly irradiation condition and to predict the life-time of the material.

Defects creation via elastic nuclear interaction

As discussed previously, the major interaction between low energy ion and material is elastic nuclear collision. This situation happens practically when ion comes to the end of its trajectory inside the solids. This colliding process results in the transferring of energy from ion to atomic nucleus with the maximum of energy transferred is predicted by formula 1.3. Depending on the amount of energy transferred, defects might be created. If the energy transferred to a lattice atom is higher than the minimum energy needed to permanently displace an atom from its regular lattice site, which is called the *"displacement threshold energy"* E_d, atom will be ejected from its position in the lattice. Likewise, the displacement of an atom leads to the formation of an empty lattice site called a vacancy. The ensemble of point defect and vacancy is named as the "Frenkel pair" defect. The creation of a Frenkel pair is possible provided that the interstitial point defect is sufficiently far away from the vacancy so that the recombination of interstitial-vacancy does not take place.

The displaced atom (called the primary knock-on atom or PKA in short as it is the first to be attacked by external ion) might carry enough kinetic energy to induce a secondary displacement (internal radiation). The secondary displaced atom in turn could itself create others displacements etc. The process continues and a series of displacements might be induced by a single projectile before it comes to rest. Finally, a highly disordered region around the path of ion is generated as it passes through the material. This process (known as a collision cascade) happens by the end of ion's trajectory via uniquely elastic collision and the set of point defects created is known as a displacement cascade. According to the model proposed by Kinchin and Peace [33] the number of displacements can be estimated as following:

$$\begin{cases} \langle N(T)\rangle = 0 & \text{if} \quad T < E_d \\ \langle N(T)\rangle = 1 & \text{if} \quad E_d \leq T < 2E_d \\ \langle N(T)\rangle = T/2E_d & \text{if} \quad T \geq E_d \end{cases}$$

in which T is the kinetic energy of the primary knock-on atom. Taking into account the contribution of electronic stopping, the number of displacements induced by PKA of energy greater than $2E_d$ is expressed as:

$$\langle N(T)\rangle = K\frac{T - E_\varepsilon}{2E_d} \quad \text{with} \quad K \approx 0.8$$

As a consequence of the collision cascades, the total number of displacements is caused not only by the direct ion-atom collision but also via all the secondary PKA-atom collisions. With the assumption made by Kinchin and Peace, the total mean number of

displacements along the entire ion range is given by:

$$\langle N_{tot} \rangle = \frac{E_{c1}}{2E_d}$$

which is dependent of the energy given to the projectile ion (E_{c1}) and the displacement threshold of the target atom (E_d) and is totally independent of the atomic numbers. Due to the bombardment, an atom might be displaced several times or might not be displaced at all. The average number that one target atom has been displaced over the entire process is called the "displacements per atom (dpa)". The notation of displacements per atom is a more convenient quantity in irradiation experiments rather than the flux (mostly in particles per unit of surface and time) or the fluence (in particles per unit of surface) for the investigation of the elastic collisions effects.

During collision cascades, interstitials and vacancies can be produced so close one to each other that they might easily recombine. The recombination results in the number of defects induced become practically much smaller. Due to the close proximity of the clustering of point defects, many of interstitials and vacancies created during collision cascades annihilate. Only as low as about few percent of the initially created point defects can survive and are capable of successfully producing a radiation induced defect.

Defects creation via inelastic electronic interaction

The energy transferred from ion to material is generally separated into two parts: (i) the continuous energy loss due to the interaction with the cloud of orbital electrons leading to the excitation and ionization of atoms but not to the direct displacements of atoms and (ii) the discrete energy loss due to the binary elastic ion-atom collision leading to the creation of Frenkel pair or collision cascades (previously discussed).

At high energy (high velocity), the cross section of nuclear interaction between ion an atom is low. The main interaction is the electronic interaction (coulomb interaction) between ion and the cloud of orbital electrons. Through the coulomb interaction, ion continuously transfers energy to the material via process of excitation and ionisation which finally transform to the heat of the target. Depending on the energy transferred, the defects may be created if the energy transferred leads to the high increase in temperature (intense excitation) or no defect is created but just the small increase of temperature observed (weak excitation).

When the energy transferred to the electrons is small but high enough to remove them completely from the shell level, a pair of electron-hole is created. In a metallic materials, this e-hole pair will be annihilated due to the high mobility electrons. The energy will quickly be transformed to the thermal vibration of the target. No localisation of charge or energy deposition is observed and no defect is induced. Inversely, in a non-

metallic materials, the e-hole has an increased stability.

When the energy transferred to the electrons is much higher (as normally the case of swift heavy ion), ion loses a few hundreds of eV to several target atoms over each inter-atomic distance. Atoms located in a cylindrical area of about 1 nm along ion trajectory are multi-ionized in typically 10^{-16} s after the passage of the ion. Electrons that have been removed spread into the material and lose energy by numerous interactions, an electromagnetic cascade is therefore created. Due to the formation of the electromagnetic cascade, the initial deposited energy dilutes progressively leading to a radial distribution of energy transferred to the target. The radial distribution of the energy density follows a dependence with the inverse of the radius square $(1/R^2)$ [34].

As the cylindrical region center along the path of the ion is highly ionized, all the positive charged atoms within the cylinder form a strongly unstable zone due to the strong Coulomb repulsion between particles of same type of charge. This can cause an explosion and therefore leads to the displacements of atoms (creation of damage due to electronic interaction) within the cylinder forming the latent track. The displacements of atoms require that the energy given to atoms should be higher than the binding energy to the lattice, say > 25 eV [35]. The mechanism was developed by Fleischer, Price and Walker in 1965 as the well-known "ion explosion model" to explain the formation of amorphous latent track registration in solids [36].

In 1960, Lifchits proposed the theory called the "thermal spike" which was then extended to fast heavy ions by Toulemonde in 1992 [37, 34]. The theory supposes that the target is considered as two continuous physical systems: the electron gas and the atomic lattice of cylindrical geometry. The theory supposes that under intense electronic excitation, the space and temperature of the electron gas and the atomic lattice is governed by the following coupled system of differential equations:

$$\begin{cases} C_e \dfrac{\partial T_e}{\partial t} = \dfrac{1}{r}\dfrac{\partial}{\partial r}\left[r K_e(T_e) \dfrac{\partial T_e}{\partial r} \right] - g(T_e - T_l) + A(r,t) \\ \\ C_l \dfrac{\partial T_l}{\partial t} = \dfrac{1}{r}\dfrac{\partial}{\partial r}\left[r K_l(T_l) \dfrac{\partial T_l}{\partial r} \right] + g(T_e - T_l) \end{cases}$$

in which

$T_e,\ T_l$ are the temperature of the electron gas and the atomic lattice, respectively;

$C_e,\ C_l,\ K_e\ K_l$ are respectively the specific heats and the thermal conductivities of electron and lattice atom;

$A(r,t)$ is the energy obtained through the electron cascade after the passage of ion;

g is the electron-lattice coupling constant.

This coupled system of differential equations has no analytical solution but numerical solution shows that ion deposits an extremely high density of energy in a short time that it results in the high temperature of the target within the cylindrical vicinity. As a consequence, the inter-atomic liaisons between atoms in this area are broken. Atoms located within this area become highly disordered that they lead to the fusion of solid in the cylinder. This cylinder is so called the amorphous latent ion track which exists only in a very short time but the trace of ion track can be found under form of point defect or even as a molten to frozen zone in some cases.

1.2.4 Behaviour of ceramics under irradiation

Ceramic materials (e.g. uranium dioxide UO_2, yttria-stabilized zirconia YSZ, magnesia spinel $MgAl_2O_4$ ...) have important applications in the nuclear industry. They are candidates for cladding materials and the promising matrices for immobilization and/or transmutation of nuclear wastes. To these applications, the knowledge of their behaviour upon irradiation is necessary. For that reason, many investigations have been being conducted so as to understand the behaviour of ceramics submitted to the bombardment of ion within them. Both the effects of the two main slowing down regimes (Sn and Se) were separately investigated: low-energy ions are utilized in order to study the effects of nuclear collision (lattice disorder, dislocation, amorphization ...) whilst swift ions are used so as to study the effects of electronic slowing down (formation of defect cluster, latent tracks ...).

Various classes of defects can be produced as low-energy ion slows down in ceramics. Due to the nuclear elastic collision which is prominent at the end of ion path, Frenkel pairs defects are created provided that the energy transferred to lattice target atoms is higher than the displacement threshold. Even though the number of survival Frenkel pairs defects is of few percent only, it is still high enough that they can finally accumulate and lead to the transformation of the structure. Interstitial defects, for instance, gather together forming the defect clusters while vacancy defects, on the other hand, concentrate in a bulk forming the cavity defects. When their concentration continue to increase upon irradiation, interstitial defects can accumulate in the further step leading to the formation of dislocation loops and hence dislocation networks. Those classes of defects are produced in a higher quantity (growth of defects) as the material is further irradiated. As a result, they cause the damage and transformation of the structure resulting in the swelling, polygonalization and also modification of the chemical, electronic, thermal, mechanical and other properties of the material.

Many investigations regarding the radiation effects on ceramic materials for nuclear energy have been conducted. Amongst them, investigations of ceramics single crystals

as the simplest model play an important role for achieving the very basic knowledge of radiation effects on ceramics structure. Several techniques including the Rutherford Backscattering in Channelling condition (RBS/C), X-Ray diffraction analysis (XRD) and Transmission Electron Microscopy (TEM), were applied for the investigation.

Behaviour of zirconia under irradiation

As discussed previously (see Sec. 1.1.2), pure zirconia exists under only monoclinic structure. When the temperature increases, pure zirconia undergoes two crystallographic transformations and the associated volume change is quite large that make it impossible to be used in applications. However, adding some oxides material can help pure zirconia to fully stabilize in cubic form (*fcc* form) which is of importance in application. This section is a summary of research carried out on both pure monoclinic and fully stabilized zirconia.

The mechanism of the radiation-induced phase transformation, monoclinic to *fcc*, in pure ZrO_2 was investigated by Wittels [38] in 1962. The effects of fast neutrons, fission fragments, and uranium chemical impurities were distinctly studied. The results indicated that: (i) fission fragment fluxes of $10^{15} - 10^{16}\ fissions/cm^3$ produced a monoclinic to *fcc* phase change in ZrO_2, and the presence of U in ZrO_2 in concentrations less than 0.38 $wt.$ % did not act as a nucleation or stabilizing atom in the process; (ii) the stability of the phases of ZrO_2 under reactor irradiation depended entirely upon the action of a fission fragment flux of sufficient magnitude; (iii) fast neutrons, solely, could not induce the phase transition at doses up to $6.3 \times 10^{20}\ n/cm^2$; (iv) in twenty-one analyses for U and Th in randomly selected reactor grade zirconium and its alloys, fissionable impurities were found in twenty cases. Natural uranium concentrations varied between 1.8 and 6.3 ppm, and thorium concentrations varied between 0.29 and 50 ppm. Two different models were given to explain the mechanism of fission fragments in producing the phase transition. Both models required the collapse of small regions due to the pressure exerted by interstitials. In one case the action took place at the beginning of the fission fragment's range via an ionization displacement process, and in the other instance the process occurred near the end of the fission fragment's range where elastic collisions predominate.

Sickafus [39], in 1999, performed another investigation on the evolution of radiation-induced damage in pure, unstabilized monoclinic zirconia and in Y, Ca and Er FSZ by RBS/C along with XRD and TEM. The crystals were irradiated with $340-400\ keV\ Xe^{2+}$ from 170 to 300 K. The main results obtained by RBS/C showed that the damage accumulation in $FSZs$ irradiated by Xe ion progresses in three stages and no amorphisation was observed (see figure 1-6). Unstabilized monoclinic zirconia was observed to transform to a higher symmetry, tetragonal or cubic phase, upon $340-400\ keV\ Xe^{2+}$ ion irradiation to Xe fluences in excess of $5 \times 10^{14}\ cm^{-2}$ (equivalent to $\sim 2\ dpa$). No amorphisation was

observed up to Xe fluence equivalent to 680 *dpa*.

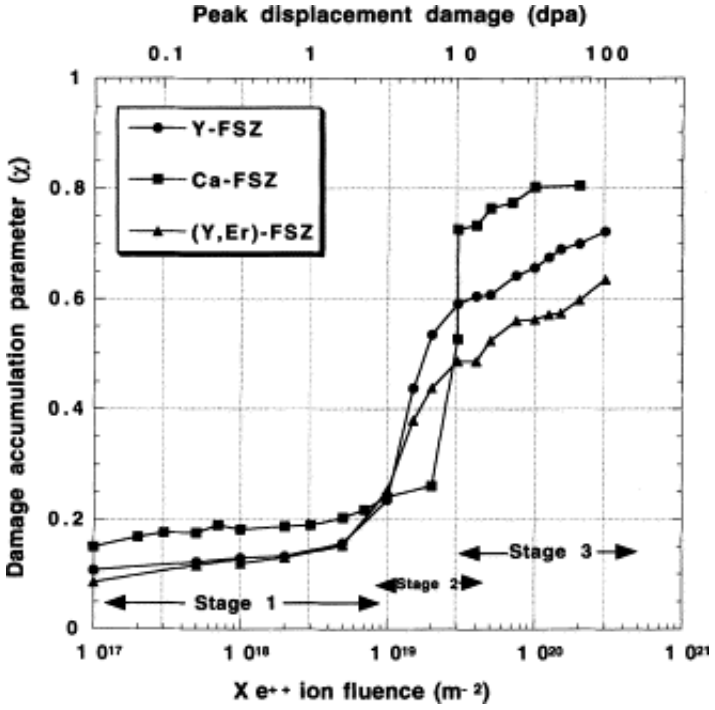

Figure 1-6: Damage accumulation recorded in $FSZs$ [39].

N. Yu et al. [40], in 1997, studied the YSZ single crystals submited to the 400 keV Xe ion irradiation at room temperature and at $T = 183\ K$ (−90°C). Defect growth was monitored *in situ* with RBS/C techniques using a 2 MeV He ion-beam. The irradiated YSZ was observed to reach the lattice disorder saturated at 70 % of the random level. The kinetic of disorder are almost identical at both room temperature and $T = 183\ K$ (see figure 1-7). At the fluence of $3 \times 10^{16}\ cm^{-2}$, the damaged layer extended to a depth of 160 nm, well beyond the irradiated depth ($< 110\ nm$). No amorphisation was observed up to the fluence of $3 \times 10^{16}\ cm^{-2}$(highest ion fluence reached in this experiment), corresponding to 110 *dpa*. *Ex situ* TEM images revealed the presence of small Xe precipitates with an average diameter of 3 nm, uniformly distributed over the $20 - 110\ nm$ in depth.

Dong-zhu Xie and colleagues studied YSZ single crystals implanted with 105 and 160 keV platinum ions to nominal doses of $2 \times 10^{16}\ cm^{-2}$ and $5 \times 10^{16}\ cm^{-2}$, respectively, at room temperature [41], and annealed, afterwards, isothermally in air ambient at 1123 and 1373 K (850°C and 1100°C respectively) from 4 to 12 h. Rutherford Backscattering Spectrometry and Channelling of 2 MeV He ions was used to study the depth distribution of lattice damage and implant, as well as the annealing behaviour. X-ray diffraction (XRD) was employed to analyse the crystallite size of implanted platinum. Both as-implanted samples do not show an amorphous phase. The Pt depth profile was almost unchanged for all samples during annealing at 1123 and 1373 K. For the 160 keV implanted sample

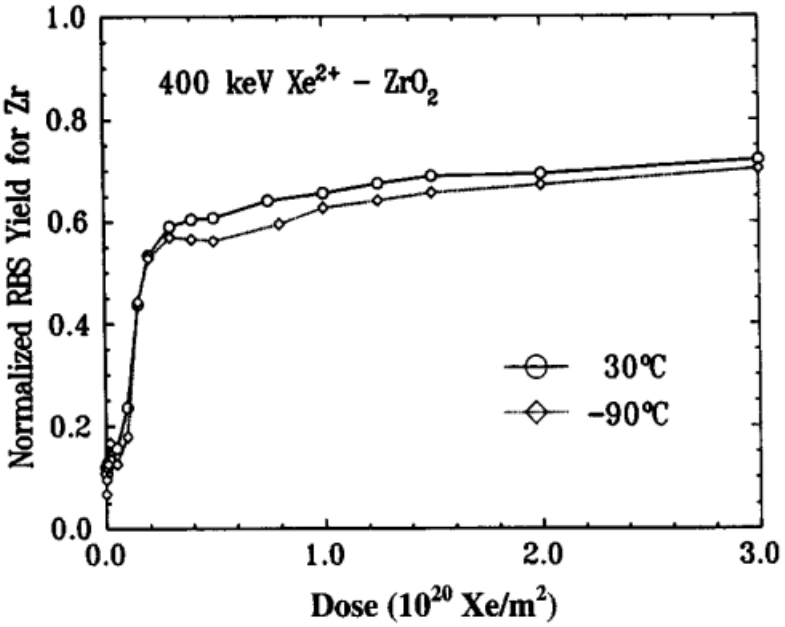

Figure 1-7: Damage accumulation in YSZ measured by RBS/C at irradiated temperature of 303 and 183 K [40].

no loss of Pt was observed after annealing at 1373 K. XRD results provided evidence for the formation of a monoclinic phase of ZrO_2 in the damage region after 1373 K annealing. For all annealed samples, Pt $\langle 200 \rangle$ preferred orientation crystallites were observed by XRD, while the Pt $\langle 111 \rangle$ peak was almost not visible for 1123 K annealed samples.

Sickafus [42], in 1998, studied the cubic-stabilized zirconia single crystals irradiated with $72-MeV$ I^+ ions (to simulate a typical U or Pu fission fragment). Irradiations were performed over the fluence range from 1×10^{14} to 5×10^{15} cm^{-2}, at temperatures of 300, 770, and 1170 K. At ambient temperature and at the highest I^+ fluence (5×10^{15} I^+/cm^2), RBS/C measurements revealed a high degree of lattice disorder. Specifically, the dechannelling parameter χ_{min} varied from 80 % to greater than 90 % over the depth probed by RBS/C (~ 1 μm). Nano-indentation measurements on the same sample indicated a decrease in elastic modulus, E, and hardness, H (both by about 9 %). These results suggest that an alteration in structure beyond simple defect accumulation occurs under these irradiation conditions. However, transmission electron microscopy observations and in particular micro-diffraction measurements failed to reveal any structural transformations in the irradiated material.

Wang et al. [43], in 2000, observed the amorphization of YSZ submitted to the 400-keV Cs-ion implantation to 1×10^{17} cm^{-2} at room temperature. Amorphization of YSZ was caused by the large size incompatibility and low mobility of Cs ions in the YSZ structure, which reflects a relatively low solubility of Cs in YSZ. Nevertheless, the Cs concentration at which amorphization of YSZ occurred is about 8 $at.$ %, well above the

typical value that could be reached in an inert fuel matrix.

Afanasyev-Charkin [44] investigated the effects of 340 keV Xe^{2+} irradiations on YSZ with fluences ranging from 1×10^{11} to 1.5×10^{17} cm^{-2}. RBS/C data and TEM images revealed no amorphization of YSZ after irradiation even to the highest investigated ion fluence. An analytical model was developed, using ion range and damage distributions calculated based on Monte Carlo simulations for ion-solid interactions, to assess sputtering effects at high fluence. Analysed results and experimental data revealed that at high fluences, the implanted ion and damage distribution profiles were significantly modified by sputtering.

Yasuda investigated the defect clusters induced in FSZ irradiated with ions and/or electrons [45]. Micro-structure evolution of YSZ, ZrO_2-13 mol % Y_2O_3, was investigated through transmission electron microscopy. Anomalous formation of large defect clusters was found under electron irradiation subsequent to ion irradiation, such as 300 keV O^+, 100 keV He^+ and 4 keV Ar^+ ions. Such defect clusters were not formed solely with ion irradiation. The defect clusters were transformed into dislocation network when they reached a critical diameter of about $1.0-1.5$ μm, and processes of nucleation, growth and transformation were repeated under electron irradiation. The defect clusters were assumed to be oxygen platelets induced through selective displacements of oxygen ions in YSZ with electron irradiation.

In 2005, Hojo and his co-workers studied the effects of irradiation on YSZ and the influence of temperature [46]. *In situ* electron microscope was used to observe the defects induced in YSZ single crystal irradiated by helium and xenon ion. Damage evolution was observed during irradiation with $35-keV$ He^+ with a flux of 5×10^{13} $cm^{-2}.s^{-1}$ at 1073, 1273 and 1473 K and during the irradiation with $60-keV$ Xe^{2+} with a flux of 5×10^{12} $cm^{-2}.s^{-1}$ at 1073 and 1473 K. The formation of Xe bubbles was clearly observed. Dislocation loops were formed by Xe ion irradiation at both temperatures but were not formed by He. The results had revealed the clear dependence of loop formation on the ion species.

Thomé and colleagues studied the damage production in yttria-stabilized cubic zirconia single crystals irradiated with medium-energy (from 30 to 450 keV) heavy ions (from He to Cs) [47]. The disorder created in the two sub-lattices (Zr^{4+} and O^{2-}) of the crystals and the lattice sites of heavy ions were determined by *in situ* Rutherford backscattering and channelling experiments using a $3-MeV$ ^4He ion beam. Damage was created at a depth close to the ion projected range at low fluences and growths towards greater depths with increasing fluences once the saturation was reached. The kinetics of the damage accumulation process revealed three stages, which (excepted for He) essentially depended on the number of displacements per atom (dpa) induced by irra-

diating ions (*ballistic contribution*). Channelling results show that the lattice location of the heaviest atoms (Xe, Cs and I) varied with the nature of implanted species (*chemical contribution*). The position of Xe and I ions is almost random over the whole fluence range investigated, meanwhile a large fraction of Cs ions is located in substitutional lattice sites at low ion fluences. At high fluences, Cs loses its substitutionality and this could be due to the precipitation of implanted species or to the formation of compounds (such as Cs_2ZrO_3), both processes being driven by a radiation-enhanced diffusion mechanism.

In 2004, Jagielski and his colleagues [48] investigated the zirconia single crystals irradiated with 450 MeV Xe ions with fluences from 10^{13} up to 2×10^{14} cm^{-2}. A methodology based on Monte-Carlo simulations of RBS/C data was proposed in order to quantitatively obtain the damage induced. The results showed that the concentration of defects was almost constant at depths above $\sim$ 500 nm, with a decreasing value in the near-surface region of the crystal. The defect accumulation kinetics exhibited a saturation at a fluence of 5×10^{13} cm^{-2} and could be reproduced by assuming the formation of tracks (diameter $\sim$ 2 nm) induced by electronic excitation processes.

A. Gentils and co-workers [49] applied the MC simulation methodology proposed previously [48] to the investigation of the damage produced in cubic zirconia single crystals irradiated with swift heavy ions. A large variety of swift heavy ions: ^{20}Ne at 70 MeV, ^{40}Ar at 100 MeV, ^{84}Kr at 732 MeV, ^{129}Xe at 450 MeV and ^{208}Pb at 931 MeV were used. Conclusions were that: (i) relatively flat damage profiles were obtained up to depths higher than 2 μm; (ii) The damage fraction increased strongly with the electronic energy loss with a threshold for damage formation at $20 - 25$ keV/nm and (iii) the creation of damage at high electronic stopping force $(dE/dx)_e$ likely resulted from the formation of non-amorphous tracks.

Moll et al. [50] investigated YSZ single crystals irradiated with heavy ions at energies ranging from a few MeV to a few GeV in order to compare the effects of nuclear collisions and electronic excitations. The damage created by irradiation was measured by RBS/C. Monte-Carlo simulations of RBS/C data showed that both the depth distributions of radiation damage and the damage build-up strongly depend on the type of irradiation. At low energy (4 MeV Au ions) the damage exhibited a peak around the ion projected range ($\sim$ 500 nm) and it accumulated with a double-step process; at high energy (940 MeV Pb ions) the damage profiles were flat up to several micrometers and the damage accumulation was monotonous (one-step). RBS/C and X-ray diffraction results showed that the various irradiations never lead to the amorphization, even at the highest fluences.

In summary, zirconia presents a high resistance to ion irradiation. Amophization was observed only in case of irradiation by 400 keV Cs ion [43] to 1×10^{17} cm^{-2} at ambient temperature. However, the Cs concentration at which amorphization of YSZ

occurred is about 8 $at.$ % which is higher than typical concentration that could be reached for nuclear applications.

Behaviour of magnesia spinel under irradiation

Single crystal and polycrystalline $MgAl_2O_4$ submitted to fast neutron (0.1 MeV) irradiation to dose of $\leq 2-3\times10^{26}$ n/m^2 was investigated by Clinard [51]. In irradiated single-crystal, only high-energy faulted loops were observed as sinks for interstitial atoms; vacancy-interstitial recombination was the dominant mode of defect accommodation, and negligible swelling results. However, polycrystalline spinel exhibited void formation near grain boundaries, and concomitant swelling, indicating that these boundaries were effective sinks for interstitials. $MgAl_2O_4$ spinel single crystal were again examined by neutron diffraction by Sickafus [52]. Crystal structure refinement of the highest fluence sample indicated that the average scattering strength of the tetrahedral crystal sites decreased by 20 % while increasing by 8 % on octahedral sites. Since the neutron scattering length for Mg is considerably larger than for Al, the result was consistent with site exchange between Mg^{2+} ions on tetrahedral sites and Al^{3+} ions on octahedral sites. Least-squares refinements also indicated that, in all irradiated samples, at least 35 % of Mg^{2+} and Al^{3+} ions in the crystal experienced disordering replacements.

In 1996, Sickafus performed another investigation on non-stoichiometric and stoichiometric magnesio-aluminate spinel single crystals (compositions $MgO\cdot Al_2O_3$ and $MgO\cdot 3Al_2O_3$, respectively) [53]. Irradiations with both 400 keV and 1.5 MeV Xe ions under cryogenic and room temperature conditions were made, in order to compare the irradiation damage response of these isostructural compounds. Overall, stoichiometric spinel was found to be more resistant to irradiation damage (microstructural alterations) than the non-stoichiometric compound. At room temperature, non-stoichiometric spinel transformed to a "metastable crystalline structure"[3] at an ion dose corresponding to 1 to 2 dpa, while this transformation was not observed in stoichiometric spinel to a dose of 10 dpa. Furthermore, under cryogenic conditions, both stoichiometric and non-stoichiometric spinel underwent a metastable phase transformation, followed by a transformation to an aperiodic structure at similar ion doses.

The micro-structure of polycrystalline stoichiometric $MgAl_2O_4$ was examined by cross-sectional electron microscopy following 430 MeV Kr^+ or 614 MeV Xe^+ ion irradiation near room temperature up to a fluence of 1.1×10^{16} $ions/m^2$ [55]. In addition, the micro-structure was examined for two specimens which had been pre-irradiated with either 2 MeV Al^+ ions or 3.6 MeV Fe^+ ions and subsequently irradiated with 430 MeV

[3] This is a disordered structure in which the O^{2-} anion sub-lattice maintains a "*pseudo*"-cubic close-packed arrangement (as in spinel), while the cations occupy randomly the octahedral lattice interstices and all tetrahedral interstices are empty [54].

Kr^+ ions. The Al^+ and Fe^+ pre-irradiated specimens contained a high density ($10^{21}-10^{23}$ m^{-3}) of interstitial dislocation loops with diameters between 5 and 30 nm prior to the swift heavy ion irradiation. Near-continuous latent ion tracks were observed in all of the specimens irradiated with swift heavy ions. The swift heavy ions also appeared to efficiently destroy pre-existing dislocation loops with diameters 5 nm, whereas larger loops remained intact following the swift heavy ion irradiation. The swift heavy ions caused structural disordering of the octahedral cautions, but did not appear to produce amorphous cores in the ion tracks. The disordered ion track diameters were ~ 2.0 and ~ 2.6 nm for the 430 MeV Kr and 614 MeV Xe ion irradiations, respectively.

Spinel of $MgAl_2O_4$ irradiated with Cu^- at dose rates up to 100 $\mu A/cm^2$, to a total dose of 3.0×10^{16} cm^{-2} was studied by Kishimoto [56]. Nanocrystal morphology and optical absorption ($\sim 0.5-5$ eV) varied depending on flux. At high fluxes, $MgAl_2O_4$ showed spontaneous precipitation of nanoparticles but, in contrast, neither long-range rearrangement of implants nor particle coarsening, up to high fluxes.

Structural changes in magnesium aluminate spinel ($MgO \cdot nAl_2O_3$) single crystals, which were irradiated with 900 keV electrons or 1 MeV Ne^+ ions at 873 K, were examined by electron channelling-enhanced X-ray microanalysis [57]. Un-irradiated $MgO \cdot Al_2O_3$ has a tendency to form the normal spinel configuration, where Mg^{2+} ions and Al^{3+} ions occupy mainly the tetrahedral and the octahedral sites, respectively. Electron irradiation induces simple cation disordering between the tetrahedral sites and the octahedral sites in $MgO \cdot Al_2O_3$. In addition to cation disordering, slight evacuation of cations from the tetrahedral sites to the octahedral sites occurs in a peak-damaged area in $MgO \cdot Al_2O_3$ irradiated with Ne^+ ions. In contrast, cation disordering is suppressed in $MgO \cdot 2.4Al_2O_3$ irradiated with electrons. The structural vacancies, present in the non-stoichiometric compound, appear to be effective in promoting irradiation damage recovery through interstitial-vacancy recombination.

The damage accumulation of $MgO \cdot n(Al_2O_3)$ single crystal implanted with 60 keV Cu^- at a flux up to 100 $\mu A/cm^2$ was studied by RBS/C [58]. No complete amorphization was observed over the flux range examined, although the crystalline lattice was significantly damaged. The damaged region on the Al sub-lattice extended to a deeper region with increasing flux. Fluence and flux dependence of Al damage peak was greatly influenced by the stoichiometry n of spinel. The Al damage peak of $MgO \cdot 1.0(Al_2O_3)$ was smaller for higher flux and fluence. Explanation was that the recombination of radiation-induced interstitials with structural vacancies effectively reduces damage of the Al sub-lattice. In the case of $MgO \cdot 2.4(Al_2O_3)$, the Al damage peak, however, increased with increasing fluence and flux. The RBS/C results indicated that the recombination mechanism was more effective in the stoichiometric spinel than the non-stoichiometric one.

The effects of swift heavy ion irradiation on nearly stoichiometric magnesium aluminate spinel ($MgO \cdot 1.1Al_2O_3$) was analysed by transmission electron microscopy. Irradiation was made with 200 MeV Xe^{14+} ions ($S_e = 25$ keV/nm) up to 5.0×10^{11} and 2.0×10^{12} cm^{-2} at ambient temperature [59, 60]. Bright-field (BF) images revealed that 200 MeV Xe^{14+} ions produced heavily disordered columns about $4 - 5$ nm in diameter along the tracks, tiny pits were formed at the entrance of ion tracks. Electronic excitation from one particle of 200 MeV Xe^{14+} caused significant disordering in region over 10 nm in diameter. The disordering of Al^{3+} ions took place over a larger area than that of Mg^{2+} ions. The disordered zones overlapped each other after irradiation up to 10^{12} cm^{-2}. Clear lattice fringes are observed in HR images even inside the ion tracks, indicating that the spinel crystals were not amorphized but partially disordered along the ion tracks. High angular resolution electron channelling X-ray spectroscopy (HARECXS) analysis showed that cation disordering progressed successively with ion fluence, and the disordered regions were found to extend over 12.8 ± 0.9 nm in diameter for Al ions and 9.6 ± 0.6 nm for Mg ions along the ion tracks. This chemically disordered region was much larger than the strained volume detected by BF and HR images.

Effects of swift heavy ion irradiation on magnesium alunimate spinel was also investigated elsewhere [61, 62]. Structural defects in the surface region of $MgAl_2O_4$ crystals irradiated with 450 MeV Xe ions were analyzed by using ^4He RBS/C. Monte-Carlo simulations applied for the interpretation of channelling spectra permitted to determine the concentration of radiation-induced defects. The depth distribution of defects was obtained. The results showed that the defect distributions were depth-dependent, likely due to annihilation of defects at the surface of the crystals. The cross-section for the formation of defects by swift Xe ions, and consequently the diameter of an ion track, were estimated using single-impact-model calculations.

The chemical and structural modifications in $MgAl_2O_4$ single crystals submitted to Cs ion implantation and thermal treatments were investigated by RBS/C experiments [63]. The changes of composition, the damage created and the behaviour of implanted ions were studied as a function of the Cs fluence and annealing temperature. Heat treatments showed that the lattice disorder was clearly maximum just after implantation and decreased with increasing annealing temperature. Heat treatments above 800°C lead to huge chemical and structural modifications. A drastic change of the sample stoichiometry (loss of Mg atoms) was exhibited, without noticeable Cs diffusion up to 1500°C (below concentrations of 3-4 $at.$ %).

The formation of radiation induced defects via electronic excitation in $MgAl_2O_4$ and their stability were studied by TEM [64]. It was observed that small interstitial-type dislocation loops dissociated into isolated interstitials under electron-induced electronic

excitation. The elimination rate of the loops was found to be one order higher than for α-alumina. The disappearance of dislocation loops by a dissociation mechanism into isolated interstitials was discussed through analysis of the growth-and-shrink process of the loops. HARECXS analysis on cross section specimens irradiated with 350 MeV Au ions showed the progress of cation disordering along ion tracks to be a function of electronic stopping power, $(dE/dx)_e$. Cations were found to exchange their sites toward a random configuration. Such disordering appeared from $(dE/dx)_e = 10$ keV/nm, and increased in size with increasing $(dE/dx)_e$ to reach nearly 10 nm in diameter at 30 keV/nm, under an assumption of a fully disordered configuration.

Behaviour of urania under irradiation

Point defect clusters and dislocation loops produced in bulk uranium dioxide by fission damage were studied by transmission electron microscopy [65]. In this work, clusters of 25 Å in diameter were first observed at a dose of 4.3×10^{15} $fissions/cm^3$. With increasing dose, these clusters quickly grow into resolvable prismatic dislocation loops. At high doses the loops grow and coalesce to form a network of dislocations, but at a dose of 1.6×10^{20} $fissions/cm^3$ and a post-irradiation anneal at $1100°C$, a new set of dislocation loops was observed to form between the existing dislocation network while a second set of dislocation loops is thought to be formed from the collapse of platelets of vacancies.

The radiation damage induced by 10 keV energetic recoils in UO_2 was investigated by molecular dynamic simulations [66]. The results revealed that, the effects of the PKA direction on the numbers of displaced atoms and Frenkel pair versus time was not observed. Most of the displaced atoms did not result in defects. 77 % and 96.3 % of the displaced uranium and oxygen atoms located at crystalline positions, creating replacements. The numbers of oxygen Frenkel pairs was about 2.5 times higher than the uranium Frenkel pairs. 89.5 % of the total interstitial clusters were composed of the cluster involves $2 - 3$ point defects. The fractions of vacancies and interstitials in clusters are 65.6 % and 44.5 %, respectively.

Nogita et Une investigated by High-resolution TEM the small intragranular bubbles in the outer region of high burnup UO_2 pellets. The results reported the presence of 4-8 nm size $Xe - Kr$ bubbles [67].

Nogita et al. [68] studied the irradiation effects in UO_2 polycrystalline due to 100 MeV Iodine ions (stopping power at surface is 23 keV/nm) over a fluence range of 1×10^{14} to 2×10^{15} cm^{-2}. The surface of the specimens was analyzed by scanning electron microscopy (SEM) and X-ray diffractometry (XRD), and then the depth profiles of incident iodine ions and defect clusters were measured by secondary ion mass spectrometry (SIMS) and transmission electron microscopy (TEM), respectively. Lattice parameter change,

which is associated with point defect accumulation, increased with ion fluence. Defect clusters of dislocations and dislocation loops were recognized, and their depth profiles were in good agreement with the calculated damage profile. These profiles of iodine ions and dislocation loops in both UO_2 and $(U, Gd)O_2$ were discussed in terms of inelastic and elastic collisions.

Sonoda et al. [69] investigated the $210 - MeV\ Xe$ implanted UO_2 to fluence of $5 \times 10^{11}\ ion/cm^2$. By the cross-sectional observation of UO_2 under at $300°C$, elliptical changes of fabricated pores that exist till $\sim 6\ \mu m$ depth and the formation of dislocations have been observed in the ion fluence over $5 \times 10^{11}\ cm^{-2}$ (figure 1-8). The drastic changes of surface morphology and inner structure in UO_2 indicate that the overlapping of ion tracks will cause the point defects, enhance the diffusion of point defects and dislocations, and form the sub-grains at relatively low temperature.

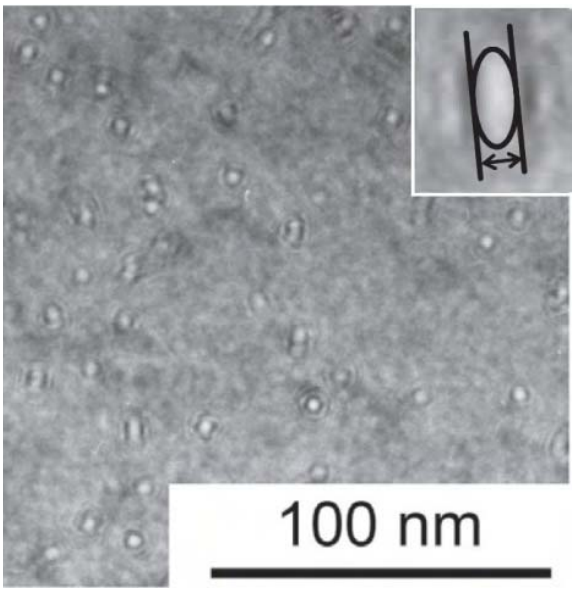

Figure 1-8: Typical images of ion tracks in UO_2 under irradiation with 210 $MeV\ Xe^{14+}$ ions to fluence of $5 \times 10^{11}\ cm^{-2}$ at room temperature [69].

Sonoda et al. [70] carried out an investigation in order to identify the conditions of the rim structure formation as a function of burn-up and temperature in which UO_2 fuel disks were irradiated at four thermal conditions, between 400 and 1300°, and at four different burn-ups, between 36 and 96 MWd/kgU. The SEM observations revealed the transition from original to sub-divided grains of rim structure and indicated that the burn-up threshold is between 55 and 82 MWd/kgU. Polyhedral sub-divided-grains with size ranging between 0.5 and 2 μm are clearly observed. TEM observations of restructured samples show that most of sub-grain boundaries are low angle and are heavily decorated by fission gas bubbles in the range 3.58 nm. In the non-restructured samples, dislocations and small precipitates are present.

Matzke et al. [71] studied UO_2 irradiated with different swift heavy ions using wide ranges of energies and fluences from 72 MeV to 2.7 GeV in the range 5×10^9 to 10^{17} cm^{-2}. This work showed that the formation of visible track in UO_2 is observed solely when the stopping power of fission products exceeds the threshold energy loss for track formation in UO_2 which could be determined to be in the range 22-29 keV/nm. Fission products of fission energy are below this threshold but nevertheless form thermal spikes in UO_2. Observable tracks are only found at the surface. By using $^{127}I^-$ beams of 72 MeV energy the consequences of fission product impact, i.e., lattice parameter increase, fission gas bubble formation, resolution of fission gas from bubbles and fission-enhanced diffusion were all observed and measured. The swelling of UO_2 was confirmed to be small and the technologically important process of polygonization (grain subdivision, also called rim-effect in operating UO_2-fuel) could be simulated.

In 1997, Wiss et al. [35] investigated specimens of sintered UO_2, irradiated with heavy ions (^{129}Xe, ^{238}U) with different fluences (5×10^{10} to 7×10^{13} cm^{-2}) and energies (173 MeV for Xe ions to 2.713 GeV for U ions). The influence of the electronic energy loss on the mechanisms of damage formation was studied in the range of 29 to 60 keV/nm. Tracks produced by U ions of 2713 and 1300 MeV and by Xe ions of 173 MeV were observed by TEM. The radii of the observed tracks were calculated using a thermal-spike model, taking into account the thermodynamic parameters of the material and the energy and velocity of the incoming ions. Figure 1-9, issued from this work, presents evolution of the temperature in the vicinity of uranium ion as a function of temps after their passage and as a function of the radial distance with respect to the trace of ion.

Figure 1-9 show that the temperature increases rapidly between 10^{-15} and 10^{-13} seconds just after the passage of ion. Afterwards, the diffusion of heat leading to the decrease of temperature is observed until 10^{-10} seconds. The maximum temperature is observed to be much higher than the melting point (3073 K) and is located in a narrow zone of 4 nm around the ion's path. This similarity in size between the experimentally observed diameter and the molten zone clearly indicates that the track is formed by a local (and likely instant) melting of the fuel in the close vicinity of ion's trajectory.

UO_2 single crystal implanted with 340 MeV Xe ion was studied by Garrido et al. in 1997 [72]. RBS/C was applied to study the structural transformation of UO_2 crystal under irradiation. This work reported the good stability of the crystalline structure under irradiation. The observed damaged volume fraction derived form this work is lower compared to the theoretical value. The result demonstrates that strong recombination takes place also under irradiation in the electronic stopping regime, which additionally confirms the stability of the UO_2 structure.

The radiation stability of urania single crystals submitted to intense electronic exci-

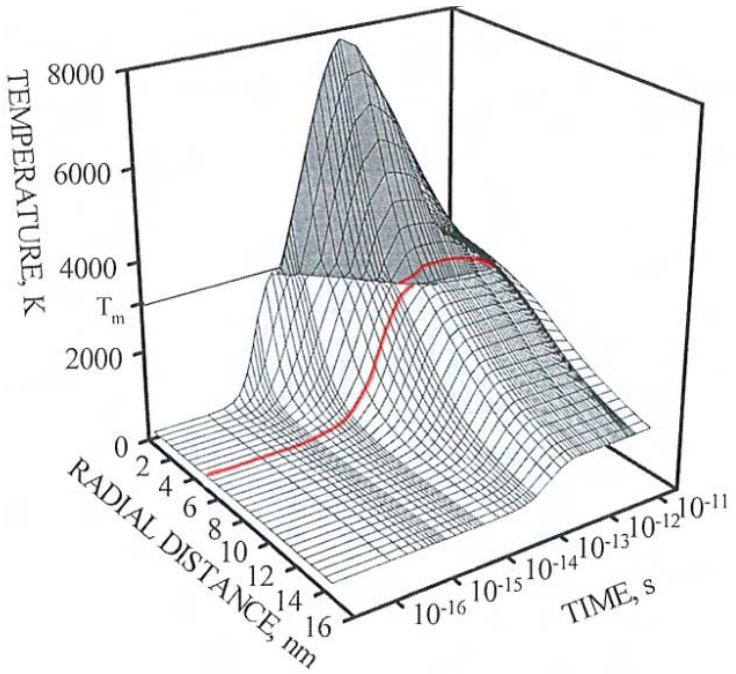

Figure 1-9: Calculated evolution of the UO_2 radial temperature distribution along a track in UO_2 as a function of time. The calculations are for 11.4 MeV/u U ions in the first nm of the target, i.e. $dE/dx = 60$ keV/nm with $\lambda = 6$ nm and a melting temperature of $Tm = 3150$ K [35].

tations induced by $944 - MeV$ Pb^{53+} ions was investigated with various analytical tools (TEM, AFM, RBS/C, XRD) to examine the modifications induced at the surface and in the crystal bulk [73]. At low fluence irradiation leads to the formation of localised ion tracks whose centre is hollowed in the surface region over a depth of ~ 100 nm and to the formation of nanometer-sized hillocks. Both features were resulted from an ejection of matter in the wake of the projectile. Track overlapping at high fluence results in the formation of micrometer-sized domains (~ 50 nm) in the crystal bulk characterised by a slight disorientation ($\sim 0.2°$) with respect to the main crystallographic orientation of the crystal.

In another work, Garrido et al. studied urania single crystals implanted with low-energy inert gases (He and Xe) [74]. The damage in-growth, due to both ballistic and chemical contributions, was investigated by in situ RBS/C experiments in the channelling mode and TEM. This work reported two main steps in the disordering kinetics for both inert gases. Relevant key parameters were found to be: the number of displaced lattice atoms created by the slowing-down of energetic ions during the implantation process; the concentration of noble gas atoms in the solid which cause the formation of large stress fields surrounding gas aggregates. The first step was reported to be due to the radiation effect scaled with the number of displacement per atoms while the second step due to the formation of inert gas bubbles at high implanted concentration.

In an interaction, ions can knock matrix atom out of their regular lattice location (Primary Knock-on Atoms, PKA). The PKA atoms in turn interact with all surrounding atoms and displace these atoms out of their location if they transfer enough energy to surrounding atom(s) [75]. A collision cascade is induced. Van Brutzel et al. [76] have studied this mechanism by Molecular dynamic by simulating the UO_2 irradiated with 80 keV U ion. The result is shown on figure 1-10. As it can be seen from the figure, 2.15 ps after the collision cascade starts, many atoms are displaced. After the equilibrium is reached, at 20 ps after injection of a PKA, the reorganisation of the crystalline structure takes place and only few Frenkel pair defects are eventually created.

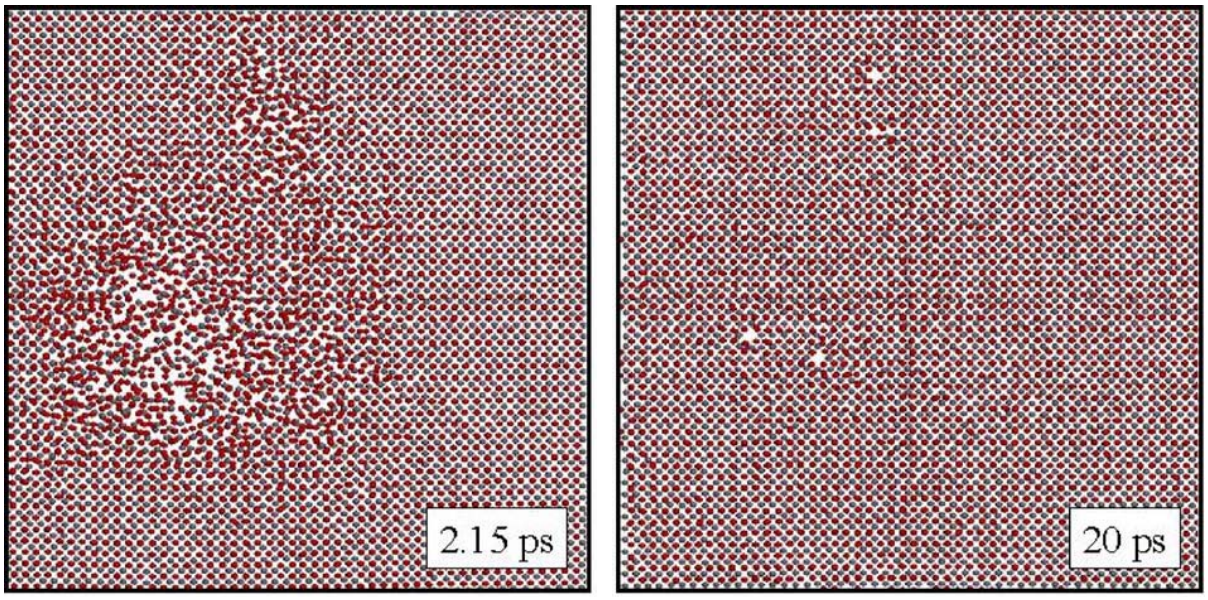

(a) (b)

Figure 1-10: Molecular dynamic simulation of displacement cascade induced by $80 - keV$ U ion irradiated in UO_2 at two different times: (a) at 2.15 ps after injection and (b) at 20 ps corresponding to the very end of the cascade [76].

Investigation by Transmission electron microscopy (TEM) were performed on a set of UO_2 thin foils by Sabathier et al. [77]. In this work, the sample were implanted with 390 keV Xe^{3+} and 300 keV Cs^{2+} ions. The results reveal the nature and quantity of defects formed as a function of Xe and Cs ion fluences. It is reported the results do not appear to be dependent upon the nature of the implanted ions. In addition to dislocation and dislocation loop formation, Xe and Cs aggregates were observed. At several Xe and Cs concentrations, the threshold temperatures for aggregate formation were determined. At concentrations of 0.4 at. %, Xe precipitation occurred above 870 K. The threshold temperature for Xe precipitation decreased to 670 K for the higher concentration samples (2 at. %) and to 770 K for Cs implanted samples at this concentration. No significant differences in the bubble size and densities were observed between the high concentration Xe or Cs samples. The aggregates formed were in the nanometer size range.

Another investigation by Transmission electron microscopy (TEM) experiments were devoted to the study of the evolution of the xenon aggregate population with increasing implantation fluence [78]. A thin UO_2 foil was implanted at fluences ranging from 3×10^{12} to 7×10^{14} cm^{-2} with 390 keV Xe^{3+} ions at 873 K. The results reported the presence of nanometer size bubbles above a fluence of 6×10^{12} Xe/cm^2 and an increase in the bubble density was observed between 6×10^{12} and 2×10^{14} Xe/cm^2. Above 2×10^{14} Xe/cm^2, the density saturates at $4 \times 10^{23} \pm 0.5 \times 10^{23}$ m^{-3}.

The fission gas release mechanisms was studied by Marchand et al. [79]. by decoupling thermal and irradiation effects and by assessing the Xenon behavior by profilometry. The samples were first implanted with $800 - keV$ ^{136}Xe then annealed either in the temperature range 1400-1600° or by irradiated with heavy energy ions ($182 - MeV$ Iodine) at room temperature, 600° or 1000°. It is reported that Xenon is mobile during irradiation at 1000° while, in contrary, thermal treatments do not induce any Xenon migration process: these results were also reported to correlate to the formation of Xenon bubbles observed by Transmission Electron Microscopy.

In summary, the radiation effects on ceramics materials have been intensively investigated. The investigation was performed to study the effects due to various irradiation conditions such as the nature of ions, energies (effects due to electronic versus nuclear stopping processes), temperature, etc. Many experimental techniques have been applied for the characterisation of irradiated materials including Transmission Electron Microscopy (TEM), X-ray diffraction analysis (XRD), Rutherford Backscattering Spectrometry in Channelling geometry (RBS/C), etc. The investigations show that ceramic materials have high resistance to irradiation. The crystalline to amorphised phrase transformation was reported only for YSZ crystal irradiated with $400 - keV$ Cs ions at room temperature to extremely high fluence of $\Phi = 10^{17}$ cm^{-2} [43]]. Nevertheless, the concentration of Cs at which amorphisation of YSZ took place is about 8 at. %, far larger than typical value that could be reached in a fuel matrix.

UO_2 crystalline structure submitted to irradiation was also studied but no amorphisation was ever reported. However, the presence of inert noble gases was clearly reported [77, 78, 79, 80]. This phenomenon could lead to a strong structural destabilisation in case of high density noble gas bubbles presenting in the matrix. Nevertheless, a detailed comparison of radiation effects due to insoluble versus soluble species (for instance of typical fission products) was never done. Such a comparison will help understand the complete behaviour of UO_2 structure submitted to irradiation of different conditions such as the effects of the solubility. This question gives rise to a research topic that has been carried out in the framework of this thesis. The following chapters of this thesis will present the investigation of the radiation effects in UO_2 single crystals submitted to irradiation of

low-energy ions. The thesis focused especially on the comparison of the effects induced by typical fission products of close masses and atomic numbers but different solubilities in UO_2. This thesis also deals with the effects of doping of impurities to very high concentration particularly the doping of an inert noble gas to about 10 at. %.

Chapter 2

Methodology

Investigation of the radiation effects on a materials can be performed in several way. In order to study the radiation effects in a real situation, samples can be putted in the reactor core where they will be bombarded by neutrons at high flux, by fission fragments at typical energy of 70 MeV, by α particles and heavy recoil nuclei. However, the eventual radiation effects on the samples is a complex process due to the integration of various types of irradiations with different initial energies. It is quite impossible to understand the effects at different condition such as the effects of low versus high energy particles (nuclear versus electronic mechanisms), the effects due to irradiation by particles of very different masses... Moreover, such investigation are very difficult to perform due to the high radioactive level of the samples as they were implanted with highly unstable fission fragments. An alternative approach that is usually followed to investigate the radiation effects in a material is to irradiate the material by an accelerated ion beam then study by various experimental techniques.

2.1 Experimental simulation of the radiation effects in nuclear fuel

Investigation of the nuclear real fuel (spent fuel) is a challenge due to various reasons. One of the main challenge that could lead to a difficulty in investigating the nuclear fuel lies in the high level of radioactivity of the sample. After a long time operation in the reactor core, the genuine fuel's composition changes due to the incorporation of newly created elements including fission fragments and minor actinides. These elements are highly unstable that disintegrate afterwards via β^- and α emission enclosed with energetic gamma rays. The radioactivity of the spent fuel is therefore a parameter that strongly limits the investigation. For instance, such investigation of the spent fuel requires special equipments and regulations that presents as a one of the most important challenge due to the high cost of safety.

Fortunately, those difficulties could be avoided by investigating a material that models the nuclear real fuel submitted to external accelerated irradiation. Moreover, by using an accelerated ion beam, the investigation could be performed with a well defined irradiation conditions that is very useful for understanding the fundamental mechanisms of

radiation effects such as the choice of nature and energy of irradiation, the temperature at which the investigation if performed, the accumulated implantation fluence, irradiation flux... Such option is the investigation of the natural or depleted UO_2 that does not contain any radioactive elements mentioned above.

In this work, the experimental simulation has been done in order to investigate the structural destabilisation of the nuclear fuel (i) due the effects of the irradiation with low-energy ions and (ii) due to the doping of the foreign elements, especially at high incorporated concentration. The samples that simulate the nuclear fuel (depleted UO_2 (0.3% ^{235}U) single crystals) have been irradiated with external accelerated ion to simulate the radiation effects and to simulate the effects due to the doping of the insoluble versus soluble fission products. Irradiated samples are characterized by various investigating techniques including the Rutherford Backscattering Spectrometry in Channelling geometry, the X-Ray diffraction and the Transmission Electron Microscopy.

2.2 Samples preparation

The first step in the investigation is the preparation of the samples. Uranium dioxides (0.3 % ^{235}U) single crystal of $\langle 100 \rangle -$orientation has been used as simple model to modelise the nuclear fuel for investigating the effects of ion irradiation. The samples were first cut off from a block with the crystallographic orientation being specified by Laue X-Ray crystallography method. They were then mechanically polished until mirror-liked finish using diamond paste down to $0,5\ \mu m$. Afterwards, the samples underwent the annealing process in the environment containing the mixture of H_2/Ar gases of 10% H_2 at $1400°C$ in order to remove any defects created during cutting and polishing processes and to fix the stoichiometry ratio of U/O to 1/2[1]. The quality of the crystal was then checked by Rutherford Backscattering and Channelling (RBS/C) technique on un-irradiated crystals. Theoretical value of the ratio of minimum axial over random yields for a virgin crystal is $\chi_{min} \sim 1 \div 2$ %.

2.3 Experiments

The samples are then irradiated with well-defined ions condition (nature and energy of ion) at room temperature at the JANNuS facility at CSNSM laboratory at the University Paris-Sud at Orsay France using a 190 kV implanter IRMA. The crystals to be irradiated were glued on a special sample holder making 7° tilting angle with respect to the main crystallographic orientation of the crystals to prevent any channelling of bombarding ions. Irradiations were made with accumulated fluence ranging from 1×10^{14} cm^{-2} to 8×10^{16} cm^{-2} (which corresponds to a concentration of incorporated impurities

[1] $UO_{2+x} + xH_2 \xrightarrow{H_2/Ar\ environment} UO_2 + xH_2O$

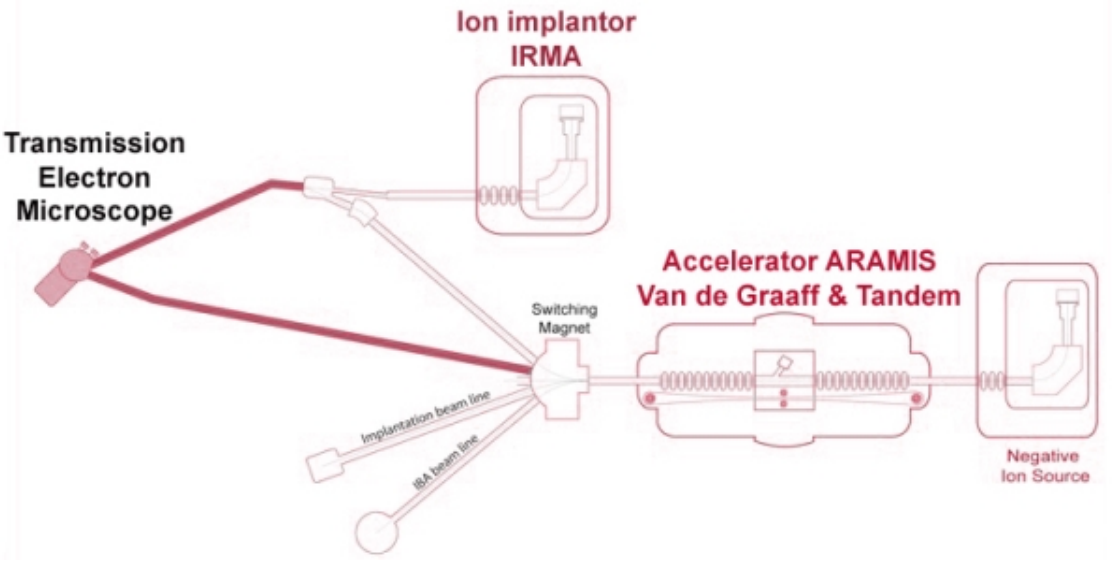

Figure 2-1: JANNuS nuclear facility, located at Orsay and managed by the **"Centre de Sciences Nucléaire et de Sciences de la Matière" (CSNSM)**, belongs to CNRS-IN2P3-Université Paris-Sud. It couples a 2 MV Tandem accelerator (ARAMIS) and a 190 kV ion implanter (IRMA) to a 200 kV Transmission Electron Microscope (TEM FEI Tecnai G^2 20).

ranging from 0.01 to 10 at. %). Implantations were made with the ions flux always kept below 5×10^{11} $cm^{-2}s^{-1}$ to avoid any significant heating of irradiated samples. After each fluence step, the samples were characterised *in situ* by the RBS/C technique; Details introduction to the RBS/C technique will be given in section 2.4.1.

SRIM calculation was made in order to estimate the stopping and range of projectiles in UO_2. Results obtained from SRIM calculation were also used to calculate the number of displacements per atom (*dpa*) induced during the irradiation. The number of displacements per atom is very helpful when comparing the radiation effects of low-energy ions of different conditions. Calculation was done assuming the displacement thresholds for uranium and oxygen sub-lattices are $E_d(U) = 40$ eV and $E_d(0) = 20$ eV, respectively [81]. The calculated depth-distribution of implanted ions is applied to compute the maximum fraction of doping ion (the concentration of implanted impurities); a useful parameter for comparing the effects of doping to high concentration. Details of SRIM calculation and results can be found on Table 2.1 while the transformation from fluence to *dpa* and fraction of implanted species will be shown in section 3.2.

Although being used as the nuclear fuel for decades, the destabilisation of UO_2 due to the radiation effects and due to the chemical effects is still not fully understood. For instance, the incorporation of fission products up to high concentration could leads to the polygonisation of the high burn-up fuel's structure close to the periphery of the fuel pellet; this phenomenon is referred to as the formation of the High Burn-up structure. The present work investigates the destabilisation of the urania crystalline structure due to the

Ions (Implante isotope)	Z	Mass (u)	Energy (keV)	Range $Rp(nm)$	Range straggling $\Delta Rp(nm)$	Nuclear stopping $Sn(keV/nm)$	Electronic stopping $Se(keV/nm)$	dpa max	Fraction of implanted ions at max (at. %)
$^{131}Xe^{3+}$	54	130.905	470	83	39	3.33	0.61	615	10.04
$^{139}La^{3+}$	57	138.906	500	86	41	3.60	0.42	681	9.56
$^{140}Ce^{3+}$	58	139.905	500	85	41	3.67	0.42	676	9.62

Table 2.1: Summary of physical properties and relevant characteristics of implantations performed in UO_2 single crystals. Range and range straggling are calculated by SRIM program assuming the displacement thresholds for uranium and oxygen sub-lattices are $E_d(U) = 40\ eV$ and $E_d(0) = 20\ eV$, respectively [81]. The stopping power is calculated at indicated initial energy of ions The maximum dpa and concentration are calculated for highest expected fluence of $\Phi = 8 \times 10^{16}\ cm^{-2}$

irradiation of a fission product liked elements at the end of their range when the process of defect creation is essentially elastic collision (the so-called ballistic contribution). Moreover, since fission fragments slow down and finally stay in the solid, the effects of their incorporation at high concentration (the so-called chemical contribution, as the incorporation of a fission product eventually modifies the chemical composition of the genuine fuel) are investigated in parallel. For that purpose, the elements of similar masses and atomic numbers have been deliberately chosen in order to investigate both the creation of defects due to nuclear stopping process and due to the incorporation of soluble (La, Ce) versus insoluble (Xe) species in UO_2 single crystals.

2.4 Techniques for characterisation

2.4.1 Rutherford Backscattering Spectrometry

Several experimental techniques can be used for characterizing the defects of the material. Amongst them, Rutherford Backscattering and Channelling (RBS/C) technique represents the outstanding feature which is convenient in material science [82, 83, 84, 85, 86, 87, 88]. Such that conveniences could be the ability of well identifying and quantifying the compositions, the capability of profiling the depth distribution of defects and the ability to localize the impurities in a material.

Rutherford Backscattering Spectrometry (RBS)

RBS is a technique which is based on the elastic nuclear interaction between the projectile and target nucleus. Light elements such as Hydrogen or Helium are usually used as projectile because they figure the least destructive elements to the structure. The energy of projectile ranges from few hundreds of kilo electron volts to few mega electron volts which, as a consequence, results in the analyzed depth up to few micrometers. Typically, in this research, we investigate the effects in the limits of few micrometers from the surface of the material which is totally in consistency to the technique.

The principle of RBS is demonstrated in figure 2-2. An incident beam of energy E_{c1} is directed to the material. After interaction with lattice atoms, this ion beam scatters in all directions. A detector is placed at angle θ with respect to the incident beam to detect ions that backscatter in that direction. Knowledge of the energy $E'_{c1}(x)$ of the backscattered ion is a crucial parameter of the technique. It helps us identifying the nature of target atom and the depth at which target atom locates. Besides, the number of detections on specified elements allows one to determine the stoichiometry ratio of all elements constituting the material [89].

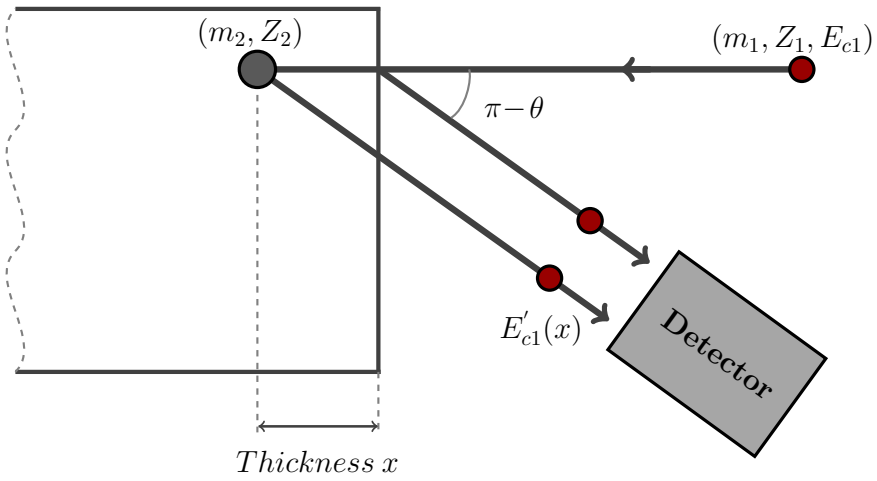

Figure 2-2: RBS geometry

Scattering cross section

The applicability of the technique depends strongly on the scattering probability of the projectile. This probability is characterized by the cross section of the scattering reaction $d\sigma/d\Omega$ in the solid angle $d\Omega$ along direction θ. In the theory of Rutherford interaction, this cross section is calculated as following [89]:

$$\frac{d\sigma}{d\Omega} = \frac{1}{4\pi\varepsilon_0} \times \left(\frac{Z_1 Z_2 e^2}{4E}\right)^2 \times \frac{4}{\sin^2\theta} \frac{\left\{\left[1 - (m_1^2/m_2^2)\sin^2\theta\right]^{1/2} + \cos\theta\right\}^2}{\left[1 - (m_1^2/m_2^2)\sin^2\theta\right]^{1/2}}$$

where Z_1, m_1 and Z_2, m_2 are respectively the atomic number and mass of projectile and target. ε_0 is the vacuum permittivity. E is the energy of incident particle, e is the elementary charge and θ is the scattering angle.

This formula says that the cross section of the Rutherford scattering reaction is inversely proportional to the square of energy of incident particle. This means that the more energy the particle possesses the smaller the scattering cross section is. It is worth noticing from this formula that, the cross section is proportional to the square of atomic number of target atom. As a result, in a compound the sensitivity of the technique to

light element is much smaller compared to heavy element. The signal recorded on light element which overlay on the signal due to heavy element is quite low and unable to be separated from background signal. Light element is seemingly undetectable in compound with heavy element.

A series of *in-situ* experiments were conducted in which a $\langle 100 \rangle-$oriented UO_2 crystals were alternately irradiated and characterized by RBS technique in channelling geometry (see next section) using a $3,085 MeV$ He^{2+} ion beam. Helium was chosen because it is a light element which turns out to be less deleterious as compared to heavier element and because the backscattering of light element is more efficient than heavy element. The energy was chosen to detect uranium cations and to benefit the resonance of interaction $He + {}^{16}O \rightarrow {}^{20}Ne^{*} \rightarrow {}^{16}O + He$ for enhancing the detection on oxygen sub-lattice [90, 91].

Channelling

Channelling is a technique that applies the principle of RBS only on single crystal. The importance of channelling technique is that the well aligned crystalline lattice site target atoms in the material are not seen as diffraction grating as in the case of X-Ray diffraction technique. They are practically viewed as rows or planes of periodically repeated atoms between which ion channels (figure 2-3). The channelling results in the much smaller number of detections of backscattered ions as most of ions channel through the crystal with low probability to be backscattered. Only a small fraction (about 1%) of backscattered event is recorded compared to the situation in which ion beam is randomly oriented towards the crystal.

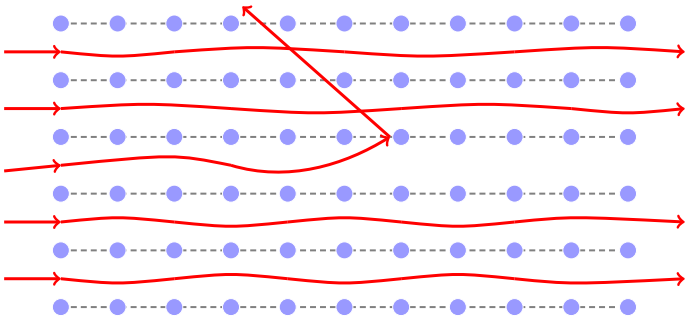

Figure 2-3: Sketch of channelling phenomenon

Figure 2-4 display a typical spectra recorded by RBS and channelling technique. Three different spectra represent the backscattering spectra in three different conditions. The random spectrum (blue line) is obtained when the incident beam is randomly oriented towards the crystal. In this configuration, the backscattering signal is quite high as the probability for the backscattering of incident ion is high. Random spectrum is usually recorded by rotating the crystal around incident beam by a certain open angle. In such

case, the spectrum can be named as a rotating random spectrum.

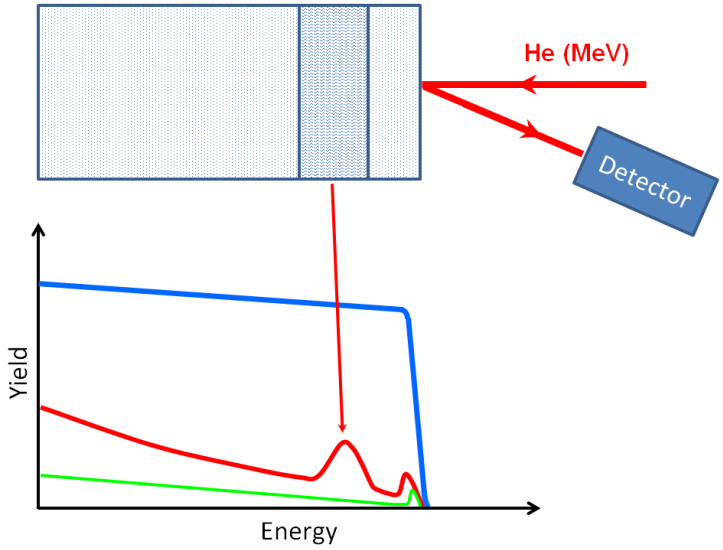

Figure 2-4: Typical channelling spectrum recorded on a crystal containing defects in a region of the crystal (red). Blue line represents the random spectrum and the green line represents the channelling spectrum recorded for perfect crystal.

When the ion beam is oriented along the crystallographic orientation of a perfect crystal (without any presence of defect), the backscattering events decrease dramatically as most of incident ions channel through the crystal. In this configuration, only a very small fraction of ion scatters on the lattice atoms and the consequential backscattering spectrum presents a very low signal as compared to the random spectrum. The green curves shown on figure 2-4 illustrates such channelling spectrum issued from a non-defective crystal. The ratio of backscattering yield of the axial channelling spectrum over that of the random spectrum integrated in a given energy windows is known as the minimum axial yield (χ_{min}). The theoretical value of χ_{min} for a perfect crystal is typically between 1 and 2 % depending on crystals.

If the ion beam is oriented along the crystallographic orientation of a crystal containing defects, the backscattering will be improved as compared to the perfect crystal. As the defects are present in random position within the crystalline structure, they function as both direct and indirect obstruction to the channelling of the incident beam. The obstruction to the incident ion beam at a given depth from the surface of the crystal is proportional to the local concentration of defect. The crystal containing defect will result in the higher channelling spectrum compared to the virgin crystal. The red curve represented on figure 2-4 is a typical example of the channelling spectrum recorded on defective crystal. As it can be seen, the spectrum consists of: (i) a surface peak due to the backscattering of ion upon atoms located at the surface of the crystal; (ii) a damage peak results from direct backscattering upon atoms that have been randomly distributed

within the lattice structure (the level of the observed damaged peak directly represents the local concentration of disordered atoms at given depth); and (iii) a de-channelling signal owing to the small angle scattering of incident ion upon both lattice atoms and defects. Actually, lattice atoms and defects along a channel contribute to the deviation of the incident ions by a small angle and the integration effect eventually kicks ions out of the channel. At this stage, ions will be scattered in all direction including the direction where the detector is placed. One backscattering signal is hence recorded.

Depth scaling

The depth profiling of RBS/C requires the necessity of relating the energy of the backscattered ion to the depth in the sample at which the backscattering takes place [92]. This relation depends on the energy loss of ion while crossing the sample, on the kinematic factor of the scattering and on the angle formed by the incident beam and by the detector's normal vector. The depth scaling is then estimated by assuming that the stopping powers on the way in as well as on the way out are constant (the so-called surface approximation). Therefore, the energy of detected ion that backscatters at depth x from the surface can be given as following:

$$E(x) = KE_\circ - xS.$$

Where, $E(x)$ is the detected energy of ion that backscattered at depth x, $E_\circ$ is the initial energy of the incident beam and S is the energy loss factor. In this formula, S is calculated as following (with the help of knowledge of the kinematic factor, scattering angles and the incoming and outgoing stopping powers assuming that the stopping in random and aligned directions are the same):

$$S = K\left(\frac{dE}{dx}\right)_{in}\frac{1}{\cos\theta_1} + \left(\frac{dE}{dx}\right)_{out}\frac{1}{\cos\theta_2}$$

Thus the depth at which the backscattering takes place will be:

$$x = \frac{KE_\circ - E(x)}{S}$$

Finally, a distribution of defects versus depth can be well constructed.

2.4.2 X-Ray diffraction

Principle

The X-Ray radiation is generated when bombarding an anode by an electron beam produced by a Tungsten filament under vacuum. It can be generated also when high speed electron beam or high energy charged particles decelerate suddenly. The generation of

X-Ray is made via the emission of a photon of energy on the order of magnitude keV when an electron at the outer shell, e.g. L shell, falls down to the K shell from which another electron has been kick off by the bombarding beam. This configuration leads to the generation of an X-ray called K_α radiation. X-rays are actually considered as an electromagnetic wave that have a wavelength in the range of 0.01 to 10 nm, corresponding to frequencies in the range 3×10^{16} Hz to 3×10^{19} Hz and energies in the range 100 eV to 100 keV. X-rays have a much shorter wavelength than visible light, which makes it possible to probe structures much smaller than what can be seen using a normal optical microscope. However, not all X-Ray can be used for diffraction experiment. As the typical lattice spacings (d_{hkl} between atomic planes of a given orientation) are between 2 and 3 Å, the wavelength of the X-Ray has to be smaller than twice the lattice spacing but should not be two small otherwise θ (the angle formed by the incident ray and the crystal's surface) is too small to be observed. Therefore, the wavelength of X-ray is usually between 0.5 and 2.5 Å for the use in material characterisation.

Bragg condition

X-ray crystallography can be used to study the crystalline structure and to determine the positions of atoms in crystals. When directed on a periodically arranged solid (a crystalline structured solid), in given direction, constructive interferences give rise to scattering of X-rays in a coherent way. For this diffraction phenomenon to occur, the inter-planar spacing d_{hkl} and diffracted angle have to satisfy the Bragg condition, i.e.

$$2d_{hkl} \sin \theta_B = n \cdot \lambda$$

where θ_B is the Bragg angle; λ is the wavelength and n is an integer that represents the diffracting order. Once the Bragg condition is satisfied, it can allow one to determine (i) the atomic planar family that is the responsible to the diffraction and (ii) the inter-planar distance between two adjacent atomic planes. Since the wavelength and the inter-planar distance are fixed, constructive interference will be observed, therefore, only at certain angle.

In order to observe the diffraction from a given lattice plane, the Bragg's law must be satisfied. This condition is often obtained by varying either the wavelength, λ, or the Bragg angle, θ. For a monochromatic X-ray beam, the only possible way is to vary the θ angle to meet the Bragg condition.

Laue condition

Bragg's law can also be rewritten under the following alternative form:

$$\sin \theta_B = \frac{n \cdot \lambda}{2d_{hkl}}$$

where the angles of diffraction are inversely proportional to the spacing of the reflecting planes in the crystal lattice. Therefore, it is usually helpful to establish a new coordinate system whose axes have the dimension of inverse length: The Reciprocal Space. The reciprocal lattice is therefore the inverse of the real lattice whose basic lattice vectors a^*, b^* and c^* are defined from the translation vectors in the crystal lattice:

$$\vec{a}^* = \frac{\vec{b} \times \vec{c}}{a \cdot b \cdot c}; \quad \vec{b}^* = \frac{\vec{c} \times \vec{a}}{a \cdot b \cdot c} \quad \text{and} \quad \vec{c}^* = \frac{\vec{a} \times \vec{b}}{a \cdot b \cdot c}$$

In the reciprocal space, the translation vectors $\vec{a}^*$, $\vec{b}^*$ and $\vec{c}^*$ are perpendicular to the planes indexing (100), (010) and (001), respectively. And if $\vec{H}_{hkl} = h\vec{a}^* + k\vec{b}^* + l\vec{c}^*$, which denotes a translation vector in the reciprocal lattice, then the ensemble of indices h, k and l represents one node in the reciprocal lattice and $\vec{H}_{hkl}$ is normal to the plane (hkl) in the real lattice and the magnitude of $\vec{H}_{hkl}$ is the inverse of the inter-planar spacing d_{hkl} between two adjacent (hkl) planes.

In the reciprocal space, the Bragg's condition can be rewritten differently as the Laue condition that can be derived as following:

Let us consider an X-ray, with the wavevector $\vec{K}_0$, is directed on a crystal and the diffracted X-ray wave has the wavevector $\vec{K}$. Assuming that the wavelength stays unchanged (which is true in the case of elastic scattering of a photon by an electron), the magnitudes of the wavevectors $\vec{K}_0$ and $\vec{K}$ are identical and equal to the inverse of wavelength:

$$|\vec{K}| = |\vec{K}_0| = \frac{1}{\lambda}$$

and the question raised is to what condition the relationship between wavevectors will the maximum constructive interference of the diffracted X-ray occur? Since the crystal is strictly periodic, it is sufficient to consider two atoms related by translation through a lattice vector $\vec{r}_{hkl} = h\vec{a} + k\vec{b} + l\vec{c}$ as illustrated on figure 2-5.

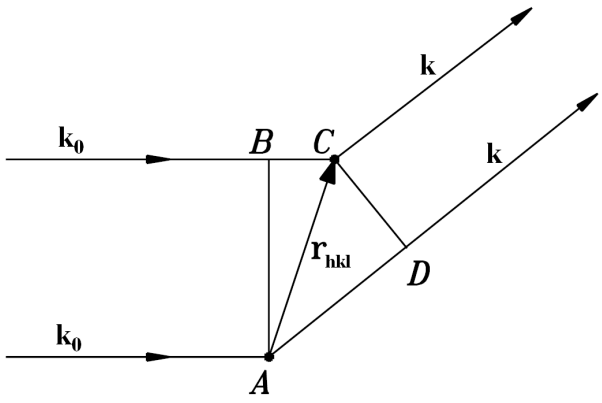

Figure 2-5: Derivation of the Laue diffraction condition

The waves diffracted from atoms A and C will result in maximum constructive interference if the difference between the optical paths is an integer multiple of the wavelength λ. As shown on figure 2-5, the optical paths difference is given by:

$$\Delta = AD - BC = \vec{r}_{hkl} \cdot \frac{\vec{K}}{|\vec{K}|} - \vec{r}_{hkl} \cdot \frac{\vec{K}_0}{|\vec{K}_0|} = \lambda \vec{r}_{hkl} \cdot (\vec{K} - \vec{K}_0)$$

Thus, the required condition must be satisfied is that the optical path equals a multiple of the wavelength, that is:

$$\vec{r}_{hkl}.\Delta\vec{K} = n$$

where $\Delta\vec{K} = \vec{K} - \vec{K}_0$ is called the scattering vector and n is an integer. This condition shows that diffraction takes place when the scattering vector $\Delta\vec{K}$ coincides with a reciprocal space vector $\vec{H}$ whose magnitude is equal to multiple of the distance between two nodes of a reciprocal space row, that is to say:

$$\Delta\vec{K} = \vec{K} - \vec{K}_0 = \vec{H}$$

Ewald's sphere

Laue condition can be figured following the construction of the Ewald's sphere. This construction, in turn, allows determination of the direction that results in the constructive interference of the diffracted beam. Ewald's sphere is defined by the center C and the radius R which is equal to the magnitude of the wavevector $\vec{K}_0$.

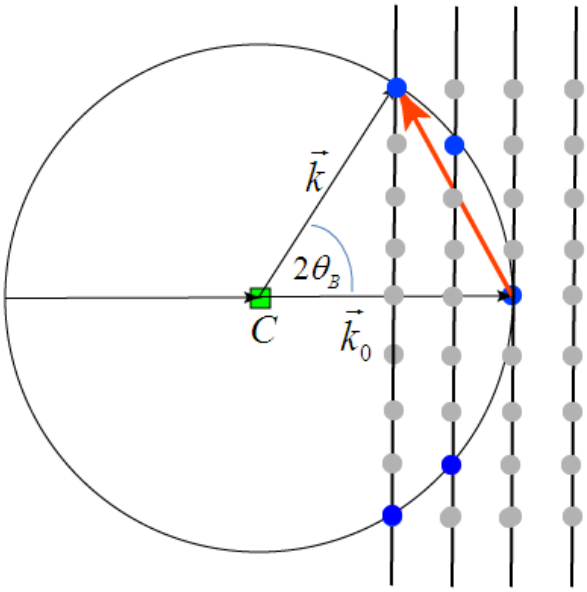

Figure 2-6: Construction of the Ewald's Sphere

As it can be seen on figure 2-6, the extremity of the diffracted wavevector locates

on the surface of the Ewald's sphere. As a convention, the extremity of the incident wavevector is considered as the origin of the reciprocal space, the condition for a constructive interference of diffracted beam is satisfied when the extremity of the diffracted wavevector coincides with a node in the reciprocal lattice space.

Symmetric geometry

The basic measurement geometry the most frequently used of x-ray diffraction instrument is the $\theta - 2\theta$ geometry including symmetric geometry. In the symmetric geometry, the angles of both the incoming and the exiting beam equal θ with respect to the specimen surface. The diffraction pattern is collected by varying the incidence angle of the incoming X-ray beam (θ) and the scattering angle (2θ) while measuring the scattered intensity I as a function of 2θ. Two angles vary during a $\theta - 2\theta$ scan and various types of diffractometers are in use. For one set of instruments, the X-ray source remains fixed while the sample is rotated around θ and the detector moves by 2θ. For other systems the sample is fixed while both the x-ray source and the detector rotate by θ simultaneously, but clockwise and anticlockwise, respectively. The diffraction on crystallographic planes that satisfy the Bragg condition yields a diffracted peak. This peak locates exactly at the angle 2θ and the shape of the peak can be a Gaussian or Lorentzian or more practically a combination of them, known as a Pseudo-Voigt. The enlargement of the peak is often observed and consists of two contributions: (i) the practical resolution of the goniometer and (ii) the intrinsic contribution of the investigated sample. The former one is unavoidable but identical in all measurements while the latter one is usually due to the presence of micro strains and/or finite size of crystallites.

Asymmetric geometry

In this geometry, the incident angle does not equal the scattering angle. This geometry is often applied to a scan known as the rocking-curve in which the angle between incident and diffracted beams is maintain to be equal to $2\theta_B$ while the incident angle varies around $2\theta_B/2$. In the real space, this geometry corresponds to the rocking of the sample around the direction of the vector $\vec{K}_B$ that is determined when $\omega = \theta_B$. $\vec{K}_B$ is the scattering vector at the maximum of the peak in a $\theta - 2\theta$ scan on the same-oriented plans. The scan in omega is similar to the situation where the module of the diffracted vector maintained constant.

In the framework of this thesis, the X-ray diffraction technique has also been applied to study the microstructural evolution and the elastic deformation of the UO_2 crystals submitted to irradiation with $500-keV\ Ce$ ions. 5 samples of $\langle 100 \rangle$ orientation and 5 samples of $\langle 111 \rangle$ orientation have been irradiated at JANNuS Orsay to the fluence of 1×10^{14}, 3×10^{14}, 5×10^{14}, 7×10^{14} and $9 \times 10^{14}\ cm^{-2}$. In this experiments, the implanted

samples were characterised at the *Institut des Sciences Chimiques de Rennes* in the University of Rennes 1. A Bruker D8 diffractometer equipped with a standard Cu tube was used. An intense and monochromatic beam of wavelength $\lambda = 0.15406\ nm$ was obtained by using a multilayer mirror behind the tube followed by a four-crystal monochromator (4×Ge220) in asymmetric configuration; the resulting primary-beam divergence was ~ 18 arcsec (0.005°). A 1D solid detector (LynxEye) was used to record X-ray scattered intensity; the point detector mode was used for recording scattering signals.

2.4.3 Transmission Electron Microscopy

The transmission Electron Microscopy (TEM) is a well established tool for studying crystallographic defects present in crystalline materials. Basically, a transmission electron microscope consists of an electron gun and an assembly of electromagnetic lenses mounted in a vertical column. The column is evacuated to a pressure better than $10^{-5}\ Torr$. The thin sample ($< 0.1\ \mu m$ thick) to be investigated is mounted on a goniometer capable of tilting the sample along two orthogonal axes so that an appropriate set of crystallographic planes can be brought into a diffracting condition. Since the wave-length of high energy electrons (e.g. wavelength of 100 keV electron is $\simeq 3.7 \times 10^{-3}\ nm$) is comparable to the magnitude of the lattice strain around a defect, a shadow is formed in the image when lattice planes affected by the defects are in diffracting condition. The resulting contrast in the image is called diffraction contrast. Owing to the small wavelength of electrons, TEMs are capable of imaging at a significantly higher resolution than light microscopes. This allows for the examination of very fine details in materials, down to a single column of atoms. In a typical modern microscope the final magnification of displayed images can be varied between 100 to several 10^6 times.

The electron microscope can be operated in two principal modes; imaging or diffraction. The electrons transmitted through the sample are brought to focus in the back focal plane of the objective lens, forming a diffraction pattern. In the image mode, the image formed by the objective is further magnified by the intermediate and projector lenses while in the diffraction mode, the intermediate lens strength is reduced so that the back focal plane of the objective is focused on the viewing screen, forming a diffracting pattern from the illuminated area of the specimen.

A Transmission Electron Microscope is ideal for a number of different fields of application amongst which the application in material science is widely seen. In the material science, the TEM is usually applied to study the structure of the material including crystalline material with the presence of defects. For example, TEM with *in situ* ion irradiation is unique among experimental techniques in that it allows the direct observation of the internal microstructure of materials on the nanoscale while they are being subjected

to irradiation. Invaluable insights into the underlying atomistic processes at work can be gained through direct observation of radiation induced and/or radiation enhanced effects such as: phase changes and segregation; mechanical and structural changes; compositional changes; grain growth and shrinkage; precipitation and dissolution; defect/bubble formation, growth, motion, coalescence, removal and destruction; ionization; diffusion; and collision cascades... There are two geometries used for analysis of the irradiated samples, namely in plan-view or as a cross-section. The plan view can offer images of the surface or at a certain depth that is not always straightforward to determine accurately. The cross section offers the possibility to observe the effects of irradiation in depth, knowing at the same time the exact location regarding the observable depth.

HRTEM is an imaging mode that allows the imaging of the crystallographic structure of a material at an atomic scale. At such small scales, individual atoms and crystalline defects can be viewed. As opposed to conventional microscopy, HRTEM does not use electron wave absorption by the sample for image formation. Instead, contrast arises from the interference in the image plane of the electron wave with itself. When the electron beam penetrates into the sample, the sample no longer changes the amplitude of the incoming electron wave function but does modify its phase, resulting in a phase-contrast imaging. In practice, this technique requires very high quality samples with ultra thin areas. It is important to note that the recorded image with this technique is not a direct representation of the sample's crystallographic structure. Image processing is usually needed afterwards for final interpretation.

Regarding the sample preparation, unfortunately a destructive method, the two modes of observation require two different methods of preparation. The plan view geometry requires mechanical back-thinning, using a tripod, until the edge of the sample reaches or is close to electron transparency; if required, the last step can be completed either by chemical etching or ion thinning at low incidence angle (in this case 8°). The sample preparation of cross section specimen is more complicated involving slicing of the sample in small pieces and gluing them together, surface against surface; then from the resulting block of material small square slices are cut so that the interface of interest lies in the middle of the piece. The steps then are the same as for a plan view sample with the additional difficulty of preferably thinning a very specific area, the area of interest close to the interfaces.

In the frame work of this thesis, some crystals were irradiated *ex situ* at selected ion fluences for investigation by Transmission Electron Microscopy. In order to obtain the images shown here a JEOL 3010 microscope was used. The microscope was equipped with a LaB_6 filament and can be operated at an accelerating voltage of 300 kV. A schematic drawing of the microscope is shown in figure 2-7. The choice of the microscope was driven

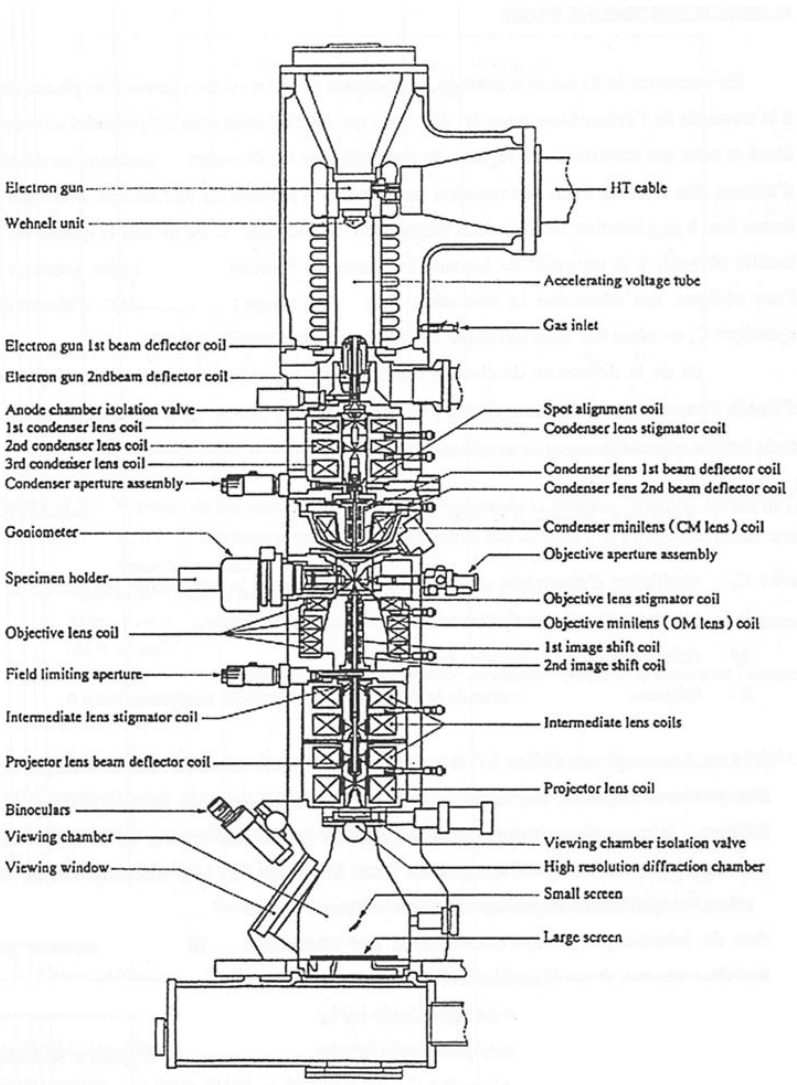

Figure 2-7: Schematic diagram of a High Resolution Transmission Electron Microscope.

by the necessity to use 300 keV electrons in order to obtain electron transmission through the UO_2 specimen; the microscope is designed for high resolution imaging, with a point resolution of 0.19 nm.

2.5 Computer tool

Ion channelling technique, for long time, is frequently used for measuring the structural defects located on the surface layer of a crystalline material over a typical depth of few μm. Experimental results obtained by this technique are usually composed of backscattering spectra measured only major axis and planes and angular scans. Interpretation of such data is by no way straightforward and the difficulty is present while extracting quantitative information from the spectra. A simplified channelling data analysis based on the two-beam approximation can be performed and the results obtained are usually considered to be sufficiently accurate. Moreover, such that approximation allows

us to have access to a quantitative measurement of defects versus depth assuming the presence of randomly displaced atoms but it becomes very difficult to apply for a material containing various classes of defects especially the problem arises in a crystal containing extended defects. In this situation, an ordinary method is no longer suitable and Monte-Carlo simulations performed on a computer seems to play the role [93, 94, 95, 96]. In this thesis we used the Monte-Carlo simulation code called McChasy developed at the Andrzej Soltan Institute for Nuclear Studies in Warsaw, Poland as a tool to analyse the channelling data.

2.5.1 Principle of Monte-Carlo simulation of channelling phenomenon

Monte-Carlo computation is a technique of calculating integrals by repeated sampling probability to obtain numerical results. In case of an ion-crystal interaction, the sampling is made at each atomic plane by calculating the probability of close encounter. In each calculation, the instantaneous distance between ion and surrounding atoms is taken into account and when it becomes small enough the nuclear interaction takes place. Due to the atomic thermal vibrations, this probability has a Gaussian-shaped distribution around a lattice location. In Cartesian coordinates xyz (assuming that the z axis coincides with the channelling axis), the probability P_i^j of close encounter with an atom located on plane j is given by [97]:

$$P_i{}^j = \frac{\cos\psi_i^j}{2\pi N u_A^2} \exp\left[-\frac{(x_i{}^j - x_A{}^j)^2 + (y_i{}^j - y_A{}^j)^2}{2u_A{}^2}\right]$$

where i is used to number the acts of sampling and (x_i^j, y_i^j) is the coordinates of ion at the plane j during sampling i while (x_A^j, y_A^j) is the position of target atom A at the plane j. u_A denotes the thermal vibration of atom A and ψ_i^j is the angle between projectile velocity vector and the channelling axis; N is the sampling number.

An integration that gives a statistical estimation of number of backscattering events corresponding to the depth z (in the $z, z + \Delta z$ depth interval) is given by:

$$K^A(z) = \sigma^A N_{tot} \Omega \sum_j \sum_i^N P_i$$

in which, σ^A is the Rutherford cross section, N_{tot} is the total number of projectiles and Ω is the open solid angle of detection. The summation is made for all acts of sampling and all atomic planes in the indicated depth interval. The "depth-spectrum" $K^A(z)$, i.e. the series of K^A values calculated for subsequent depth intervals, can be transformed to the energy spectrum by taking into account the energy loss of projectiles on the entrance

and exit paths. Such spectra, obtained for each element in the crystal, are finally added together to the final backscattering spectrum. In case the sampling is made uniformly at each atomic plane in the crystal, the random spectrum is produced. Since the accuracy of the Monte-Carlo calculation is proportional to the total number of projectile ($\sim \sqrt{N_{tot}^{-1}}$) it can be improved by increasing N_{tot}.

In order to simulate the channelling of ion, the most basic feature is the incorporation of the lattice structure. Since the channelling of ion takes place along a channel or between atomic planes, the lattice crystalline structure is usually viewed as composed of rows. This situation becomes realistic as long as the ion beam is oriented close to the considered direction (typically a few degree off). It is also advantageous that in this approach the next important interaction will generally be the next atom along the row. Taking into account this approach, many crystalline structures were incorporated in Monte-Carlo computational program. Another alternative approach to incorporate the lattice structure is made by providing the basic locations of atoms in a unit cell and all translation operators related to the crystal. By doing this, the program performs a search procedure to find the next lattice atom (or atoms) with which the projectile will interact.

Others features that are also important to the simulation are the experimental divergence of the ion beam around its main direction and the potential function which governs the ion-atom Coulomb interaction. The ion beam's divergence was generally implemented by using a distribution of the probability of finding projectile ion from the beam's centre while the Molière's approximation to the Thomas-Fermi screening function was most widely used as screening function since it provides a universal function and is reasonably accurate [98].

Thermal vibration of atoms plays also an important role in computational simulation. Typically, atoms are supposed to locate around its lattice location where the exact position is predicted by a Gaussian distribution having the width calculated from the Debye theory.

2.5.2 McChasy

McChasy (abbreviation for Monte-Carlo CHAnnelling SYmulation) is a computer computational program designed for calculating the ion-crystal interaction in channelling condition for a variety of crystalline structure including the fluorite-type structure exhibited by UO_2. Analysis by McChasy program is made with the following steps. In a very first step, it is mandatory to declare several parameters concerning (i) the crystal to be investigated (structure, chemical composition, thermal vibration of each component), (ii) the geometry of such RBS/C measurement (solid angle of detector, incident and backscattering angle, etc), (iii) the analysing beam (nature of analysing ion, energy,

beam divergence), (iv) the energy resolution (the factors that define the energy interval in one acquisition channel). In the second step, the crystal is usually divided in thin layer of few nanometres to few hundreds nanometres. In each layer, a given fraction of defects is defined as input for simulation. Simulation can be then performed and the output is a channelling spectrum that contains information on the backscattering events at each acquisition channel. The final step is to normalize the obtained spectra for comparison with experimental data.

In a simulation, a backscattering energy spectra for He channelling in crystalline materials and/or an angular scan are usually obtained as the output. As the most important application of the RBS/C technique, this program also allows the calculation of the damage fraction and the distribution of defects versus depth in the crystal. In this situation, the program can take into account various classes of defects such as point defects, defect clusters, dislocations and even the polygonisation of the crystal.

McChasy uses the ZLB potential [99] in order to takes into account the electron screening on the ion-atom interaction [100]. An important feature is the option to take into account the substitutions of atoms in the structure. Such option becomes important when the crystal is heavily irradiated by ions to very high concentration. In this situation, the incorporation of foreign ions modifies to large extent the composition of the structure and thus influences the eventual results. Typically, one simulation that gives an acceptable statistic ($N_{tot} \simeq 40000$) takes 120 minutes.

Chapter 3

Irradiation effects on the urania structure

This chapter focuses on the experimental results obtained in this thesis. In the first part, channelling spectra recorded on the crystal implanted with the noble gas Xe is presented as an illustrative example of the used methodology. Then, the analysis of channelling spectra recorded on a crystal implanted with low-energy ion (applying the two-beam approximation approach) is explained and applied to the decomposition of channelling spectra. Afterwards, the distributions of defects versus depth and the evolution of the kinetics of damage build-up are extracted so as to understand the kinetics of the defects induced. Finally, similar experiments regarding the irradiations by lanthanide ions are presented in the second part.

3.1 Irradiation with noble gas ions

Figure 3-1 displays a typical example of channelling spectra recorded on a UO_2 single crystal recorded in aligned and random directions. Crystals were implanted with $470-keV$ Xe ions at both low fluence ($\Phi \leq 5\times10^{15}$ cm^{-2}) and high fluence ($\Phi \geq 5\times10^{15}$ cm^{-2}) ranges and alternatively characterised by RBS/C after each implantation step. The figure also displays the channelling spectrum recorded on the same sample before irradiation. Note that the random spectrum recorded consists of a front at 2887 keV (the signal due to the backscattering of He ions on U sub-lattice at the surface of crystal), a plateau below 2887 keV (the signal due to backscattering on U atoms at increasing depth) and a characteristic peak located at about 1045 keV (see figure 3-1.a). The appearance of this peak is the consequence of the elastic resonant scattering at 3038 keV of ^4He ions with ^{16}O atoms, $^{16}O(^4He,^4He)^{16}O$, which enhances the backscattering on O sub-lattice target. Actually, the Rutherford elastic backscattering of ^4He ions on O sub-lattice results in the backscattered signal with a front (that should appear at 1130 keV) and a continuous increasing signal as decreasing energy of backscattered ions. However, since the Rutherford backscattering cross section is proportional to the square of atomic number of target atoms, the backscattering signal coming back from O sub-lattice ($Z^2 = 8^2 = 64$) is so small compared to the backscattering signal coming back from U sub-lattice ($Z^2 =$

$92^2 = 8464$) that it becomes negligible and cannot be distinguished (or separated) from the overall spectra. Only backscattered ions coming back from the resonant scattering are visible from the channelling spectra as the resonant reaction enhances the backscattering event of ^4He on O sub-lattice to larger factor (typically 20, see section 2).

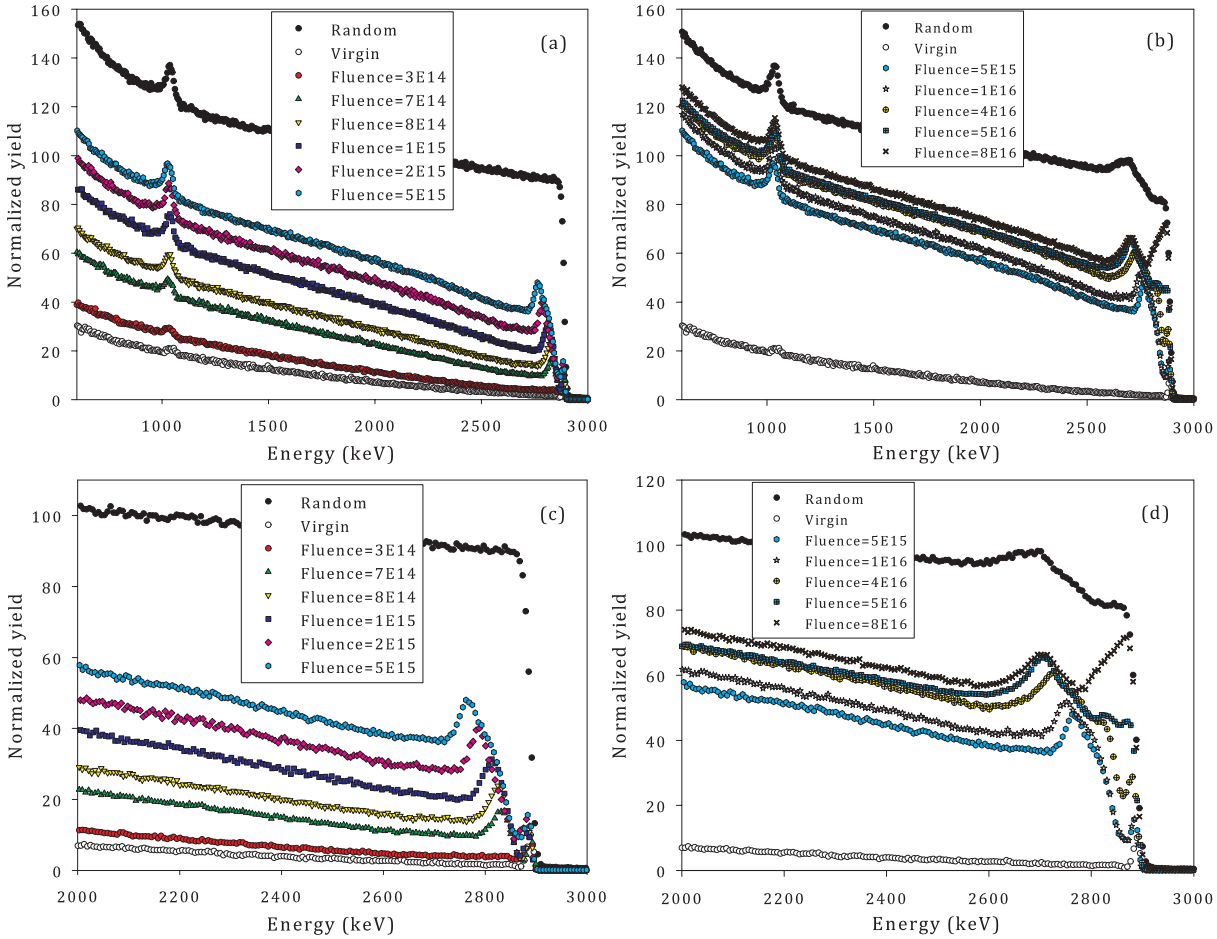

Figure 3-1: Typical (a and b) and high-energy part (c and d) of RBS/C spectra recorded in random (full circle) and $\langle 100 \rangle-$aligned directions (empty circle) on un-implanted and implanted UO_2 crystal with $470 - keV\ Xe$ ions. Fluences are measured in unit of cm^{-2}.

The RBS/C spectra recorded for virgin samples reveal a very low dechannelling level, in accordance with the good crystallinity of the single crystals ($\chi_{min} < 2\%$ at the surface). Axial channelling spectra recorded on irradiated crystals, in contrary, show an important increase of the minimum axial yield with respect to the virgin level. In other words, irradiation have had strong influence on the crystalline structure of the investigated crystal and hence highly increased the backscattering of He ions.

A peak at an energy ranging from ~ 2600 to 2887 keV (known as the "damage peak" in the literature) appears as a consequence of ion irradiation. This peak reflects, in fact, the direct backscattering of He ions on U atoms randomly displaced by irradiation with low-energy Xe ions (by elastic nuclear interaction in the present investigation) (figure 3-1.c and figure 3-1.d). It is worth emphasizing that the level and shape of the peak reflects

the local concentration and the depth distribution of U atoms displaced from their regular positions in the fluorite-type structure. One can notice that the damage peak extends to a deeper depth from the surface when the irradiation fluence increases but the axial yield recorded at a given energy (and hence at a given depth) remain almost constant, except at very high fluence.

The random spectrum recorded on a crystal implanted at high fluence has a shape that has been modified as a consequence of high impurity concentration. As it can be observed on figure 3-1.b, two specific features are clearly viewed. The first feature is seen at the close surface where the backscattering yield of the random spectrum exhibits a lower level for crystal implanted to high concentration compared to the un-irradiated crystal. The second feature lies in the observation of a peak located at the depth corresponding to the energy of backscattered ion of about 2680 keV corresponding to the backscattering energy of He ion on Xe (the front of the backscattering signal due to Xe - corresponding to Xe atoms located at the surface - locates at 2737 keV). Both the two features are not visible for low implanted fluence (see figure 3-1.a) as their effects are negligible but they are seen only when the crystal is heavily implanted. Therefore, they are definitely connected to the presence of impurities at high implanted concentration in UO_2 crystal.

An abnormal feature of channelling spectra is observed for crystals irradiated at very high ion fluence: a huge rising of the backscattering signal close to the surface can be observed from the spectra (see figure 3-1.d). The backscattering of He ions at the close surface increases dramatically in comparison to spectra recorded at low fluence. The signal approaches the random level as if the crystalline structure at the surface layer were destroyed, i.e., as if the crystal structure were amorphised by irradiation.

A clear effect of irradiation is also observed on the dechannelling signal of the spectra. At low ion fluence, the dechannelling signal recorded (from 2000 to 2600 keV, see figure 3-1.c) increases rapidly with increasing ion fluences. On the contrary, the dechannelling signals of spectra recorded for very high ion fluence behaves differently (figure 3-1.d), a similar continuous increasing signal is recorded with the decreasing energy of detected ions but the absolute level does not differ so much from fluence to the other. It is seemingly that the dechannelling signal for He ions literally saturates when the disorder in the UO_2 lattice increases (i.e. when the crystal is irradiated to large fluence).

To account for the effects of irradiation and to understand the effects of irradiation on the structural stability, a first analysis of channelling spectra has been first carried out in the framework of the classical two-beam approximation (TBA) method. This approach was proposed by Bøgh in 1968 [101]. It is assumed that the analysing beam consists of two components: the random component and the channelled component. The random component is supposed to interact with all atoms (matrix atoms and atoms

displaced from their regular positions), whilst the channelled component is supposed to interact only with atoms that are located within the channels. Backscattered ions of the channelled beam gives contribution to the damage peak and directly reflect the fraction of randomly displaced atoms in the matrix. The channelling spectrum is therefore composed of three components: the surface peak, the dechannelling signal and the damage peak. The surface peak represents the backscattering of He ions on atoms located at the surface of the crystal. For the sake of simplicity both the surface peak and the damage peak are fitted assuming a Gaussian-liked distribution. In addition, the dechannelling background is modelled by a Fermi-Dirac-shaped function [102].

An example of the decomposition of the channelling spectra recorded for a crystal implanted at the fluence of $\Phi = 1 \times 10^{15}\ cm^{-2}$ is depicted on figure 3-2. The decomposition of channelling spectra recorded for crystal implanted to high concentration is slightly different due to the extra contribution coming from implanted species and is explained later on. In general, in order to analyse a channelling spectrum using the TBA approach, one has to separate the damage peak from the channelling spectra. As a consequence, we obtain (i) a damage peak that reflects the local concentration of defects at given depth and (ii) a dechannelling signal that reflects the progressive increasing signal with increasing depth. The decisive point, which figures as the clue of this decomposition method, is the choice of shape of the dechannelling signal). In this work, the S-shaped background signal has been modelled assuming a Fermi-Dirac-like function that can be written by the following simple analytical expression:

$$F_{dech}(ch_i) = k - \frac{a}{1 + \exp\left(-\frac{ch_i - b}{c}\right)}$$

where ch_i corresponds to the channel number i used for recording the signal during the acquisition of a backscattering spectrum. The decomposition is made in channel (thus in energy) and then converted to the depth z. The parameters k, a, b, c are the characteristic parameters that define the height, the width and the position ... of the dechannelling signal.

For low implantation fluence, the procedure used to decompose a channelling spectrum is to fit the channelling spectrum by the sum of the three individual components: (i) the S-shaped signal which represents the dechannelled fraction of analysing beam, (ii) the surface peak which represent the fraction of analysing beam backscattered from atoms located at the surface of the crystal and (iii) the damage peak which represents the fraction of analysing beam backscattered from defective atoms that are randomly displaced within the matrix. When the best fit to the channelling spectrum is achieved, the Fermi-Dirac-liked dechannelling contribution is subtracted to get the fraction of defects

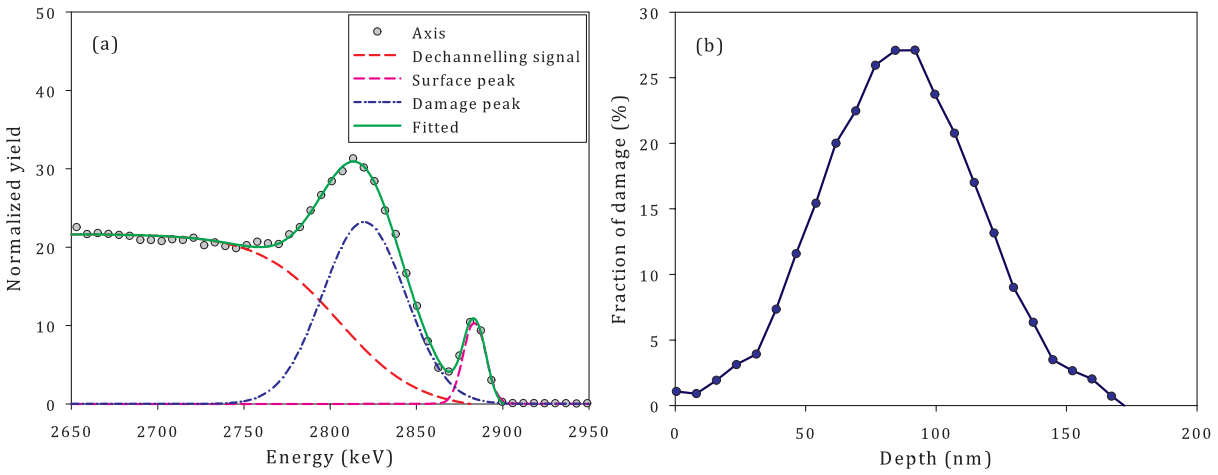

Figure 3-2: Typical example of a decomposition of channelling spectrum applying the TBA approach (a) and the corresponding distribution of defects versus depth (b). The channelling spectrum is fitted with three components: the dechannelling signal (red long-dashed), the Gaussian-shaped surface peak (pink short-dashed) and the Gaussian-shaped damage peak (blue dash-dotted).

F_d, which is calculated according to the following formula:

$$F_d = F_d(ch_i) = \frac{Y_{aligned}(ch_i) - Y_{surface.peak}(ch_i) - F_{dech}(ch_i)}{Y_{random}(ch_i) - F_{dech}(ch_i)}$$

in which: $Y_{aligned}(ch_i)$ and $Y_{random}(ch_i)$ are the normalized backscattering yields recorded in axial channelling condition (when the analysing beam is aligned along the crystal's orientation) and in random conditions respectively. $Y_{surface.peak}(ch_i)$ and $F_{dech}(ch_i)$ are the data obtain by the fit.

Finally, to extract the distribution of defect versus depth a transformation from energy into the depth is performed applying the tabulation of the stopping power measured for ^4He in UO_2 by using the data provided by the RUMP code.

For channelling spectrum recorded at high implanted fluence, the decomposition has to be modified since there is an extra contribution to the channelling spectrum due to the presence of impurities in the matrix (see figure 3-3). This phenomenon is observed *via* the appearance of a peak located at around 2680 keV on both aligned and random spectra (see figure 3-1.d). As it can be seen on this figure, the backscattering signal due to impurities overlaps on the damage peak. It is then necessary to isolate the backscattering signal on impurities so as to obtain the damage peak that reflects the pure contribution of the U sub-lattice. In this work, we performed that decomposition by supposing that the contribution of impurities to the axial channelling spectrum is equal to that contribution to the random spectrum. This approach assumes that all Xe atoms are located in random position similar to the case where impurities locate randomly within the matrix and give

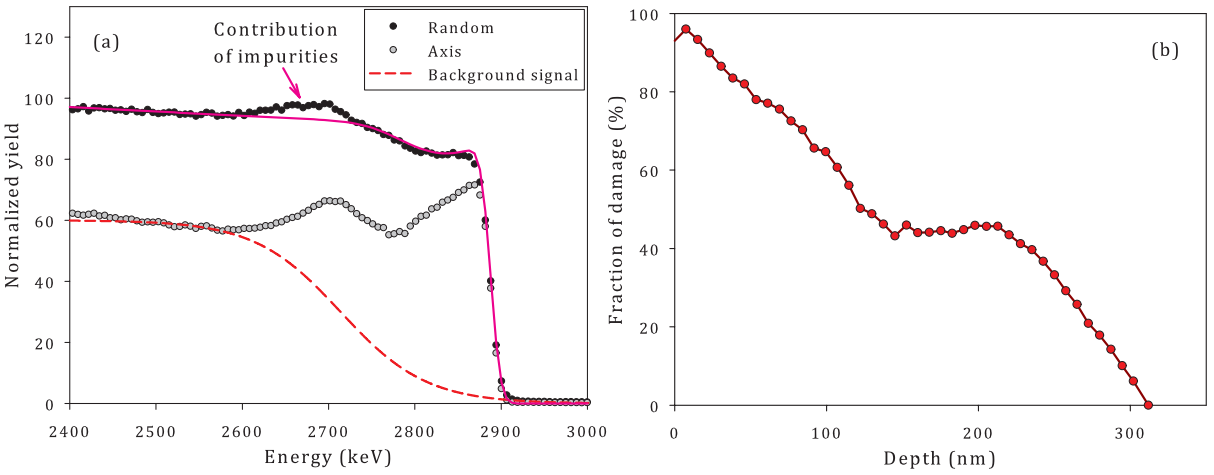

Figure 3-3: Decomposition of a channelling spectrum recorded at high implanted fluence taking into account the contribution of implanted impurities (indicated on figure a) and the corresponding distribution of defects versus depth (b).

contribution to the channelling spectra, as if spectrum was recorded in random condition. Finally, the eventual damage fraction at a given depth extracted from channelling spectra recorded for high implanted fluence is calculated taking into account the subtraction of contribution of impurities. The fraction of defects F_d is hence calculated using the following modified formula:

$$F_d = F_d(ch_i) = \frac{Y_{aligned}(ch_i) - Y_{surface.peak}(ch_i) - F_{dech}(ch_i) - Y_{impurity}(ch_i)}{Y_{random}(ch_i) - F_{dech}(ch_i) - Y_{impurity}(ch_i)}$$

where $Y_{impurity}(ch_i)$ is the normalized backscattering yield extracted from the random spectrum for impurities.

Figure 3-4 displays the distributions of damage fraction versus depth for various implantation fluences of Xe ions at low-fluence (figure 3-4.a), medium-fluence (figure 3-4.b) and high-fluence (figure 3-4.c) ranges. The distributions were extracted from the decomposition of signals according to the three components previously described. The distribution of Xe ions implanted to the matrix sub-lattice calculated by the SRIM code is also displayed so as to compare with the experimentally measured damage profiles. At low fluence (ranging from 0 to 1×10^{15} cm^{-2}) the radiation damage is created essentially around the implanted range of Xe in UO_2, i.e. around $Rp = 85$ nm. It is also apparent that the fraction of damage increases progressively with increasing ion fluence. At the medium fluence range (from 1×10^{15} to 1×10^{16} cm^{-2}), two important features are observed on the distribution of damage versus depth. Firstly, the radiation damage literally grows thicker. As the ion fluence increases, the damage created spreads into the deeper layer of the crystal up to 250 nm in depth, far beyond the calculated implantation profile. Secondly, the concentration of damage gradually extends deeper and saturates (at about

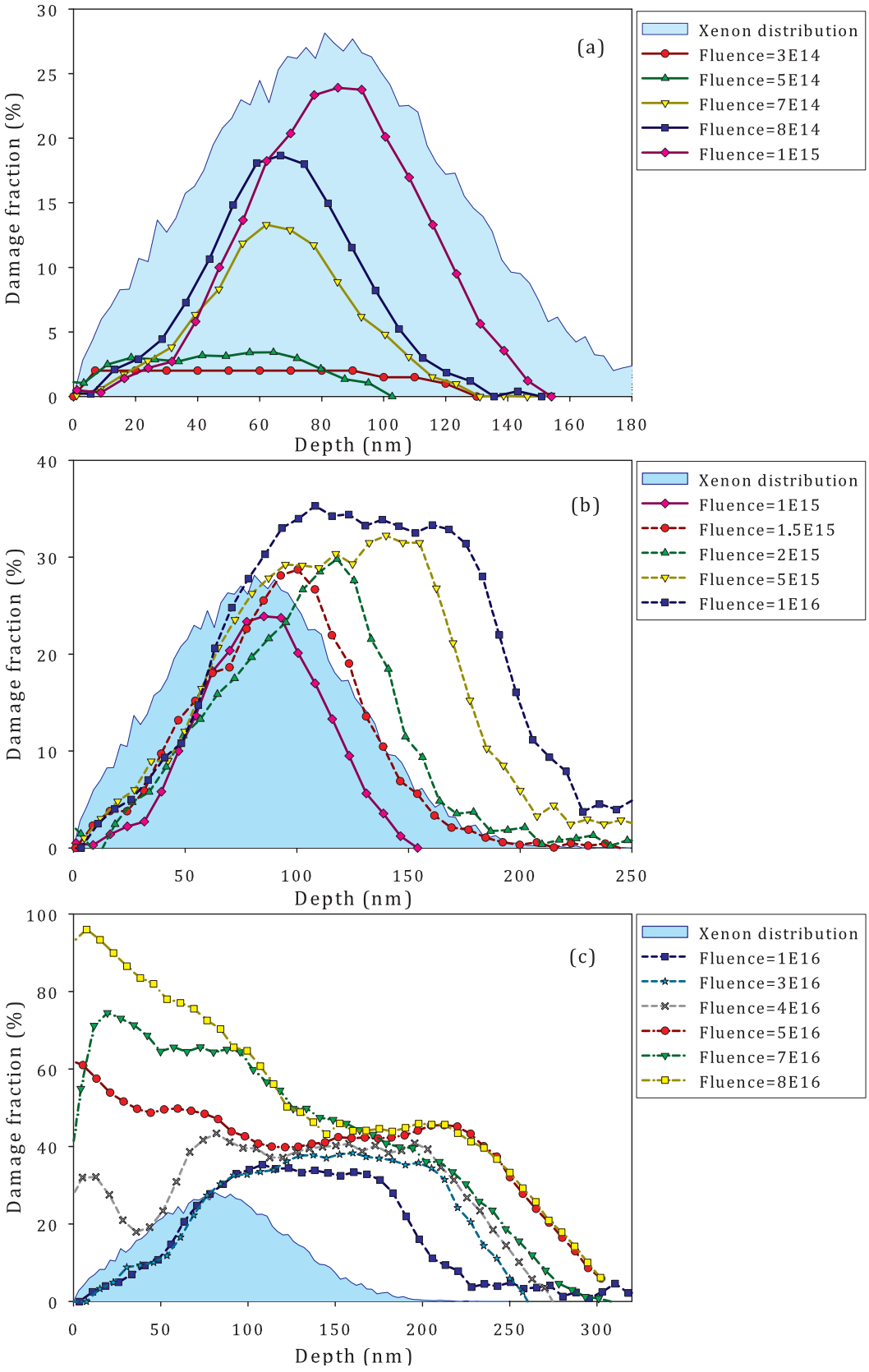

Figure 3-4: Distribution of randomly displaced atoms versus depth for (a) low, (b) medium and (c) high fluence ranges. Depth distribution were extracted from analysis of channelling spectra using the two-beam approximation method. Fluences are expressed in unit of cm^{-2}. Filled area represents the distribution of implanted Xe calculated by the SRIM calculation code (in arbitrary unit).

32 %) when the maximum depth of the created damage exceeds the maximum depth of Xe atoms calculated by SRIM code. At high fluence (over 1×10^{16} cm^{-2}), a marked behaviour of damage induced is observed. First of all, a maximum depth of about 300 nm was observed on the damage profiles for the highest investigated fluence. The distribution of defects induced at high ion fluence can be separated into two regions: the surface region and the bulk one. On the bulk region (the region which is located beyond the distribution of the implanted ion, larger than $Rp + \Delta Rp$, i.e. 150 nm), the fraction of defects created remains almost constant. On the contrary, a dramatic increase of the defects is observed from the projected range of Xe ions towards the free surface of the crystal ($0 \leq z \leq Rp$). At the highest ion fluence used in this investigation (8×10^{16} cm^{-2}), the fraction of defects almost reaches the random level, i.e., 100 % of atoms are randomly displaced from their regular positions.

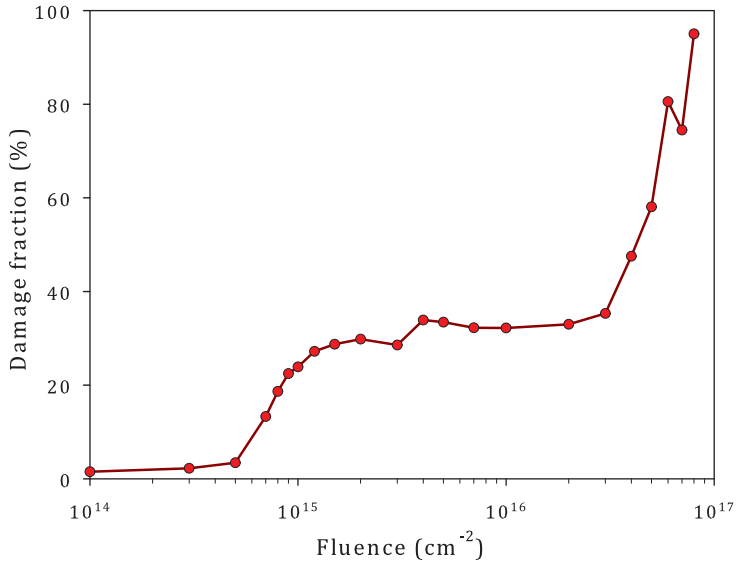

Figure 3-5: Evolution of the fraction of randomly displaced atoms calculated at the maximum of the profile damage accumulation in the UO_2 single crystal as a function of ion fluence.

The evolution of maximum damage level extracted from the depth profiles (calculated at the maximum of the distributions) is represented in figure 3-5 as a function of the implanted ion fluence. It is apparent from the data that under irradiation of Xe ions the damage accumulation in UO_2 single crystal follows two sharp steps interspaced with a saturation stage (a constant plateau is observed). The first build-up step ranges between about $\Phi = 7 \times 10^{14}$ cm^{-2} to 1×10^{15} cm^{-2}. The second build-up step occurs at high implanted ions fluences (larger than $\Phi = 3 \times 10^{16}$ cm^{-2}). Between the two sharp steps, the accumulation of damage remains essentially unchanged over a very wide range of implanted ion fluence (between $\Phi = 1 \times 10^{15}$ cm^{-2} and $\Phi = 3 \times 10^{16}$ cm^{-2}). At the highest implanted fluence (at $\Phi = 8 \times 10^{16}$ cm^{-2}), the created damage reaches almost 100 %. UO_2 crystalline structure behaves as if it were amorphised when irradiated by Xe ions

to this fluence.

3.2 Irradiation with lanthanide ions (La and Ce)

Two investigations using La and Ce ion accelerated at $500 - keV$ to bombard the UO_2 single crystals have been performed. Alternative implantation with lanthanide ions and characterisation were performed *in situ* on the IRMA/ARRAMIS facility. In comparison to the insoluble inert noble gas Xe, La and Ce are soluble into the UO_2 fluorite-type structure [103] while the masses of the three considered elements are very close. Figure 3-6 and figure 3-8 depict the channelling spectra recorded while the corresponding damage depth distributions generated by the implanted species are shown on figure 3-7 and figure 3-9, respectively. Channelling spectra recorded in both two conditions show a progressive rising of the dechannelling signal due to the radiation effects. In addition, the damage peaks are clearly visible and the broadening of the damage zone towards the deeper depth of crystal with increasing the ion fluence is clearly evidenced (similarly to the Xe irradiation case discussed in the previous section). The axial yields at the right side of damage peaks at a specified energy (close to the surface) remain also nearly constant. However, an important difference on shape of channelling spectra is observed at very high ion fluence: irradiation with La and Ce ions does not lead to the dramatic increase of the damage induced at the surface previously observed for the Xe case. This actually reveals that the UO_2 single crystals irradiated to high fluence by lanthanides elements behave differently compared to the crystal irradiated with Xe elements. In other words, the chemical nature of implanted species plays a role on the matrix destabilisation at high fluence.

The distributions of damage versus the depth reveal a similar behaviour of the damage induced by the two different ions. At low implanted fluence (below $\Phi = 1 \times 10^{15}$ cm^{-2}), the fraction of induced damage increases gradually with increasing ion fluence around the implanted range $Rp \sim 85$ nm. At higher implanted fluence (above 1×10^{15} cm^{-2}), the creation of defects extends into the deeper layer (well beyond $Rp + \Delta Rp =$ 125 nm). It is worth to notice that, in both the two studying cases, the creation of defects saturates when irradiating the crystals to higher fluence and, in addition, a similar level of maximum fraction of defect at the saturation (around 25 %) is observed. This level is lower than the one recorded for $Xe-$implanted crystal.

The evolutions of the damage accumulation (calculated at the maximum of the distributions) corresponding to the irradiation with Xe, La and Ce are presented on figure 3-10. The figure is plotted using two scales other than the implanted ion fluence scale, i.e. the number of *dpa* scale in order to compare the effect due to the radiation damage created by ballistic collisions and the concentration of implanted species scale, so as to compare the effects due to the incorporation of a given type impurity (soluble and insoluble - chemical

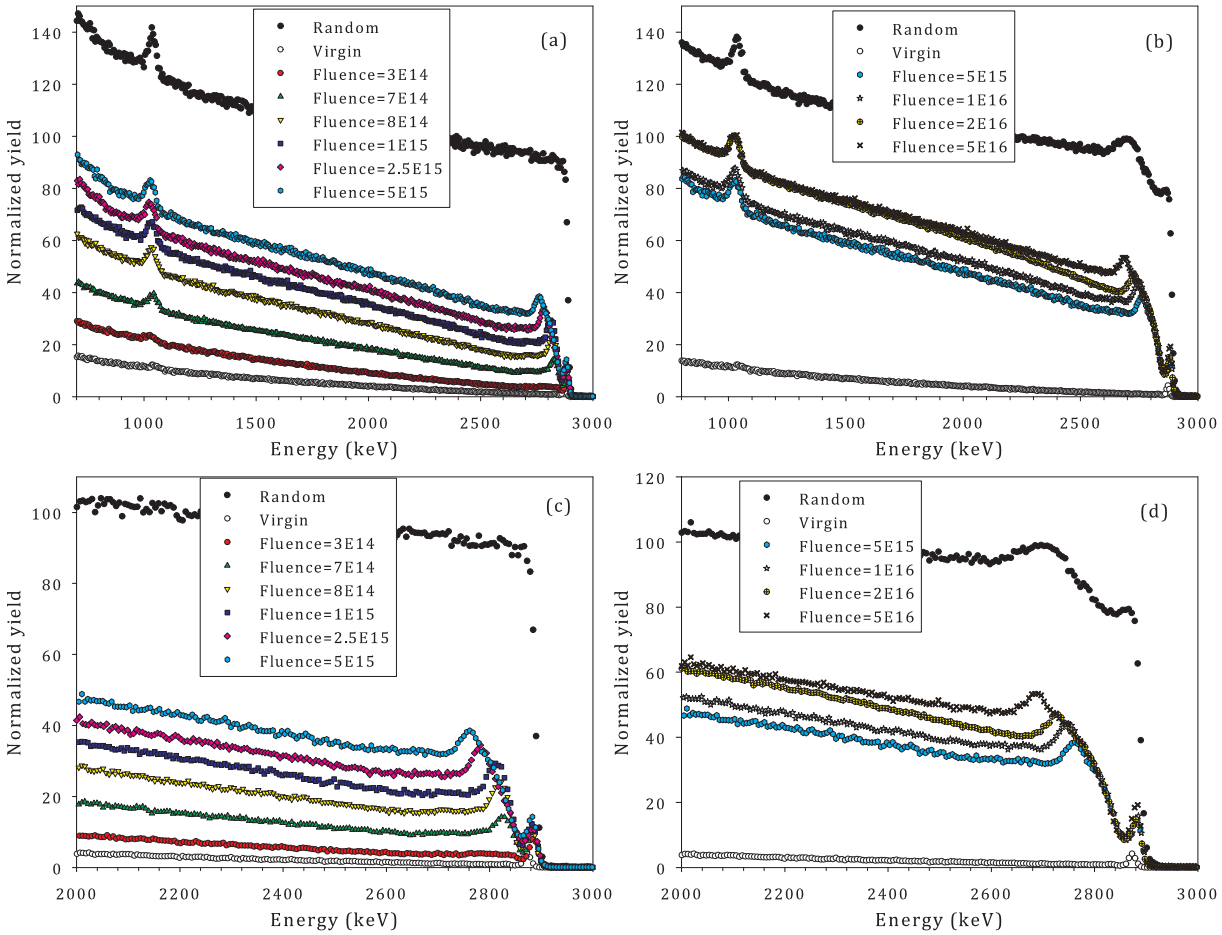

Figure 3-6: Channelling spectra (a and b) and high energy part of channelling spectra (c and d) recorded for UO_2 crystals irradiated with La ions. Fluences are measured in unit of cm^{-2}.

effect). Both the *dpa* and the concentration of implanted species scales are calculated from the fluence scale based on SRIM calculation. Calculations were performed assuming that the displacement thresholds of U and O atoms are $E_d(U) = 40\ eV$ and $E_d(O) = 20\ eV$ respectively [81]. The two following mathematical expressions are applied for converting from fluence to *dpa* and concentration scales.

$$dpa = D_{TRIM} \times 10^8 \frac{\Phi}{\left(\frac{N}{V}\right)_{UO_2}} \quad \text{and} \quad C = \frac{(N/V)_{ion}}{(N/V)_{UO_2}} \times 100\%$$

where D_{TRIM} is the maximum collision events calculated by the SRIM code expressed in $atoms/cm^3/atoms/cm^2$; $(N/V)_{UO_2}$ is the theoretical density of UO_2; $(N/V)_{ion}$ is the maximum density of ion calculated by SRIM expressed in $atoms/cm^3$ and Φ is the actual ion fluence (in expressed in cm^{-2}).

Figure 3-10 shows a fast rising of damage induced is observed in all three cases at low fluence. In other words, all the evolutions present a build-up step that is induced around 4 to 7 *dpa* corresponding to a minor fraction of incorporated ions of about 0.1

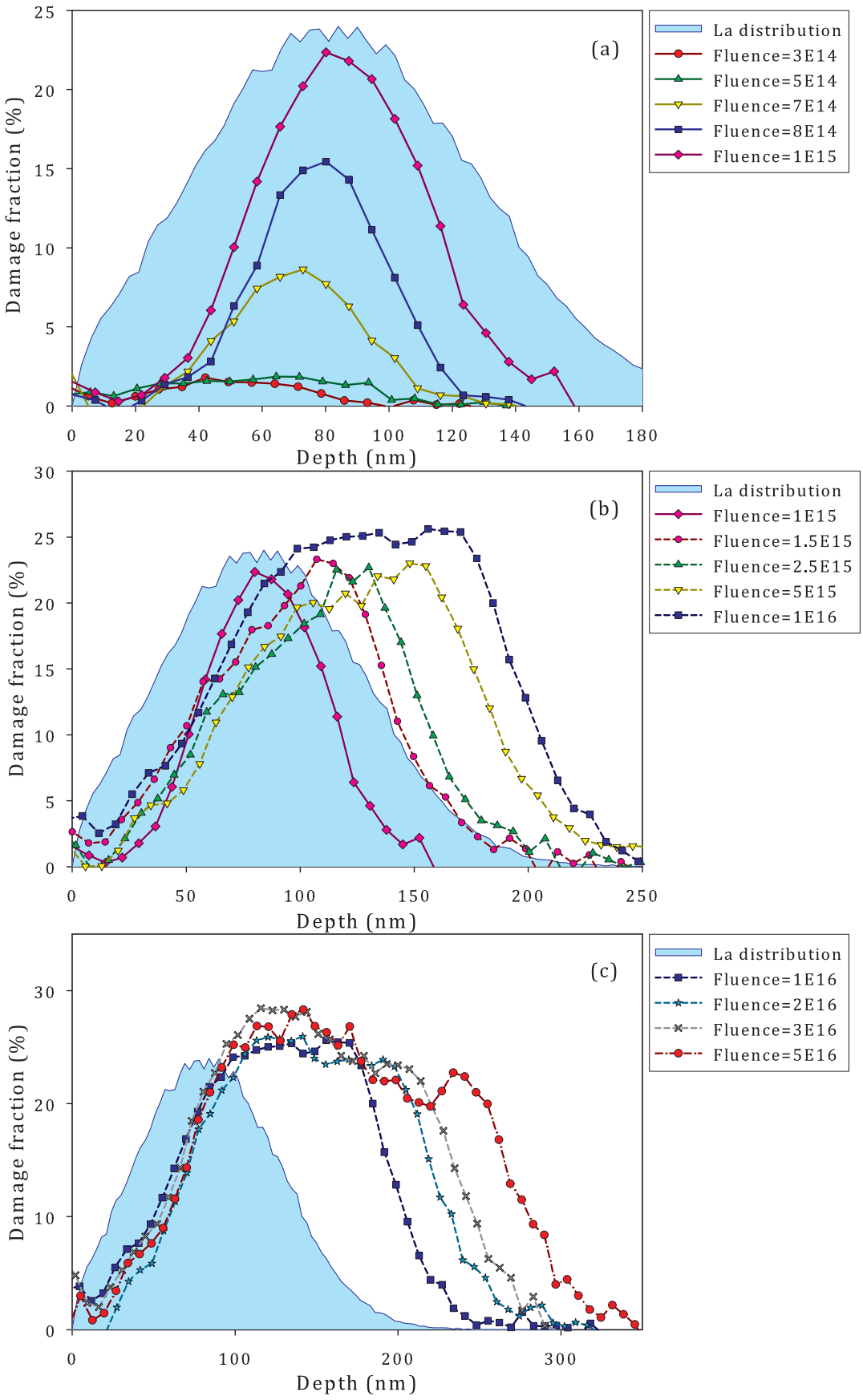

Figure 3-7: Distributions of the defects versus the depth extracted (using the same TBA method discussed here before) for UO_2 crystals implanted with *La* ions. Fluences are expressed in unit of cm^{-2}. The distribution of *La* (filled area) calculated by SRIM program is plotted in arbitrary unit.

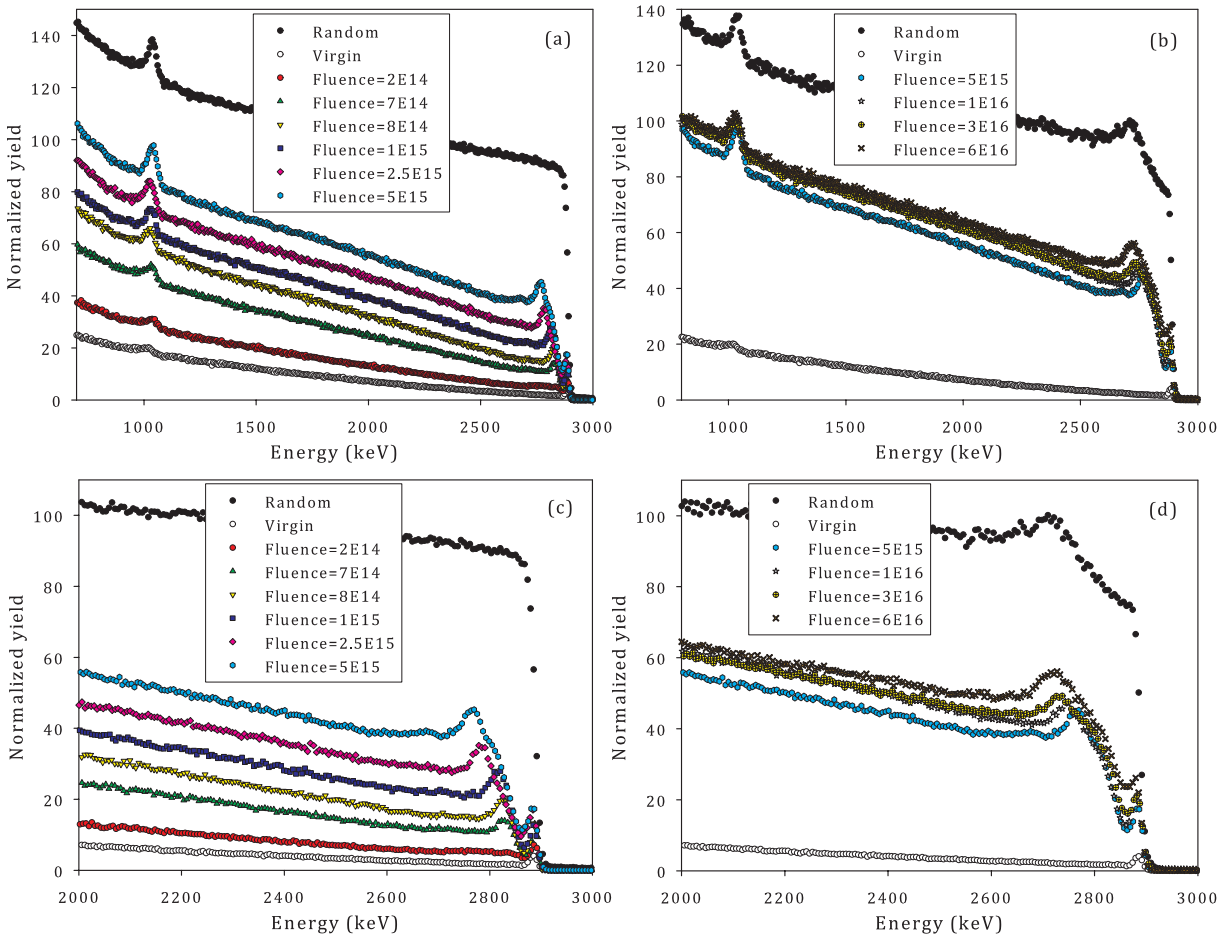

Figure 3-8: Channelling spectra (a and b) and high energy part of channelling spectra (c and d) recorded for UO_2 crystals irradiated with Ce ions. Fluences are measured in unit of cm^{-2}.

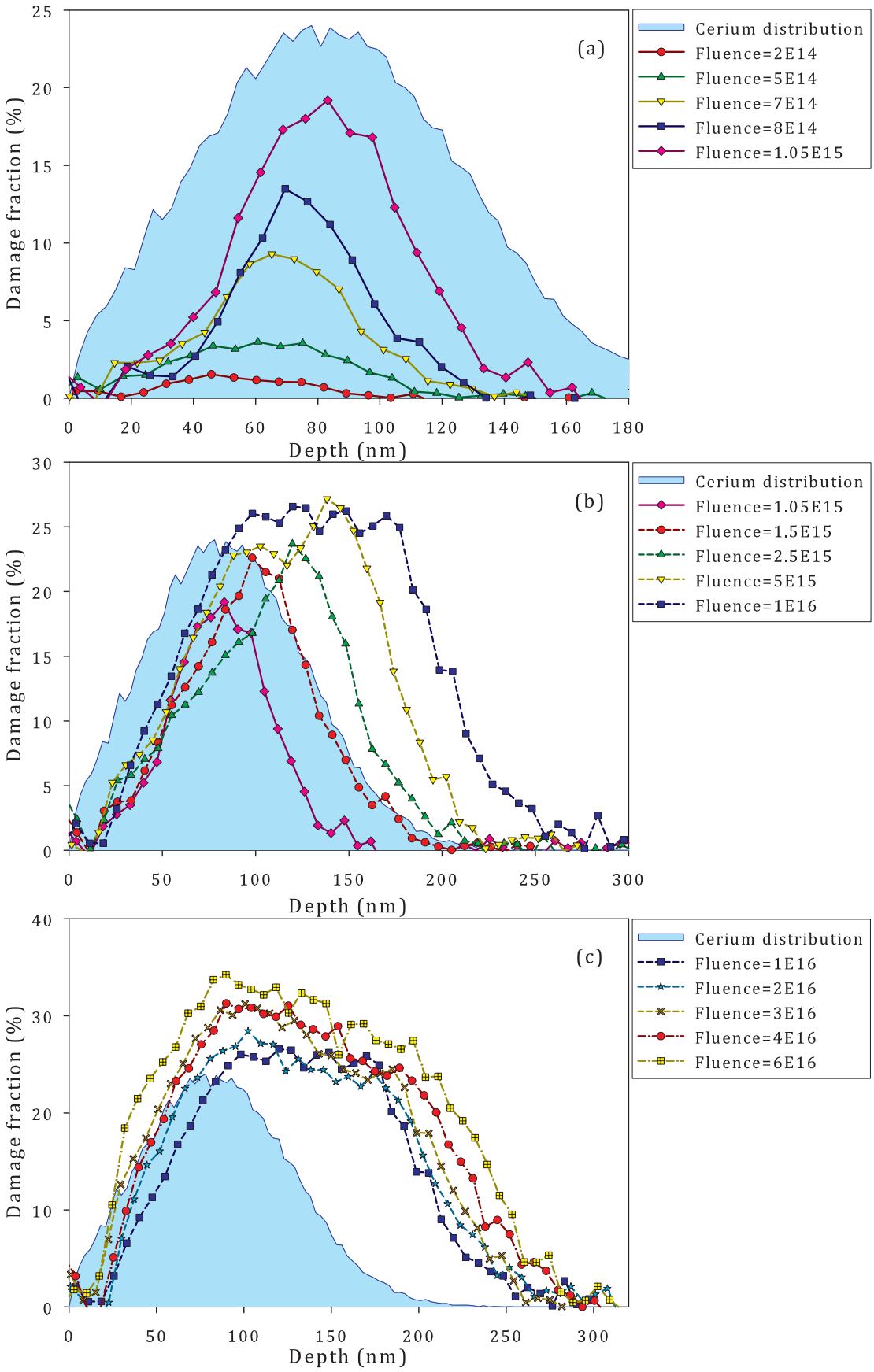

Figure 3-9: Distributions of the defects versus the depth extracted (using the same TBA method discussed here before) for UO_2 crystals implanted with Ce ions. Fluences are expressed in unit of cm^{-2}. The distribution of Ce (filled area) calculated by SRIM program is plotted in arbitrary unit.

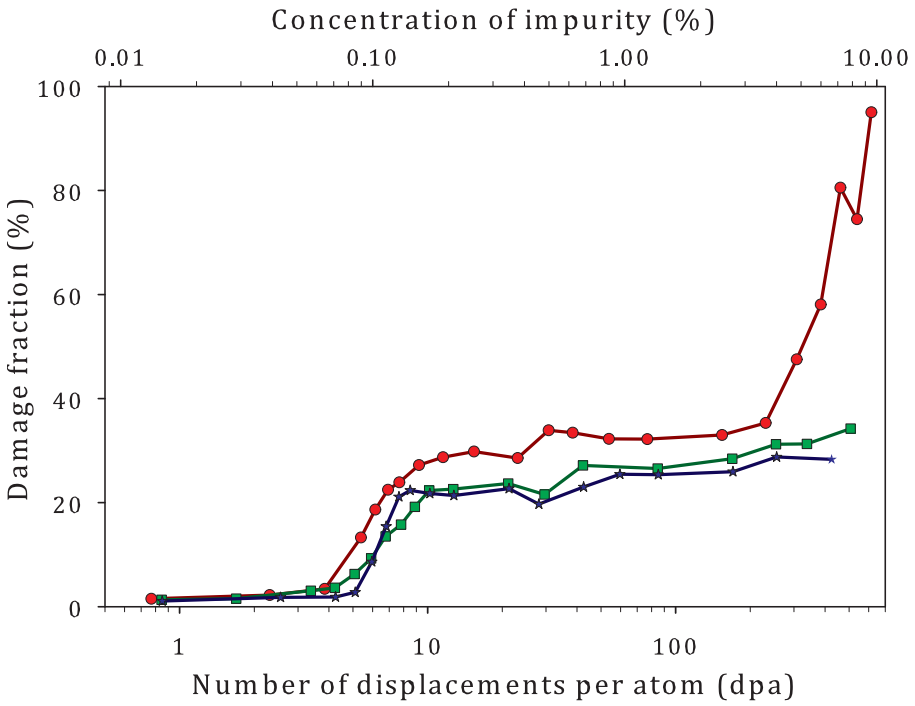

Figure 3-10: Evolution of the damage accumulation (fraction of randomly displaced atoms at maximum) in crystals implanted with $470-keV\ Xe$ (red circle), $500-keV\ La$ (blue star) and $500-keV\ Ce$ (green square) as a function of the number of *dpa* as well as a function of the maximum concentration of implanted species.

at. %. Moreover this build-up of damage is created for the same number of *dpa* and is therefore independent of the nature of the bombarding ion. Even though the mass and the energy chosen are different (for the sake of having the similar implanted range as discussed in previous session), one can conclude that this build-up step that appears at the same position regardless of the nature of ions originates from the same radiation-induced effects, due to the collision cascades generated by nuclear interaction.

Beside the same build-up step observed, the evolutions of the damage accumulation reveal important differences due to the effects of implantation with Xe compared to the effects of implantation with lanthanide ions. The first difference lies in the saturation plateaus. Distinct levels of saturation are clearly evidenced. The plateaus of saturation are almost the same for La and Ce but Xe ions results in a higher plateau of saturation. A significant difference of 10 % of absolute damage fractions induced is obtained from the data analysis (corresponding to a 30 % relative difference in the damage fraction). Secondly, the major difference is characterised by the lack of the second build-up step at very high concentration. A huge fraction of damage was created by the incorporation of Xe ions when its concentration exceeds 4 at. %, but such a dramatic increase is not evidenced for irradiation with La and Ce ions.

3.3 Microstructural evolution under irradiation

The X-ray diffraction technique has been applied to study the microstructural evolution and the elastic deformation of the UO_2 crystals due to irradiation with $500-keV$ Ce ions at low fluence to investigate the first step of the radiation damage, previously observed by RBS/C. In this investigation, the $\theta - 2\theta$ scans around peak index (400) for the $\langle 100 \rangle-$oriented crystals were recorded while the same data were recorded around peak index (222) for the $\langle 111 \rangle-$oriented crystals.

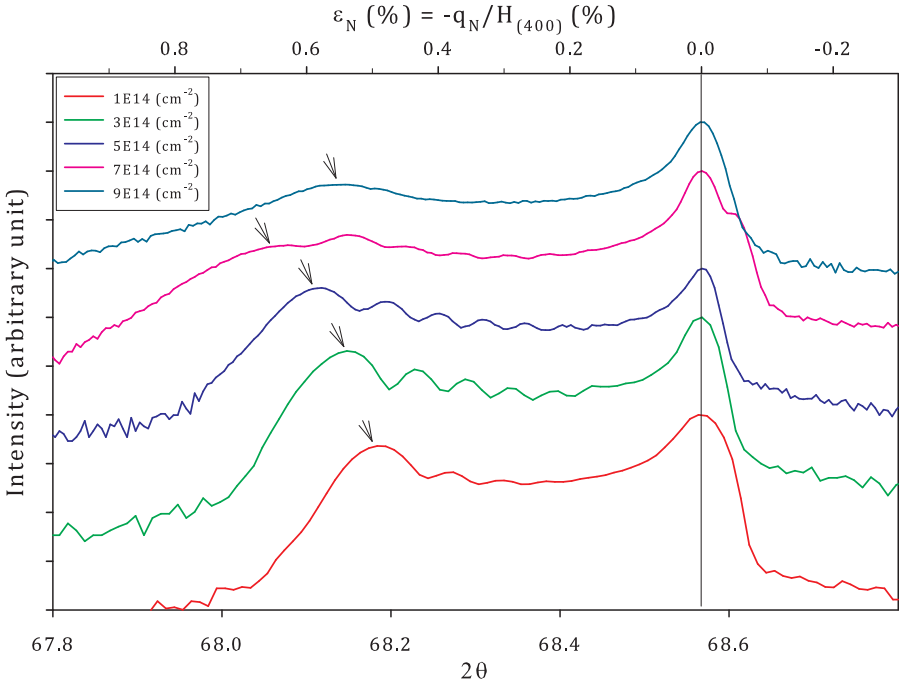

Figure 3-11: $\theta - 2\theta$ experimental scan recorded around the (400) Bragg reflection for $\langle 100 \rangle-$oriented UO_2 crystals implanted to indicated fluences. The arrows indicate the last peak arising from the maximum strain value exhibited by the damaged layer.

Figure 3-11 represents the $\theta - 2\theta$ experimental scans recorded around the (400) Bragg reflection for $\langle 100 \rangle-$oriented crystals. The intensity is plotted in logarithmic scale in arbitrary unit as a function of 2θ as well as a function of the normalized deviation from the reciprocal lattice vector ($\varepsilon_N = -q_N/H_{400}$). This quantity directly reflects the out-of-plane elastic strain of the crystal (i.e. the relative variation of the interplanar distance between (400) planes in the direction perpendicular to the crystal's surface). All recorded spectra present an intense peak located at $2\theta = 68.567°$ which is the consequence of the diffraction by the bulk part of the crystal, i.e. the underlying un-damaged substrate. This peak was recorded because X-rays allow probing the crystals structure up to the depth of about 5 μm from the surface while the irradiated part is present at the close surface up to the maximum depth of about 300 nm, as observed by RBS/C measurements (see figure 3-4, 3-7 and 3-9). This peak can be named, therefore, as the un-damaged peak.

The spectra presented on this figure are very similar for fluence from $\Phi = 1 \times 10^{14}$ to 7×10^{14} cm^{-2}. That is to say, these spectra display three similar important features: (i) the signal is composed of fringe pattern; (ii) the signal arising from the damaged part is located on the lower 2θ angles with respect to the un-damaged peak. According to the Bragg condition, this feature demonstrates that the damage layer is characterised by a larger lattice parameter and thus it exhibits a positive normal strain; (iii) The position of the last peak observed at the lowest 2θ angle (which is indicated by the small arrows on figure 3-11) shifts towards the lower angle when the ion fluence increases. This shift reveals an increase of the maximum normal strain ε_N^{max} up to the fluence of $\Phi = 7 \times 10^{14}$ cm^{-2}. For the crystal implanted at 9×10^{14} cm^{-2}, the fringe pattern vanishes. The $\theta - 2\theta$ scan recorded at this fluence presents an intense peak due to the substrate along with a very wide peak due to the damaged part. This wide peak is attributed to the diffuse scattering arising from a highly defective crystal [104, 105]. It is worth noticing that at this fluence, this peak moves towards the un-damaged peak, a phenomenon that reveals the strain relief in the damaged layer. Such phenomenon has been well reported for UO_2 single crystal irradiated with $20 - keV$ He ion [106] and also for other crystalline structures as in cubic zirconia [107] and pyrochlores [108].

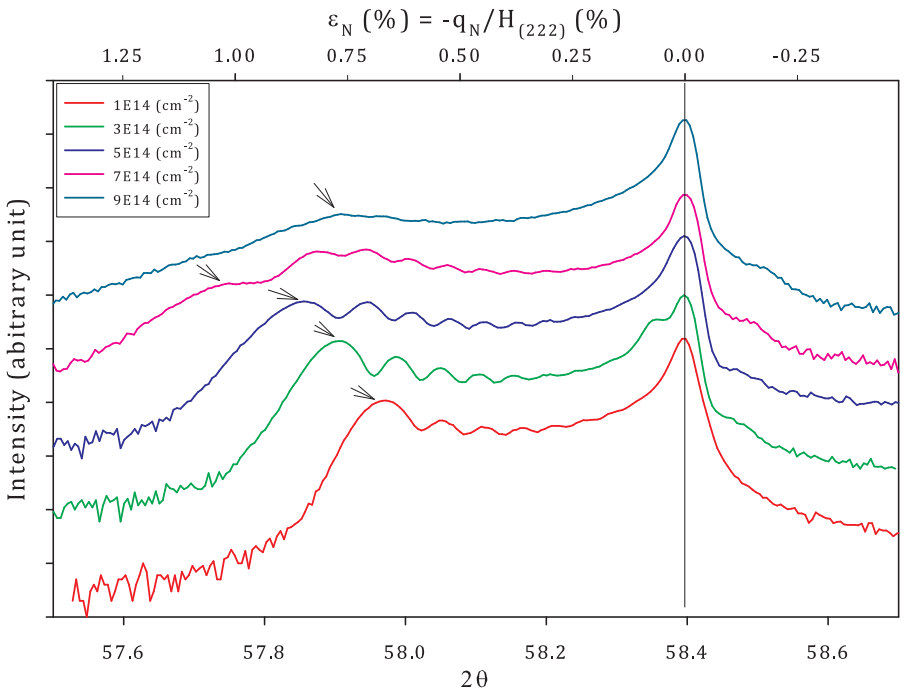

Figure 3-12: $\theta - 2\theta$ experimental scan around the (222) atomic planes for $\langle 111 \rangle-$oriented UO_2 crystals implanted to indicated fluences. The arrows indicate the last peak arising from the maximum strain value exhibited by the damaged layer.

Figure 3-12 displays the $\theta - 2\theta$ experimental scans around the (222) Bragg reflection for $\langle 111 \rangle-$oriented crystals. Similar features are observed as compared to the same scans obtained on $\langle 100 \rangle-$oriented crystals. The peak located at $2\theta = 58.395°$ corresponds to

the diffraction from the substrate part. For all crystals implanted up to $\Phi = 7 \times 10^{14}$ cm^{-2}, the corresponding spectra clearly show the fringe patterns on the lower 2θ angles. While increasing ion fluence, the last peak located on the lower 2θ angle shifts towards smaller values of 2θ; this feature is related to the increase of the maximum normal strain due to irradiation. At the fluence of $\Phi = 9 \times 10^{14}$ cm^{-2}, the fringe pattern disappears. The spectrum reveals the consequence of diffuse scattering by the defective part which is observed *via* the wide peak located on lower 2θ angles side as the perfect atomic arrangements is severely perturbed. In addition, this wide peak is also observed to move towards the higher 2θ angle, indicating a partial relief of the normal strain.

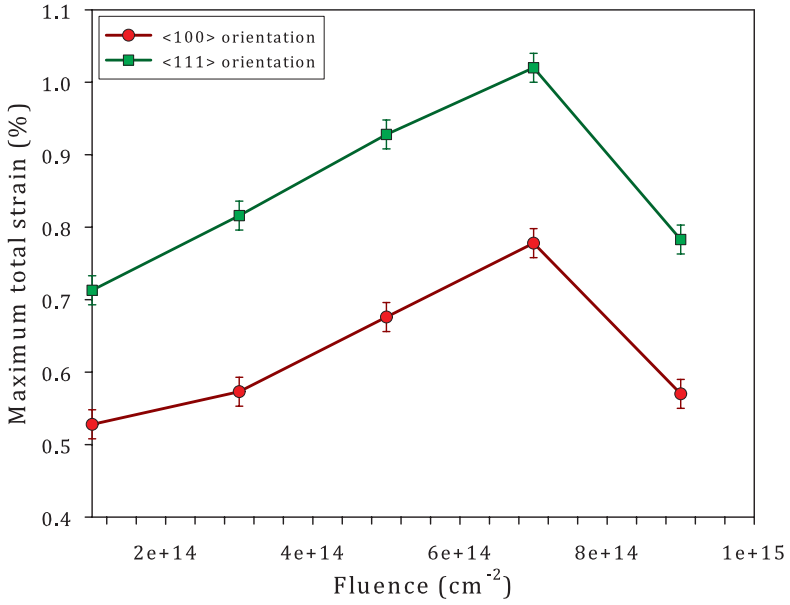

Figure 3-13: Evolution of the maximum total strain as a function of implantion fluence for $\langle 100 \rangle-$ and $\langle 111 \rangle-$oriented crystals.

Figure 3-13 depicts the evolution of the maximum normal strain ε_N^{max} arising in the damage part as a function of the ion fluence for both $\langle 100 \rangle$ and $\langle 111 \rangle$ orientations. The value of maximum normal strain is obtained directly from the position of the last peak located on the lowest angle on the $\theta - 2\theta$ scans with respect to the un-damaged peak: $(\varepsilon_N^{max} = \frac{\Delta d}{d_{hkl}} = -\frac{q_N}{H_N} = -\frac{q_N}{H \cos\psi})$ where Δd represents the variation of the inter-planar spacing induced by irradiation; $-\frac{q_N}{H_N}$ represents the normalized deviation expressed in the reciprocal space.As clearly shown on this figure, the maximum normal strain experimentally measured depends on the orientation of the investigated crystals. The values observed for $\langle 111 \rangle-$oriented crystals are higher than those for $\langle 100 \rangle-$oriented crystals. Regarding the evolution with irradiation, the maximum normal strain in both orientations increases with increasing ion fluence up to 7×10^{14} cm^{-2}, corresponding to 5.9 *dpa*. Maximum values of 0.65 % and 1.02 % are observed when the irradiation reaches the fluence of 7×10^{14} cm^{-2} for both $\langle 100 \rangle-$ and $\langle 111 \rangle-$oriented families, respectively. When

the fluence exceeds 7×10^{14} cm^{-2} the maximum normal strain in both families drops down. This phenomenon reveals a partial relief of the strain in the crystal [105]. At this stage, there exists a transition from elastic to plastic deformation in the crystal. It is likely that at the first step the irradiation creates point defects leading to the increase of lattice parameter of the irradiated part. When the relaxation of the crystal takes place, the deposited energy leads to the creation of extended defect clusters in the matrix. These phenomena, i.e. the relief of strain field and the formation of defects clusters, are observed in connection to the steep increase of RDA observed by the RBS/C measurement at 4 to 7 *dpa* (see figure 3-10). The steep increase of RDA is concomitant to the relief of the strain field under continuous irradiation.

The $\theta - 2\theta$ scans recorded at each fluence step can allow one to determine the maximum out-of-plane strain. Based on the maximum normal strain, the corresponding strain/stress state of the damage layer can be derived. The following analysis of the strain/stress state, which is based on a two-step model [109, 110], holds for single crystal of cubic crystalline structure submited to irradiation with low energy ion.

The analysis of the strain/stress state can be made assuming that: (i) only the irradiated layer responds to the mechanical solicitation and this response is merely elastic; (ii) the in-plane strain does not exist, there is only an out-of-plane strain and (iii) the swelling of the damaged layer is free in the out-of-plane direction due to the free surface. The two-step evolution of the strain/stress state occurs as the following. In the first step, the thin layer that is submitted to the mechanical solicitation (i.e ion irradiation) can be considered as a free thin film inside which the radiation induced defects lead to the free swelling or shrinking of the surrounding matrix and thus to the local volume modification:

$$\left(\frac{\Delta V}{V}\right)^{def} = 2\varepsilon_{//}^{def} + \varepsilon_{N}^{def}$$

where $\varepsilon_{//}^{def}$ and ε_{N}^{def} denote the in-plane and out-of-plane strains due to defects, respectively. Supposing that the lattice modification is isotropic, $\varepsilon_{//}^{def}$ is equal to ε_{N}^{def} and therefore

$$\left(\frac{\Delta V}{V}\right)^{def} = 3\varepsilon_{N}^{def}$$

In the second step, since the damage layer can be considered as the thin film deposited on a substrate (the thick un-damage layer), it is constrained by the substrate and hence there exists a stress imposed by the substrate to the damaged layer in the direction parallel to the crystal's surface (i.e. the in-plane direction). As a result, the substrate exerts a fixation stress ($\sigma_{//}^{SR}$, SR denotes the reaction of the substrate) which finally cancels the two in-plane strain components appearing in the damage layer as a consequence of

the radiation damage ($\varepsilon_{//}^{SR} = -\varepsilon_{//}^{def}$). The applied fixation stress consequently leads to an additional normal strain acting on the damaged layer and the deformation takes places only in the out-of-plane direction, i.e., the deformation evolves along the free surface of the crystal where there is no stress imposed. This additional strain due to the reaction of the substrate is proportional to the initial elastic strain induced by irradiation:

$$\varepsilon_{//}^{SR} = \alpha_{hkl}^{SR} \varepsilon_N^{def}$$

where α_{hkl}^{SR}, which depends on the orientation and the elastic constants of the material, reflects the reaction of the substrate acting on the damage layer. This factor has been presented in the work of S.I. Rao and C.R. Houska [109]:

$$\alpha_{hkl}^{SR} = \frac{2C_{12} - C_{an}\Omega_{hkl}}{C_{11} + C_{an}\Omega_{hkl}}$$

In this expression, Ω_{hkl} is a geometric factor which is equal to 0 for $\langle 100 \rangle$ orientation and to 4/3 for $\langle 111 \rangle$ orientation; $C_{an} = C_{44} - (C_{11} - C_{12})/2$ with C_{ij} being the elastic stiffnesses of the investigated material. The values used in this investigation were experimentally obtained [111]: $C_{11} = 396\ GPa$, $C_{12} = 121\ GPa$ and $C_{44} = 64\ GPa$. Thus, the total normal strain experimentally measured *via* the $(\theta - 2\theta)$ scan can be expressed as the following [110, 109, 112]:

$$\varepsilon_N^{total} = \varepsilon_N^{def} \left(1 + \alpha_{hkl}^{SR}\right)$$

In summary, the irradiated layer is characterized by a zero in-plane strain and a non-zero out-of-plain strain which is normal to the crystal's surface.

Considering the stress exerting on the damage layer, this layer exhibits only the in-plane fixation stress since the third component is zero due to the free surface. As mentioned above, the in-plane strain of the damage layer is totally cancelled by the substrate; the fixation stress can be, therefore, calculated according to the work of Rao and Houska developed for cubic single crystal [109]:

$$\sigma_{//}^{fix} = -\frac{C_{11} + (1 - \alpha_{hkl}^{SR})C_{12} - C_{an}\left(1 + \alpha_{hkl}^{SR}\right)\Omega_1}{1 + \alpha_{hkl}^{SR}} \varepsilon_N^{total}$$

where Ω_1 equals 0 for $\langle 100 \rangle$ orientation and -2/3 for $\langle 111 \rangle$ orientation.

Figure 3-14 depicts the evolution of the maximum elastic normal strain induced by irradiation and the maximum in-plane fixation stress due to the substrate reaction arising in both the $\langle 100 \rangle-$ and $\langle 111 \rangle-$oriented crystals as a function of the implantation dose (expressed in *dpa*). The evolutions of the damage fraction measured by RBS/C are also represented. As it can be seen, the maximum elastic normal strain ε_N^{def} due to defects

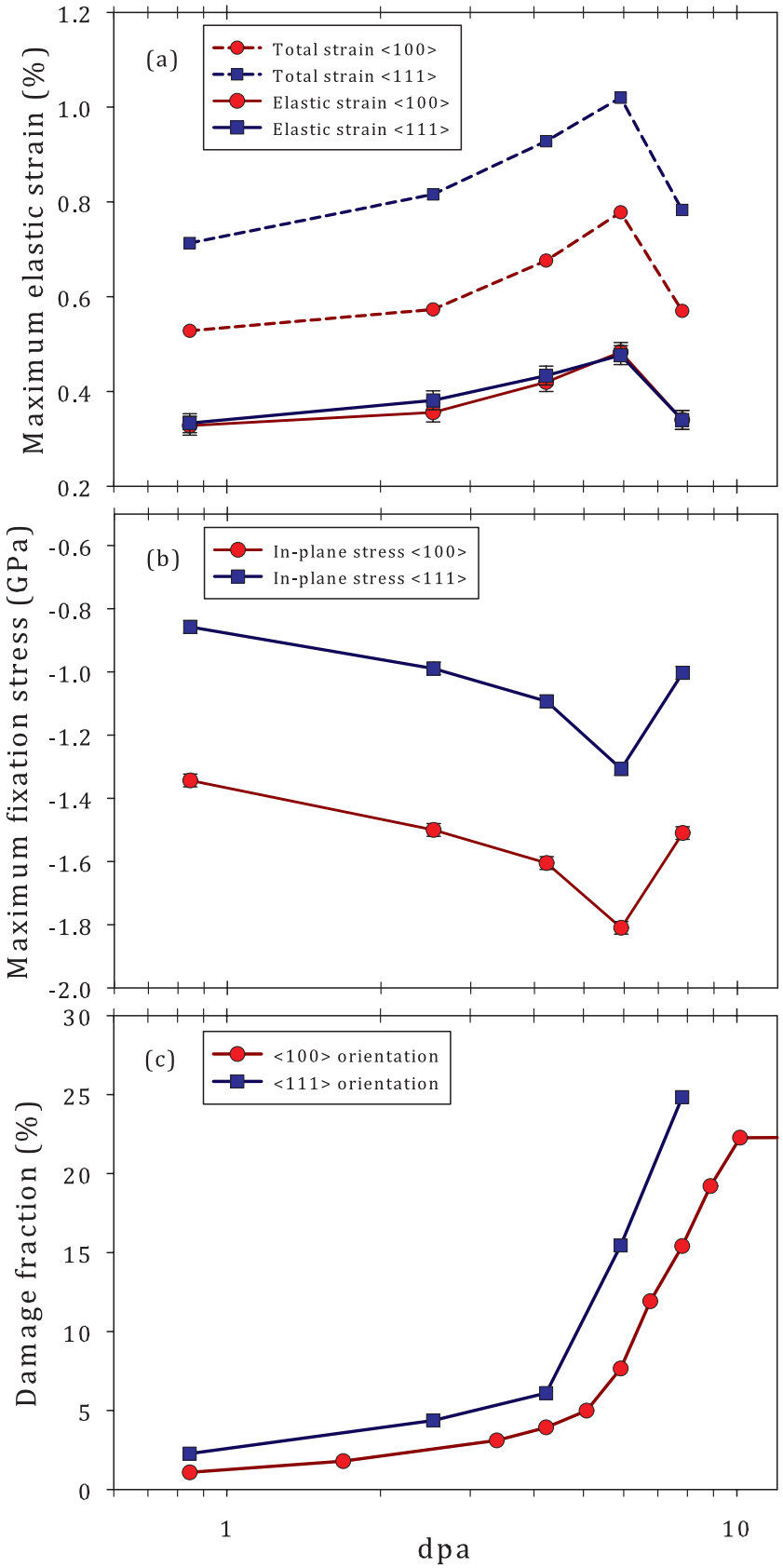

Figure 3-14: Evolution of the maximum elastic normal strain (a) and the maximum in-plane fixation stress (b) as a function of implantation dose expressed in *dpa* for both $\langle 100 \rangle-$ and $\langle 111 \rangle-$oriented UO_2 crystals implanted with Ce ions. The evolutions of damage fraction measured by RBS/C technique are also plotted (c).

only increases gradually with irradiation and reaches the maximum value of 0.4 % and 0.48 % at the implantation dose equivalent to 5.9 *dpa* for ⟨100⟩ and ⟨111⟩ orientations, respectively (figure 3-14.a). The values seen here clearly show that the sole contribution of radiation effects results in smaller normal strain compared to the total normal strain ($\varepsilon_N^{total} = 0.66\%$ and 1.03 % respectively for ⟨100⟩ and ⟨111⟩ orientations) to which there is an additional contribution due to the substrate's reaction. After this fluence, it is no longer possible to measure the elastic normal strain since the relaxation of the crystalline structure takes place. There exists a structural transformation from elastic to plastic deformation.

Similar behaviour of maximum in-plane stress is witnessed as compared to the evolution of maximum elastic normal strain. Negative values of maximum in-plane stress are obtained since this stress represents the compressive force acting on the damage layer by the substrate part. As shown on figure 3-14.b, this stress increases up to -1.8 and -1.3 GPa for ⟨100⟩ and ⟨111⟩ orientations; a very high value of stress arising in UO_2 crystal. However, the maximum values of fixation stress observed in this work are lower than those reported in a recent work where UO_2 single crystal implanted with $20 - keV$ He ions exhibited stress level of -2.8 GPa [106]. The difference is believed to be due to the solubility and concentration of implanted species. Indeed, the maximum relaxation stress is measured in the crystal implanted with $20-keV$ He ions at almost 5 at. % of implanted He, while the stress measured in this work is at less than 0.1 at. % of implanted Ce. In addition, He - an inert noble gas - is well known to form bubbles leading to the high strain in the damage layer ($\varepsilon_N^{def} = 1.03\%$), thus higher substrate reaction stress.

Referring to the evolution of damage build-up measured by RBS/C technique (see sections 3.1 and 3.2), both evolution of maximum elastic normal strain and maximum in-plane stress are observed since the very first stage of damage evolution when irradiation creates a the small fraction of defects. At this stage, the main type of induced defect is essentially point defects (interstitial defects). As irradiation reaches over 5.9 *dpa* (the same *dpa* at which the steep increase of radiation damage starts), a transformation of point defects to extended defects takes place. It is at this point we observed the relaxation of the crystalline structure, i.e. the transition from elastic to plastic deformation.

Comparing the two orientations, it is apparent that the elastic strain exhibited by the damaged layer shows no difference (see figure 3-14.a) while the total normal strains experimentally measured depend on the orientations. Such value measured for ⟨111⟩ orientations is clearly higher than ⟨100⟩ orientations. However, the measured total normal strain is higher for ⟨111⟩ than ⟨100⟩ orientations because of the elastic anisotropy of UO_2. This quantity is negative for UO_2 ($C_{an} = C_{44} - (C_{11} - C_{12})/2 = -73.5\ GPa$) meaning that the (111) planes are more compliant than the (100) planes. Therefore, they allow

a larger strain to be developed at the same irradiation condition. Similarly, the in-plane axial stress experienced by the damaged layers differs for the two orientations. Maximum values derived from the strain/stress analysis are -1.8 and -1.3 GPa for ⟨100⟩ and ⟨111⟩ orientations, respectively. The results obtained in this investigation is therefore totally in agreement to the recently reported work [112] where the elastic strain arising in ⟨100⟩ and ⟨111⟩ orientations is almost perfectly equal in irradiated cubic zirconia.

The same strain level exhibited by both crystallographic orientations can be explained by following argumentations. Firstly, the irradiation induced defects are isotropically distributed within the crystal. This argument is in consistency with the fact that the process of defects creation occurring during a collision cascades is random. Secondly, the damage fraction produced at given fluence seems to be equal regardless of the orientation. Indeed, the figure 3-14.c displays the kinetics of maximum damage fraction measured by RBS/C versus implantation fluence where the damage fraction is in both ⟨111⟩ and ⟨100⟩ orientations. This phenomenon is due to the same amount of energy deposited during a collision cascade. The eventual total normal strain experimentally measured is different because the reaction of the thick substrate layer is different. This reaction is dependent to the orientation of the crystal. The results discussed here is in good consistency with that reported for cubic zirconia crystals irradiated by 300 keV Cs^+ ions [112]).

3.4 TEM observation of the radiation damage

The Transmission Electron Microscopy technique has been applied to investigate, at the atomic scale, the formation of defects in irradiated UO_2 crystals due to irradiation with $500-keV$ Ce ions at low fluence according to the first step of the radiation damage previously observed by RBS/C. In this investigation, high resolution images were recorded for both plan-view and cross-section geometries on the same crystal irradiated at $\Phi = 5 \times 10^{14}$ cm^{-2}.

The plan view images obtained, as displayed in figure 3-15, show the existence of dislocation loops in the irradiated sample. The dislocations appear as small ellipses and in some cases, as on the left-hand side in the image shown, they appear to be linked. The wide almost straight contrasts that extend all over the image are due to thickness variations; as indeed sample preparation induced a thickness gradient in the thinned area, away from the edge. The exact depth at which these dislocations are located is difficult to determine due to the sample preparation.

The spot shown in figure 3-16 corresponds to a projectile impact. The plan view high resolution image was taken using a ⟨100⟩ type zone axis and the corresponding diffraction pattern is shown in the inserted image. The selected area diffraction (SAD) was obtained using a selection aperture of ~ 150 nm in diameter projected on the sample. The contrast

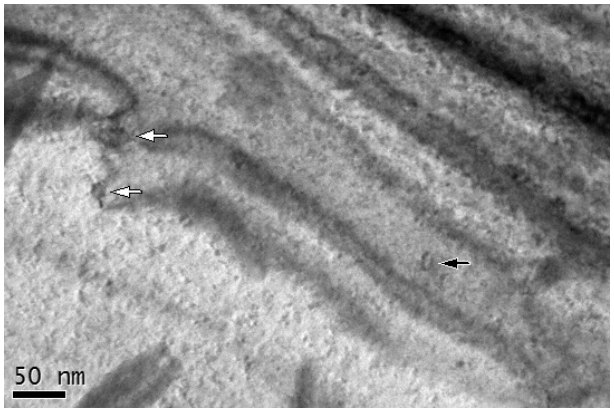

Figure 3-15: Plan view image of a UO_2 single crystal irradiated with $500 - keV\ Ce$ ions, at a fluence of $5 \times 10^{14}\ cm^{-2}$. Dislocations loops are marked with arrows. The white arrows show two linked dislocations.

difference around the impact is an indication that the angle of incidence of the projectile was not exactly normal to the surface (as predicted when the sample was fixed on a 7° sample holder to avoid channelling of bombarding ion). Worth mentioning is the absence of any other defects in the impact region meaning that a complete recovery exists, at least at the level that the image was taken.

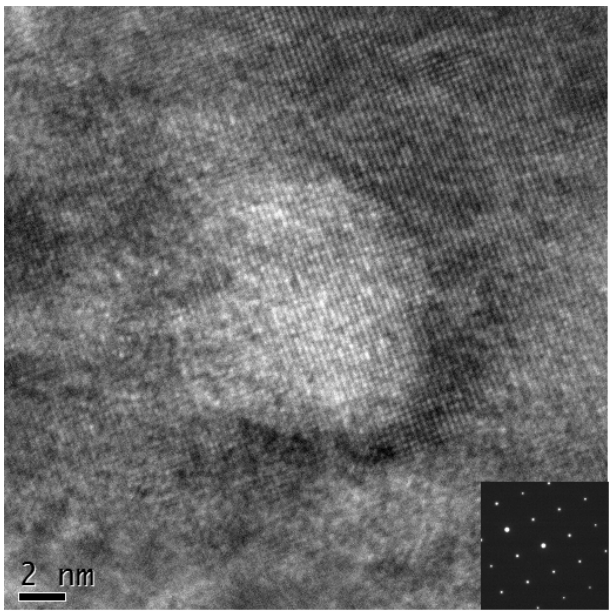

Figure 3-16: Plan view image of a UO_2 single crystal irradiated with $500 - keV\ Ce$ ions, at a fluence of $5 \times 10^{14}\ cm^{-2}$; Projectile impact, close to the surface of the specimen, and associated SAD pattern. The zone axis is of $\langle 100 \rangle$ type, as attested by the four-fold symmetry of the diffraction pattern.

In order to observe the depth and the character of the damage caused by the ion irradiation, a series of images with increasing depth from the surface were obtained from a cross-section specimen, and are shown in figure 3-17b. The path of the images along

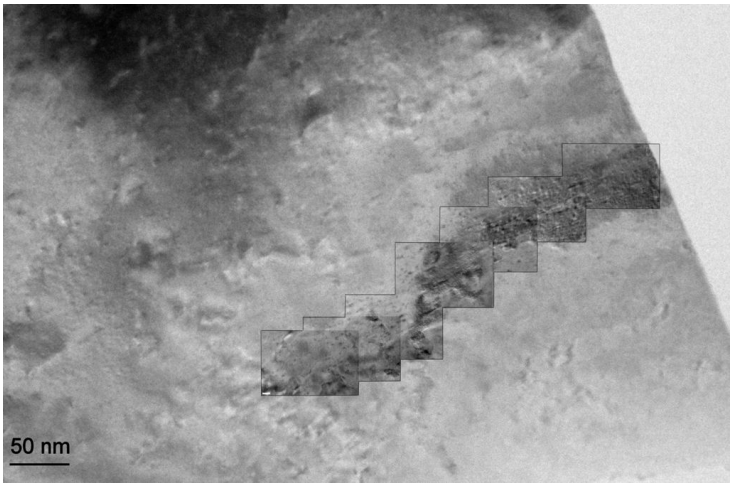

(a) General area where the high resolution sequence was taken.

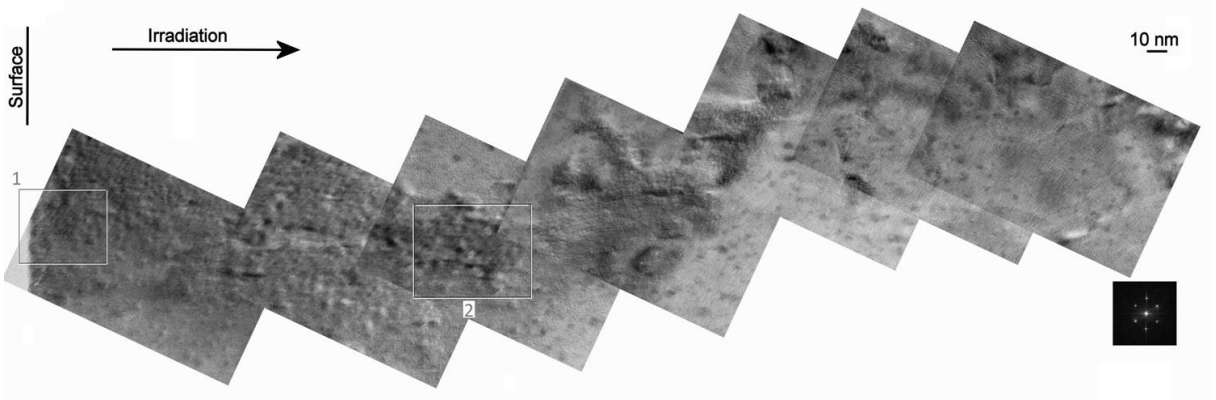

(b) Composite high resolution image ($\langle 011 \rangle$ type zone axis) over a depth of 270 nm.

Figure 3-17: Cross-section image of a UO_2 single crystal irradiated with $500 - keV\ Ce$ ions, at a fluence of $5 \times 10^{14}\ cm^{-2}$. Figure (b) is displayed as rotating 180° from figure (a) for easy following.

the cross-section tries to emulate the path of the projectiles, as shown in figure 3-17a. From these images, it is apparent that the most damaged part, that is defects and wide dislocation loops, is distributed over the first 120 nm down from the surface, while, as expected, the maximum damage is between 90 and 130 nm. These values are in excellent agreement with SRIM calculations (which give, for UO_2 irradiated with $500 - keV\ ^{142}Ce$, a projected range and a straggling range of $Rp = 86\ nm$ and $\Delta Rp = 41\ nm$, respectively) and with the experimentally measured distribution of damage extracted by the TBA approach for low fluence (see figure 3-4.a). Beyond this depth there are a few more defects visible but they are very small dislocation loops. The smooth contrast gradients over large parts of the specimen are probably due to stress introduced either during the irradiation or possibly during the sample preparation, as a thin specimen effect. It should be mentioned here that the full analysed range actually concerns the electron-transparent part of the sample; at a distance greater than $\sim$ 300 nm from the surface, no useful

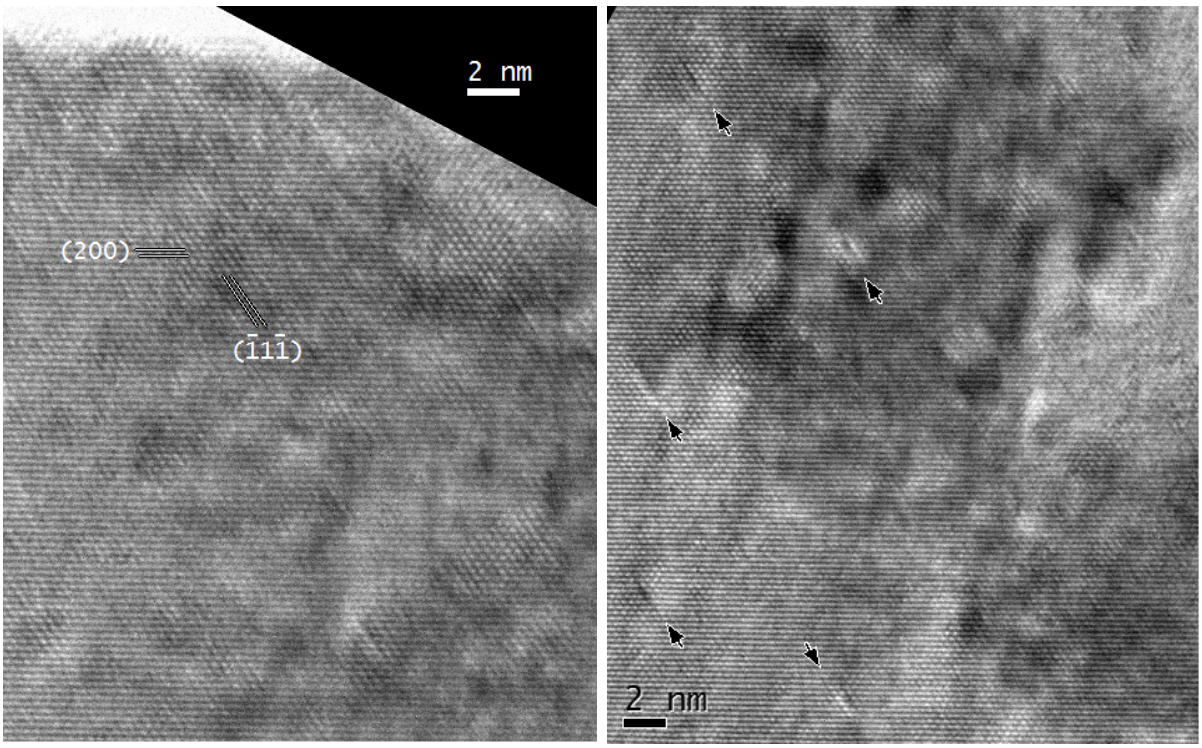

(a) (b)

Figure 3-18: Cross-section image of a UO_2 single crystal irradiated with $500 - keV\ Ce$ ions, at a fluence of $5 \times 10^{14}\ cm^{-2}$. Enlarged view (a) on the top of the composite image (upper region marked as (1) with a rectangle in figure 3-17b) and (b) in the middle of the composite image (lower region marked as (2) with a rectangle in figure 3-17b). The black arrows in figure (b) indicate selected dislocation loops lying in the (111) planes.

imaging is possible any further.

Figure 3-18a is an enlarged view of the top-most area in the sample (see rectangle (1) in figure 3-17b) in high resolution mode, as it was obtained. The (200) planes parallel to the sample surface, as well as some close packed (111) planes are indicated, and local disorientations are clearly visible on the (111) planes. Moreover, the vertical broader lines are reminiscent of irradiation tracks. This picture shows that whatever damage initially introduced by the ion irradiation, the sample area close to the surface is in almost fully recovered, as the broad dark contrast lines are a residual stress signature of the trajectory traces, whereas the atomic planes only show local distortions but no global or large-sized defects. This feature is totally consistent with the distribution of defects versus depth as measured by RBS/C (see figure 3-4.a) where significant fraction of defects is observed starting from $\sim 30\ nm$ below the surface.

The specimen region shown enlarged in figure 3-18b (see lower rectangle in figure 3-17b) is located roughly $\sim 120\ nm$ away from the sample surface. As in the previous image, vertical contrasts due to irradiation tracks are still present; and the (111) type planes are clearly visible. In this region the dislocation loops, some of them being indicated by the

black arrows are small enough (measured length $\sim 2\ nm$) so that they are easily imaged in high resolution mode. The dislocations loops are always lying in the close-packed (111) type planes, as expected for the structural space group of UO_2. Note that the dislocations, here shown because of the appropriate imaging conditions, are all aligned in the same direction; however they most probably exist in all (111) type planes, and the bright-dark contrast visible in various places are indicative for the existence of such loops lying in the other (111) planes that are in the body of the thin specimen. Defects of this type become more and more scarce as we go further down away from the surface until they finally disappear.

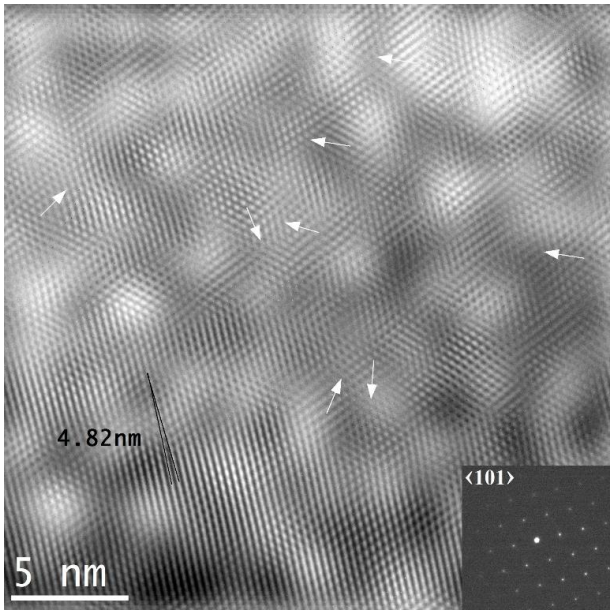

Figure 3-19: Processed image, filtered FFT and the corresponding power spectrum of UO_2 single crystal irradiated with $500 - keV\ Ce$ ions, at a fluence of $5 \times 10^{14}\ cm^{-2}$ and associated SAD pattern. The white arrows indicate selected dislocation edges.

Finally, part of the images were processed using FFT filtering, in order to obtain some more accurate characteristics regarding the defects. Figure 3-19 shows an example of an FFT filtered image and the corresponding power spectrum. A number of edge-type dislocations are indicated by the arrows. A highly disordered zone is clearly observed where dislocations are present at high density. Such an image gives the density of dislocations to be approximately of few $10^{12}\ cm^{-2}$. A thorough analysis of one dislocation (indicated by the two black lines on this figure) shows that the length of the distorted part of the two closest atomic rows amounts to $\sim 4.8\ nm$ and the angle measured between the atomic row connected to the dislocation edge and the closest one (between the two indicated black lines) is about $\sim 4°$.

3.5 Summary

To summarize, irradiation with Xe, La and Ce ions of low energy have clearly led to the formation of radiation damage in UO_2 crystals. The results measured by RBS/C and analysed by the TBA approach reveal that the radiation effects lead to a three stages for irradiation with La and Ce ions and four stages for irradiation with Xe ion of damage evolutions. At the first stage, irradiation lead to the elastic deformation of the crystalline structure. This stage is characterised by the creation of point defects of low dimension that leads to the expansion of the damaged layer toward the free surface. At the second stage, the strain/stress build-up triggers the transformation from point defects to defects cluster. This stage is characterised by the steep increase of damage observed at 4 to 7 *dpa* which is due to the creation of damage *via* ballistic collision. This stage is also observed to be independent to the nature of implanted ions. At the third stage, the fraction of created damage saturates over a long range of irradiation (from 10 to 300 *dpa* for irradiation with Xe ion and from 10 *dpa* to the highest investigated fluence for irradiation with La and Ce ions). It is also at this stage, the difference behaviour of UO_2 crystalline structure submitted to irradiation with inert noble gas (Xe) versus soluble species (La and Ce) is observed. Irradiation with inert noble gas leads to the higher damage fraction than soluble species. This clear difference between insoluble and soluble ions was observed over a large range of irradiation but such that difference due to irradiation with soluble species (La vs. Ce) is not evident. In fact, the UO_2 crystalline structure seems to response very similarly to irradiation with La and Ce ions. The fourth stage of damage evolution is observed only for implantation with noble gas Xe ions up to very high concentration. When the incorporation of Xe ions exceeds 5 at. % the dramatic increase of damage fraction takes place. This dramatic increase localises at the close surface of the crystal on the region that corresponds to the implantation range of Xe in UO_2. At this stage, due to the incorporation up to high concentration, the incorporated Xe ions tend to gather together in large quantity forming the bubbles that eventually result in the frustration of the crystalline structure. Consequently, the damage fraction increases dramatically as it can be seen on the evolution of damage measured by RBS/C.

The channelling data were analysed in the framework of the TBA approach. This approximation implicitly assumes that all created defects can be described as randomly displaced atoms. TEM results are at clear variance with such an interpretation, since the presence of extended defects, such as dislocations, were revealed. Nevertheless, channelling data are indeed intrinsically sensible to both randomly displaced (short-range order) atoms and distortions of the lattice (medium-range order). The two components can be extracted by an advanced analysis of the channelling data provided by the use of Monte-Carlo simulation codes. In the next chapter, we discuss the development of a new model -

comprising two classes of defects - that was developed to shed some light on the evolution of the populations of defects versus ion fluence and their influence on the destabilisation of the crystalline structure under irradiation.

Chapter 4

Towards an advanced description of the evolution of the urania structure under irradiation: a two-defect class model

The analysis of the structural reorganisation induced in uranium dioxide single crystals bombarded with low-energy ions used to mimic the fate of fission fragments has led to the several important conclusions. Two important steps in the process of damage formation are established: (i) at low fluence the presence of the first step scales with the number of displacements per atom and is therefore related to the radiation damage generated by atomic collision cascades; (ii) at large fluence, corresponding to a very large concentration of incorporated impurities, a huge second step is observed, specifically for crystals implanted with Xe ions, whilst, conversely, the structure of lanthanide-implanted crystals seems to be essentially insensible to the further creation of damage and incorporation of impurities up to a very large number of *dpa*. Those two steps are separated by almost constant plateaus, for which the structure for the crystal seems to be in a quasi-steady state characterised by a constant fraction of randomly displaced atoms.

The coupling of the ion channelling method with Rutherford Backscattering Spectrometry has been extensively used in the past to quantitatively investigate the depth distribution of displaced atoms from their regular atomic positions. As a first approximation, analysis of the data was performed in the framework of the so-called two-beam approximation (TBA, see the previous chapter). This model supposes the existence of two simultaneously processes: (i) direct backscattering of ions on atoms randomly located within the channels and (ii) scattering of ions that continuously interact with matrix atoms and atoms located within the matrix and thereby leave the channel at a certain depth traversed in the crystal. The latter process occurs as a consequence of a continuous series of small-angle collisions and eventually forms the dechannelling contribution to a spectrum recorded across the main crystallographic direction. The channelling spectrum comprises therefore the signals coming from the direct backscattering superimposed over

the dechannelling contribution (signal coming from forwards scattering). Let us stress that the quantitative investigation of the damage depth distribution implicitly assumes the knowledge of the nature of radiation-induced defects. The analysis performed in the previous section assumes that *only randomly displaced atoms* are generated during irradiation.

An advanced knowledge of the mechanisms of the matrix destabilisation under irradiation requires a complete analysis of the evolution of the various created defects versus fluence. Although the channelling technique is intrinsically limited when applied to the case of a highly defective material, including the presence of various types of defects, defect in crystals can nevertheless be classified according to their influence with respect to a channelled ion. As a matter of fact, they are responsible for (i) obstruction-type dechannelling (typically an atom off its regular atomic position, a stacking fault) and (ii) distortion-type dechannelling (e.g. lattice distortion, dislocations). Many defects contribute of course to both obstruction and distortions of the lattice leading to a composite dechannelling. Although the complete evaluation of the influence of various types of defects is almost impossible, the use of Monte-Carlo simulation codes allows us to propose a simplified model of defects involving both the presence of (i) randomly displaced atoms and (ii) bent channels to account for the dechannelling contributions coming from obstruction and distortion, respectively.

In the present work, such a model is used to shed some light on the mechanisms of the radiation damage production in fluorite-structured uranium dioxide. Main objectives include the determination of the damage evolution for the various types of defects leading to obstruction and distortion, as well as the understanding of the observed differences between noble-gas-irradiated and lanthanide-irradiated crystals, in relation with the nature of incorporated species.

4.1 Description of the model of defects

The radiation-induced defects are very complex and consist of various types. Their influences on the dechannelling of incident probing ions are partially, on one hand, obstructing the incoming ions and deflecting their trajectories, on the other hand. In the case of irradiation with low-energy ions, the created defects are located close to the surface of the crystal and their presence in the crystal are viewed on the axial spectrum *via* the appearance of a damage peak and *via* the dechannelling signal which is at higher level than the virgin axial spectrum. These two components are obviously the results of the presence of radiation defects with their own characteristics for each type (and hence distinct defect scattering factors). Such a complex configuration may be nevertheless simulated by a simplified model of defects, where the two dominant types are taken into account:

(i) pure interstitial atoms, small enough in order to virtually produce no lattice distortion and referred to as randomly displaced atoms; (ii) distorted channels characterised by a local curvature, hereafter referred to as bent channels, resulting in some extra transverse energy given to channelled ions. It is worth to stress that those two types of defects correspond in fact to extreme conditions of pure obstruction-type channelling and pure distortion-type channelling, respectively (i.e. defect scattering factor equals 1 and 0, respectively). Every complex mixture of defects involving different types and numbers can therefore be in principle reproduced by a distribution of defects using both types.

Let us to point out that the higher dechannelling signal observed at low energy, i.e. at depth larger than the damage profile, does not mean that the defects (or more precisely, the distortion-type defects) are created at the corresponding depth as compared to the virgin spectrum. In fact, the increasing dechannelling signal is due to the continuous interactions of probing ions with matrix ions with all types of defect including the randomly displaced atoms (RDA) and bent channels (BC). These interactions lead to the small-angle deviations of the channelled ions and finally kick off them out of the channel at a given depth. In other words, each contribution to the dechannelling signal results from the integration of small interaction over the whole thickness covered including damage area where major deviation of ions is caused by the presence of defects.

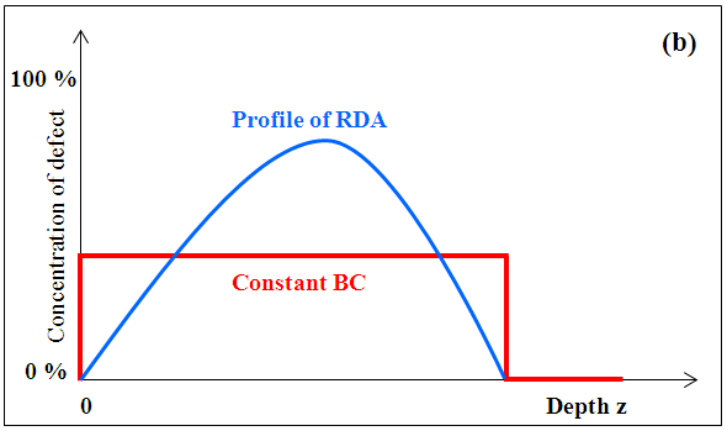

Figure 4-1: A simplified model of defects: a profile of RDA defects (blue) and a constant fraction of BC defects (red) are incorporated on the damaged layer.

For the sake of simplicity, a two-class defect model is proposed. This model assumes that both the RDA and BC are created on the same defected zone in the near-surface region, in agreement with the creation of radiation-induced defects by low-energy ions. The RDA is responsible for the damage peak, which reflects the local concentration of interstitial defects with a small contribution to the dechannelling yield, while the BC is supposed to have the major influence on the dechannelling signal. The concentration of BC is assumed to be constant over the whole damaged layer, whilst a given arbitrary

distribution of RDA is allowed over the same region (see figure 4-1). Such an approach allows one to limit the number of free parameters in such a way that the obtained results can be directly compared at various ion fluence and different type of projectiles. This simplified assumption can be considered as a thorough primary analysis in which the BC has been averaged. The limitation of such an approach will be discussed in section 4.2.3.

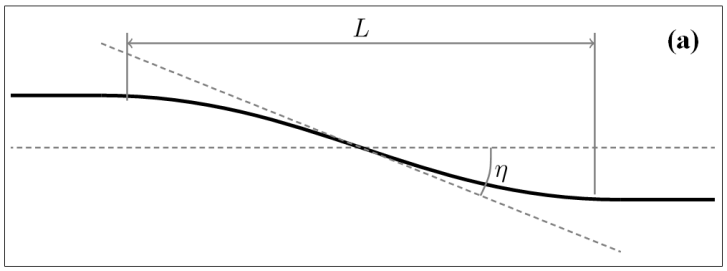

Figure 4-2: A schematic representation of bent channel defect characterised by the length (L) and the angle (η) of the distortion with respect to the channel direction.

Ben channels defect refers to atomic channels that are modified under irradiation. It refers actually to the distortion of atomic arrangement in the investigated direction. In this work the distorted atomic row is modelled by an Arctangent function, which is parameterized by the length L of the curved region and by the angle η with respect to the direction of the undistorted channels (figure 4-2). The volume fraction of bent channels is a variable and it varies in the range of 0 to 1. In addition, the fraction of randomly displaced atoms can simply be fixed at every depth from 0 to 1 (i.e. up to the hypothetical case of 100 % displaced atoms corresponding to the creation of an amorphous structure).

4.2 Simulation of axial channelling spectra by Monte-Carlo

4.2.1 Definition of the structural parameters

Monte Carlo simulations to the channelling data recorded on UO_2 crystals were performed by means of the McChasy simulation code. Positions of both U and O atoms are derived from the crystalline structure of urania (space group $Fm\bar{3}m$): U atoms are located at $4(a)$ positions (0,0,0), and O atoms are located at $8(c)$ positions $\left(\frac{1}{4},\frac{1}{4},\frac{1}{4}\right)$; $\left(\frac{1}{4},\frac{1}{4},\frac{3}{4}\right)$. The cell parameter is $a = 547.0\ pm$. The incorporated element implanted in the lattice (Xe or lanthanide ions) is assumed to be located at octahedral positions of the fluorite-type structure with an occupancy corresponding to the fraction of the foreign specie, which depends on the implantation profile and thus on depth z. The influence of the implanted element is almost negligible at low fluence, i.e. below $\Phi = 1\times10^{16}\ cm^{-2}$ (the concentration at maximum is about 1.4 % according to SRIM calculation), but it has an increasing

significant contribution at larger concentration (see chapter 3). The distribution profile of implanted species (characterised by Rp and ΔRp) is calculated by the careful analysis of the recorded experimental random RBS spectra for crystals implanted at very large fluence, whose shape in the surface region of the U signal allows the determination of the range and range straggling (see the specific shape of the random spectra on figure 3-1.d, 3-6.d and 3-8.d). Such parameters are in good agreement with values calculated by means of the SRIM simulation code ($Rp = 83\ nm$ and $\Delta Rp = 39\ nm$). These parameters are used to calculate the distribution profile at low impurity concentration, i.e. below $\Phi = 1 \times 10^{16}\ cm^{-2}$, since RBS is not sensible enough to give an accurate estimation in these experimental conditions.

Root-mean-square amplitudes of U and O atoms are measured on pristine crystals before implantation with ions. Axial channelling spectra and angular scans are recorded and they are compared to Monte Carlo simulations performed assuming a defect-free UO_2 single crystal with various values of thermal vibrations. Both values of thermal vibrations measured on U and O sub-lattice vary slightly with the crystalline quality of a given specimen and they are all in good agreement with values previously recorded on virgin UO_2 crystals [113, 114] and data derived from neutron investigations [115]. Typical values vary from $\sqrt{\langle u \rangle_U^2} = 6.0\ pm$ to $7.5\ pm$ and $\sqrt{\langle u \rangle_O^2} = 9.0\ pm$ to $12.0\ pm$.

4.2.2 The role played by randomly displaced atoms (RDA) to channelling spectra

As a first simplified approach, a defect model comprises only a distribution of RDA can be considered as an extreme configuration in which the fraction of BC equals zero, i.e., irradiation leads solely to the creation of RDA. In this configuration, the depth-distribution of RDA is the sole input data (the fraction of RDA on both sub-lattices has to be specified at every depth) and the axial spectrum calculated by Monte Carlo simulation is compared to the experimental spectrum. A typical example of analysis carried out for crystal implanted with Xe ion at a chosen fluence, namely $\Phi = 2 \times 10^{15}$ cm^{-2}, is shown on figure 4-3.

The data was analysed at the first step by the TBA approach, by which the damage peak was separated from the dechannelling signal and hence a depth-distribution of defects was calculated (see section 3.1). The distribution of defects derived from the TBA calculation has been used as an input parameter for simulation, assuming that all defects are considered as RDA, in order to test the ability to reproduce the channelling spectrum. Hence, an identical profile of RDA compared to the depth-distribution of defects extracted from the TBA approach is used for simulation (see figure 4-3.a). The calculated spectrum, which is also plotted of figure 4-3.b, reveals that the use of a profile of RDA having an

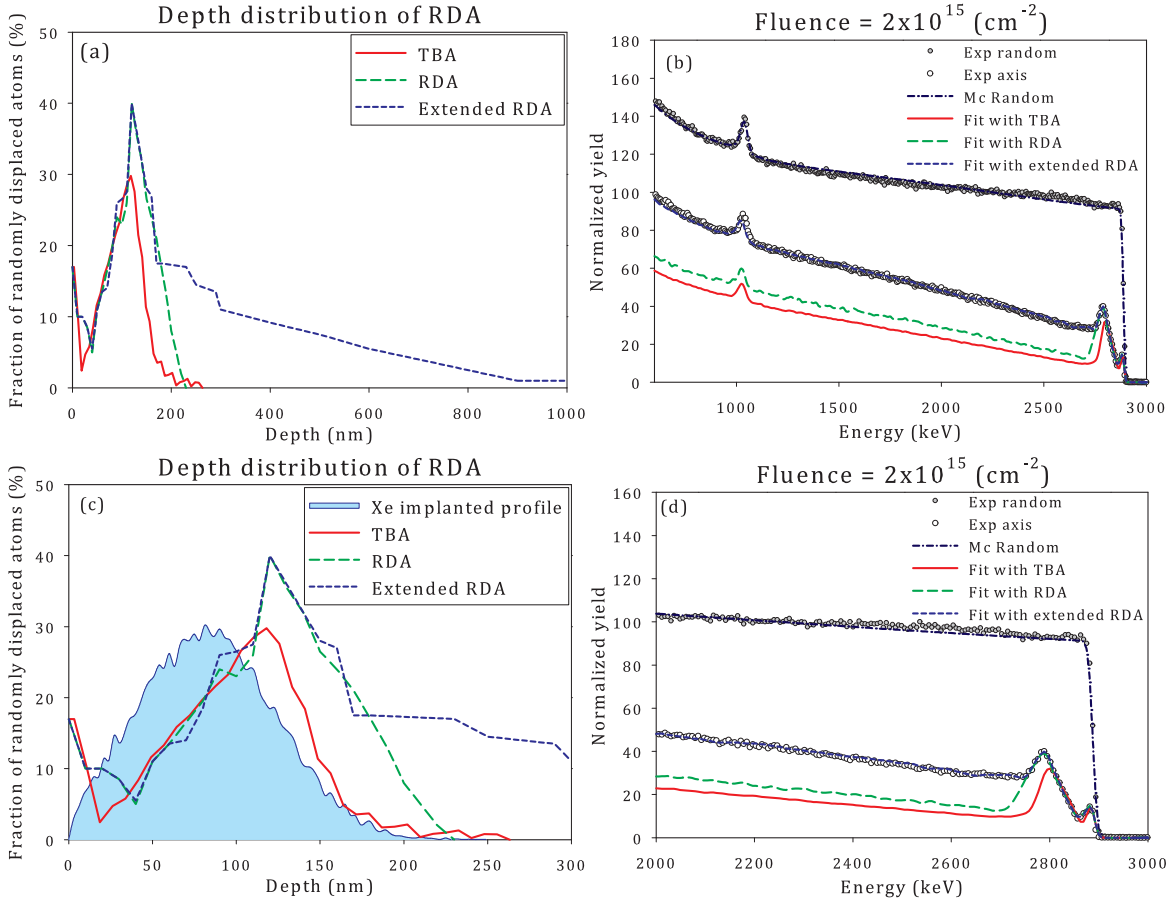

Figure 4-3: Fits to channelling spectra (b and d) assuming that RDA distributions are the sole type of defects (a and c). The red solid lines denotes the distribution of RDA (in figure (a), indicated in the legend as TBA) (see chapter 3) and the corresponding spectrum obtained from simulation (in figure (b)) with the profile of defects derived from the TBA. Long-dashed green lines denote distribution of RDA (in figure (a) and (c), indicated in the legend as RDA) that allows reproducing the damage peak and the corresponding spectrum (figure (b) and (d)). Short-dashed blue lines represent the distribution of RDA (indicated in the legend as extended RDA) that allows fitting the entire spectrum over the whole energy range of backscattered ions.

identical profile as the depth-distribution of defects issued from the TBA method cannot reproduce the experimental channelling data. A discrepancy between experimental and simulation is clearly witnessed.

Let us discuss first the dechannelling signal at a depth larger compared to the damage peak (i.e. in the undamaged zone at large depth). It is observed that the presence of RDA clearly leads to an increasing dechannelling yield as compared to the virgin spectrum, but the dechannelling yield is by far too low compared to the experimental spectrum. Considering now the damage peak, the Monte-Carlo simulation fails to reproduce the height of the damage peak; such a feature is partially due to the underestimation of the dechannelling signal discussed here before. A much lower damage peak is obtained in comparison to experimental spectrum. In addition, the simulated damage peak presents a narrower width. It is seemingly that the fraction of RDA is neither high nor wide enough

to reproduce the damage peak. Therefore, figure 4-3 clearly demonstrates that the use of the RDA with a depth-distribution directly extracted from the TBA does not allow fitting neither the damage peak nor the dechannelling signal.

An improved profile of RDA can then be applied so as to try to fit the channelling spectrum. In fact, another profile of RDA is defined as input for simulation (a table of the fraction of randomly displaced atoms on both U and O sub-lattices at every depth is defined) and the input table is modified until a good agreement between simulation and experimental data is finally reached. As it can be seen on figure 4-3.d, the damage peak is nicely reproduced by simulation: a good agreement is found both the height and the width and the peak. As shown on figure 4-3.c, the profile of RDA shows a higher fraction and a wider distribution of randomly displaced atoms versus depth as compared to the depth-distribution of defect extracted from TBA approach. However, even if these additional defects slightly improve the dechannelling yield, a much lower dechannelling signal is still evidenced. The underestimation of the dechannelling yield provides strong evidence that in order to fully fit the spectrum either (i) a broader defects distribution is necessary or (ii) other classes of defect need to be taken into account to compensate the difference between experimental and calculated dechannelling yields.

The first hypothesis is tested in this section. The profile of RDA is extended to larger depth (at depths larger compared to the damage peak) to increase the level of the dechannelling yield. As seen from the figure 4-3.b, the new profile of RDA allows an excellent fit to the channelling spectrum up to very larger depth (up to typically over 2 μm). However, a much broader depth-distribution of RDA is necessary to account for the observed calculated axial spectrum. A non-zero fraction of RDA is needed up to a depth far larger than the implanted profile of Xe ions (represented by filled area on figure 4-3.c). As observed on the figure 4-3.a, a significant fraction of RDA is created up to 1 μm meanwhile the maximum depth of $Xe-$implanted in UO_2 calculated by SRIM is only 200 nm (see the filled area). Such a result is physically unacceptable. The discussed results reveal that channelling data analysed by simulation with the sole contribution of RDA fails. The resulting spectrum shows either an underestimated dechannelling signal or an unphysical distribution of RDA versus depth. Other classes of defect definitely need to be taken into consideration.

4.2.3 The role played by the bent channel (BC) class of defects

In the previous section we show that the use of a distribution of Randomly Displaced Atoms does not provide a satisfactory fit to the channelling data. As an alternative approach, channelling data was analysed assuming that the contribution of RDA is fully cancelled and that bent channels are the sole type of defects created under irradiation

with low-energy ions. This configuration shares strong similarities with the case where only dislocations are located in the defective crystal. Figure 4-4.a displays the channelling spectrum recorded for the $Xe-$implanted crystal at a fluence $\Phi = 2\times10^{15}\ cm^{-2}$ (the same fluence that has been analysed by RDA) and the fitted spectra for comparison. At first, the experimental spectrum was fitted assuming a distribution of BC identical to the profile of radiation damage extracted by the TBA method. As a second possibility, a very sharp distribution of BC is constructed based on the actual implanted profile of Xe ions in the damage area (a maximum BC fraction of 95 % located at the depth of 80 nm, i.e. around the Xe implanted range) is employed for simulation. Finally, a constant distribution of BC is also tested for the sake of simplicity. All simulated spectra and the corresponding profiles of BC are shown on figure 4-4.a and figure 4-4.b, respectively.

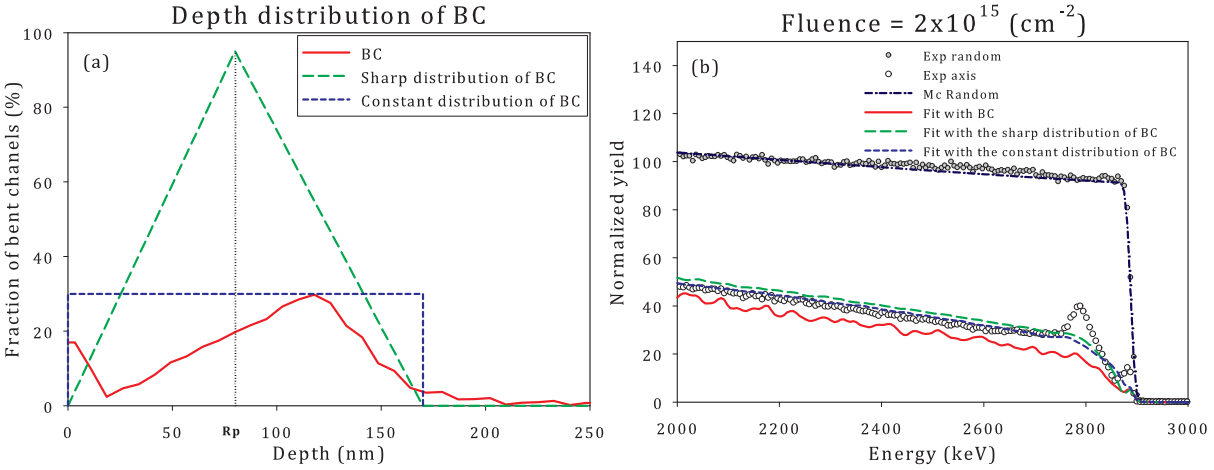

Figure 4-4: Fit to channelling spectrum assuming the sole presence of bent channels as radiation-induced defects ($L = 5\ nm$ and $\eta = 1.5°$). The red solid line denotes the simulated spectrum and the corresponding distribution of BC assuming both the depth distribution and the concentration derived from the TBA. Long-dashed green line denotes the simulated spectrum and the corresponding sharp distribution of BC (up to 95 % of BC). Short-dashed blue line represents the calculated spectrum assuming a constant distribution of BC from the surface up to a given depth. Dotted line help showing that the sharp distribution of BC is centred at the ion's implanted range.

As it can be seen from the figure 4-4.b, the use of a profile of BC with the depth-distribution extracted from the TBA method does not provide a satisfactory agreement between experimental and calculated axial spectra. The first tested distribution of BC appears to be at a clear variance with the experimental data. As observed on the figure 4-4.b, the simulated spectrum shows an increasing dechannelling yield with decreasing energy of the backscattered ions. The dechannelling yield has a similar trend compared with the experimental dechannelling yield but an underestimation in the yield is clear seen. Moreover, the backscattering signal on the defected zone close to the surface does not show any damage peak as compared to the experimental spectrum. Only a steep increasing of the signal on the damage layer is observed with increasing depth, a feature

which was anticipated since the presence of bent channels does not involved the presence of direct-scattering centres. Thus, the use of a distribution of BC with the profile issued from TBA approach fails to reproduce the channelling spectrum especially the damage peak.

In order to check if the presence of the damage peaks could be accounted for by the sole contribution of BC, a sharp profile of BC is employed. As viewed on figure 4-4.b, a new distribution of BC is used as input data up to the same depth at which a significant fraction of defects extracted by the TBA method is still observed, i.e. $\sim 160\ nm$. The maximum fraction of 95 % of BC is fixed at around 80 nm, i.e. at a depth corresponding to the maximum fraction of $470-keV\ Xe$ ions implanted in UO_2. The resulting spectrum obtained from simulation reveals once again that even though a very sharp distribution of BC is used, no damage peak can be evidenced. The simulated spectrum shows the same increasing spectrum with decreasing energy of the analysing ions previously observed. Conversely, the dechannelling yield shows a higher level (due to the higher fraction of BC) but a similar trend (slope) of the dechannelling yield is witnessed compared to the experimental data. As a conclusion, the dechannelling yield can be easily reproduced with a suitable distribution of BC.

Since the use of BC essentially affects the level of the dechannelling yield, a constant distribution of BC should also be tested. As seen on figure 4-4.b, a constant distribution of BC from 0 up to 175 nm with a fraction of 30 % is used as input. The result obtained is quite interesting since the spectrum obtained is very similar to the one calculated assuming a sharp distribution of BC. On the defected zone, no damage peak is observed: the signal increases rapidly with increasing depth. Beyond this zone, the dechannelling signal reveals a similar behaviour compared to the dechannelling yield obtained using the sharp profile of BC. The result discussed here lead to a very important conclusion: since the calculated dechannelling yield reveals to be eventually insensitive of the exact details of the depth distribution of BC, a constant profile of BC is then assumed for the sake of simplicity in the following Monte-Carlo simulations to account for the radiation damage created by ion irradiation.

To summarise, simulation with the sole contribution of BC can allow reproduction of the dechannelling yield but it fails to reproduce the damage peak. BC merely leads to a gradual increasing dechannelling yield irrespective of the exact details of the depth distribution of BC defects. In fact, the BC does not act as an obstruction centre to the probing ions and hence do not lead to a significant increase of direct backscattering events. They influence the pathway of probing ions through a series of small-angle scattering. As a result, the backscattering of ions takes place at a certain depth transversed. The deeper the depth transversed by ions, the higher the probability to be dechannelled and hence

the higher the signal is recorded. A complete analysis of the channelling data recorded on low-energy ion-irradiated crystals requires a model involving the contribution of a more complex type of defects, since the sole contribution of BC does not allow a satisfactory description of the radiation damage.

4.2.4 Monte Carlo simulations with the complete model of defects: RDA- and BC-type

In the section 4.2.2 and 4.2.3, Monte Carlo simulations performed with the unique contribution coming from either the RDA or the BC type of defects fail to reproduce the experimental channelling spectra. The RDA-type of defects can reproduce the damage peak but it clearly underestimates the dechannelling yield at depths larger than the implantation profile. Conversely, the use of the BC-type of defects allows a nice fitting of the dechannelling contribution but the presence of the damage peak cannot be obtained. Therefore, the BC-type of defects should be used in combination with another type of defects that allows the reproduction of the damage peak. The RDA-type of defect figures, of course, as an obvious candidate that fulfils those requirements. In fact, the RDA-type of defects allows one to fit the damage peak whilst BC can be used as a complementary factor to improve the fitting of the dechannelling signal.

To fit a channelling spectrum with the combination of RDA- and BC-types of defects, the same procedure is followed for every channelling spectra recorded at a given implanted fluence. In the first step, a profile of RDA is employed as the sole class of defect to fit the damage peak. As a consequence (see section 4.2.2), the simulated spectrum shows an underestimated dechannelling yield compared to the experimental spectrum. In the next step, the BC-type of defects is applied to improve the fit. The constant fraction of BC over the entire thickness of damage zone is progressively increased from 0 by small steps until the best fit is finally achieved. It is worth stressing that the presence of BC implies the need to modify the profile of RDA at every step to maintain the quality of the fit to the damage peak. In fact both BC-type and RDA-type of defects contribute to the dechannelling signal, whilst only the RDA-class of defects has a significant contribution to the direct scattering yield. As it was demonstrated in the section 4.2.3, the use of BC improves not only the dechannelling yield but also gives an extra contribution to the backscattering yield on the damage region, i.e. the damage peak. Experimental channelling spectra are fitted by MC simulation until the combination of RDA and BC produces the best agreement between experimental and simulations. Both depth distributions of RDA and BC are then extracted and they provide quantitative measurements of the defects distribution measured by the ion channelling technique.

As indicated in the description of the model of defects, BC is characterised by two

parameters that are the length and the angle of bent channel (see section 4.1). Therefore, the choice of these two parameters directly affects the contribution of BC to the channelling spectrum. However, these two parameters result in the subsequent contribution of BC to the simulated channelling spectra in opposite ways. The angle of the distorted part has a straight influence on the dechannelling yield as it refers to the imperfection of the atomic channel. This imperfection results in an extra transverse force acting on the channelling ions. This force is perpendicular to the trajectory of channelling ions that progressively deviates and eventually dechannels the probing ions. Therefore, the higher the angle of distortion is, the higher probability to be dechannelled the ions have and the higher the dechannelling yield is obtained. A clear example that represents the influence of the angle of distorted part is shown on figure 4-5.a.

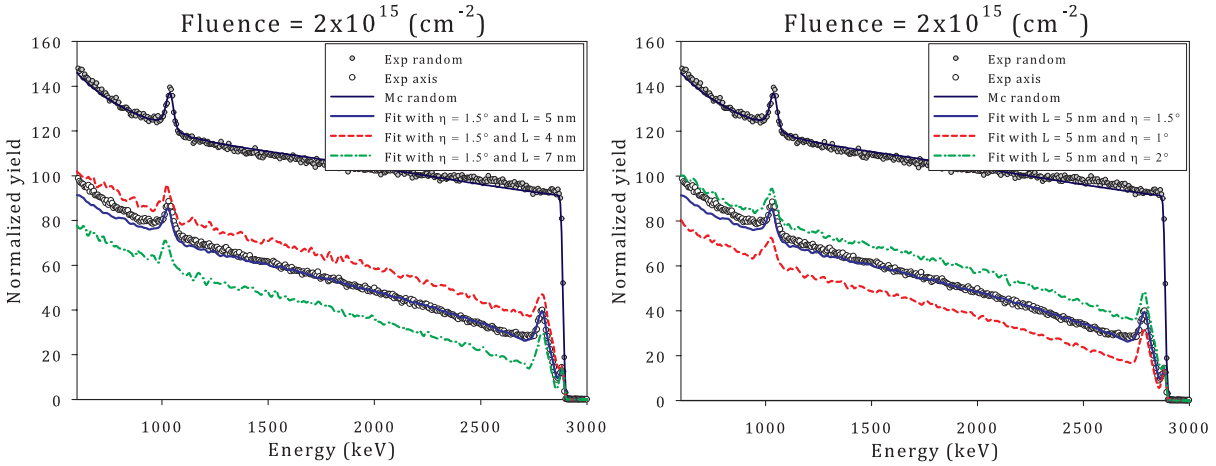

Figure 4-5: Examples showing the influence of (a) the length L and (b) the angle η of distorted channels to the simulated channelling spectra. The distribution of RDA and the constant distribution of BC are fixed according to the best fit which is obtained for $L = 5\ nm$ and $\eta = 1.5°$.

Conversely, the length of the distorted part has inverse influence on the dechannelling yield. The higher length of the distorted part will reduce the intensity of interaction (intensity of transverse force over unit of thickness covered by analysing ion) that leads to the deviation of the channelled ions. The higher the length of distortion is, the smaller the intensity of transverse force becomes. Hence, the smaller angle the ion is deviated (scattered) and therefore the lower dechannelling yield is consequently obtained. The direct influence of the length of distorted part to the simulated channelling spectra is demonstrated on figure 4-5.b. The two parameters affect the contribution of BC to the channelling spectra in two opposite ways. It is then important to specify the suitable intervals for the two parameters such that (i) the combination of these two parameters reasonably reflects the true created defects and (ii) the combination of BC + RDA allows the reproduction the channelling spectra. These parameters also need to be in reasonable

agreement with the defects that are observed by other alternative investigating technique, e.g. the HRTEM observation on dislocation. The following discussion will focus on the use of the complete model of defects (RDA + BC) to analyse channelling data in which the angle and the length of distortion are fixed to be $L = 5\ nm$ and $\eta = 1.5°$ for all three crystals. The choice of these values will be discussed in section 4.3.4.

4.3 Damage evolution

As a result of analysis, the distributions of RDA and BC versus depth have been extracted from the channelling spectra. This section focuses on the analysis of channelling data by Monte-Carlo simulations and on the evolutions of both distributions of RDA and BC defects versus ion fluence. Afterwards, this section discusses also the evolutions of the fraction of the defects created versus the accumulated ion fluence. Results obtained for irradiation with all the three implanted elements will be shown and commented. Moreover, a comparison between the effects due to the irradiation by ions of different chemical nature is discussed.

4.3.1 Analysis of channelling spectra

Channelling data corresponding to the $470-keV\ Xe-$implanted crystal are analysed by Monte-Carlo simulation using the complete model of defects. All the spectra have been fitted with the combination of RDA and BC. Figure 4-6 displays the best fits to experimental channelling spectra obtained from simulation for Xe implanted crystal at various ion fluences. It is worth noticing that experimental RBS/C spectra are remarkably fitted and that a good agreement between experimental data and simulation is obtained over a large energy window. Only at large depth, i.e. at depths largely exceeding the damaged zone $z > 1\ \mu m$, a discrepancy is observed for some fluences. Such feature is likely due to the multiple scattering processes (that were not taken into account in the computational code) and to the inaccuracy of the stopping cross sections at large depth. They do not limit the present Monte Carlo investigations. The agreement between experimental axial spectra and the defect model involving both RDA and BC is really excellent in the energy window from 2000 to 2887 keV (corresponding to a depth from 0 to 1 μm), as it can be seen from figure 4-6.a and figure 4-6.b. Figure 4-6 also reveals that the damage peaks, observed on the channelling spectra at the indicated ion fluence, have been nicely reproduced by the combination of RDA and BC. Both the increase and the broadening into the larger depth of the damage peak as increasing ion fluence have been totally accounted for by simulation. Even at very high implanted fluence (larger than $\Phi = 1 \times 10^{16}\ cm^{-2}$) the dramatic increasing of the signal observed on the damage peak (close to the surface of the crystal) has been fitted satisfactorily. The complete model of defects (RDA + BC) has, therefore, succeeded in reproducing the channelling spectra

recorded in crystal implanted with low-energy ions.

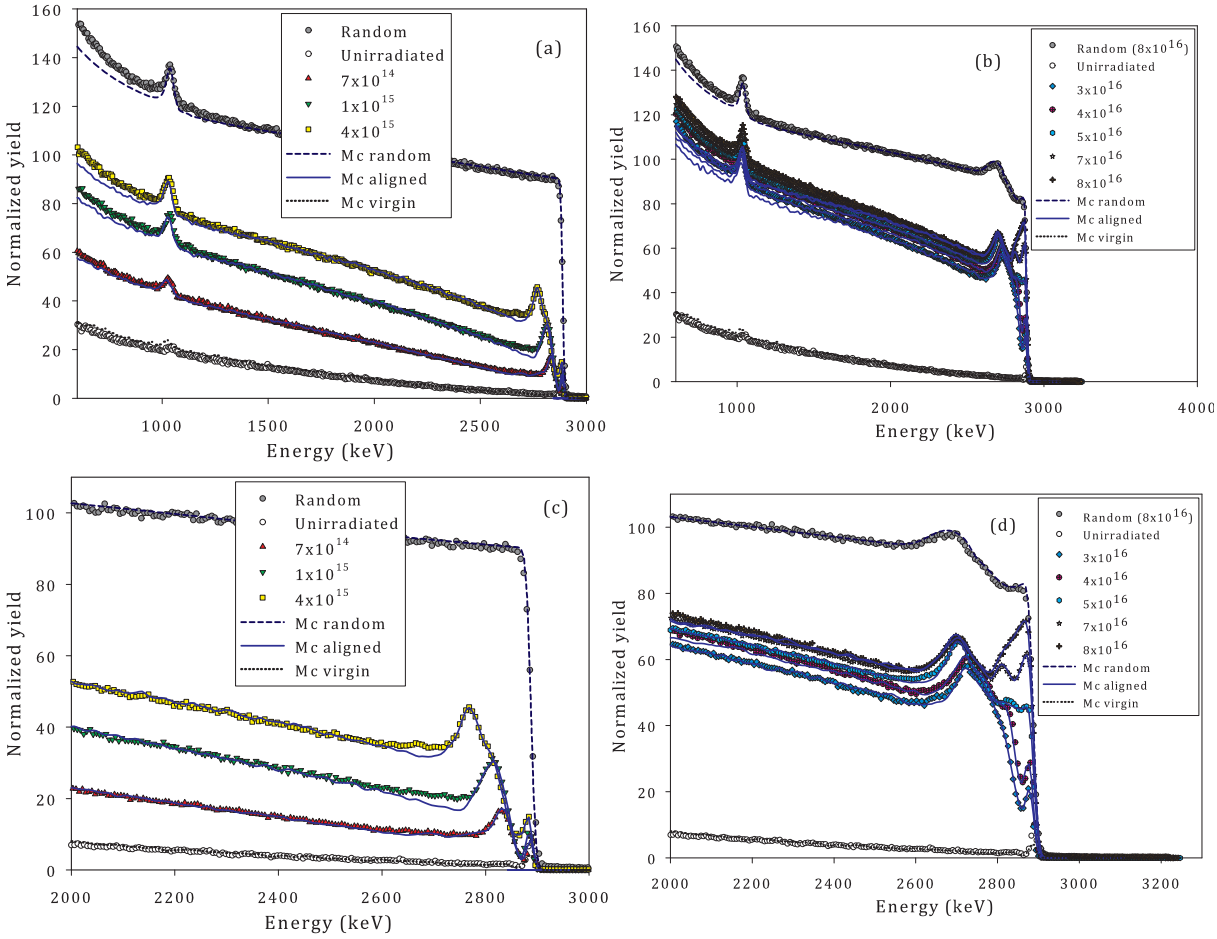

Figure 4-6: Best MC simulations to RBS/C spectra recorded for $Xe-$implanted crystal in random condition (dashed line) and in axial aligned condition for virgin (dotted) and UO_2 implanted crystal (solid line). Experimental channelling spectra are plotted in symbols and the fluences are expressed in unit of cm^{-2}. (c) and (d) are zooms in the surface region of figure (a) and (b). Fits were performed assuming $L = 5\ nm$ and $\eta = 1.5°$.

It is also important to point out that a systematic discrepancy is observed for some fluences. As viewed on figure 4-6.c, the simulated channelling signal just after the damage peak (i.e. corresponding to the energy range from 2650 keV to 2750 keV) is underestimated compared to the experimental spectra. Such discrepancy can be easily solved by extending the profile of RDA into deeper layer. With an extended profile of defect, channelling spectra can be reproduced with much better agreement with respect to the experimental data but once again the result leads to a distribution of defect with the depth largely exceeding the maximum depth of implantation, i.e. a non-physical depth-distribution of defects (see section 4.2.2). This discrepancy appears as a limitation of the two-defect class model of defect that cannot allow an exact reproduction of channelling data. A better decomposition of defects, involving a more complex description might likely solve this discrepancy.

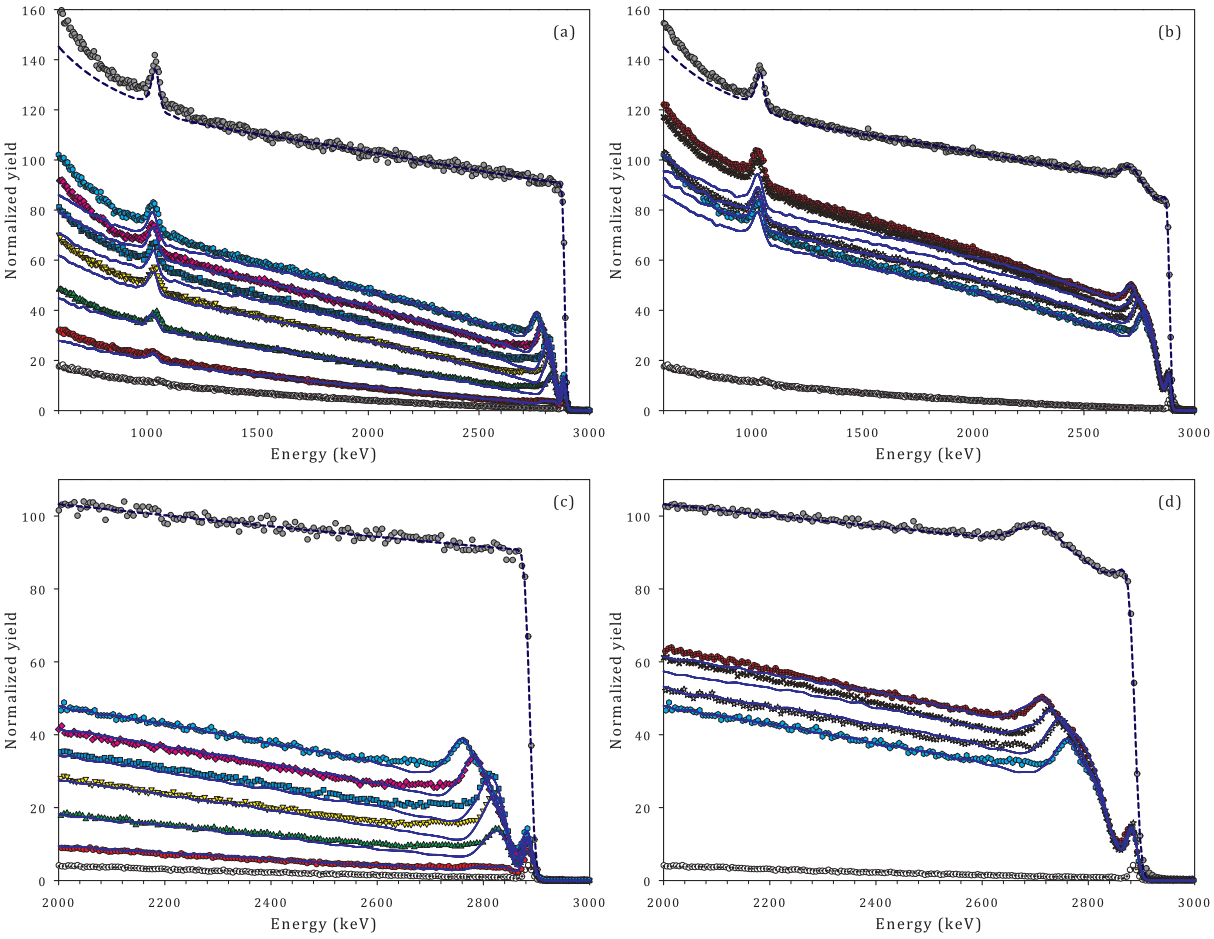

Figure 4-7: Best MC simulations to RBS/C spectra recorded for La-implanted UO_2 crystal at low (a) and high (b) fluences. The zooms on high energy part are shown on figure (c) and (d) respectively. Dashed and dotted lines denote the best MC simulations to random and axial virgin spectra. Solid lines denote best fits to axial aligned spectra recorded for irradiated crystal. Experimental channelling spectra are plotted in symbols for fluences of $\Phi = 3 \times 10^{14}$ cm^{-2} (red circle), 7×10^{14} cm^{-2} (green triangle up), 8×10^{14} cm^{-2} (yellow triangle down), 1×10^{15} cm^{-2} (violet square), 2.5×10^{15} cm^{-2} (pink diamond), 5×10^{15} cm^{-2} (cyan hexagon), 1×10^{16} cm^{-2} (gray star), 2×10^{16} cm^{-2} (orange cross) and 3×10^{16} cm^{-2} (red crossed-circle). Fits were performed assuming $L = 5$ nm and $\eta = 1.5°$.

The evolution of the shape of the random spectra versus implanted ion fluence deserves a discussion. In fact, as it was already mentioned, the MC simulations were performed assuming the presence of the implanted species located at the octahedral positions in the lattice structure with a content corresponding to the ion fluence. As it can be seen from the figure 4-6.b, the exact shape of experimental random spectra is fully accounted for the presence of extra-incorporated atoms (see for instance the shape of the random spectrum recorded when the crystal is irradiated at the highest fluence of 8×10^{16} cm^{-2}). The incorporation of Xe ions to high concentration leads to a random spectrum with both (i) a lower backscattering yield at the surface due to the modification of the stopping power on the implanted layer compared to the un-irradiated crystal and (ii) the appearance of a peak located in between 2600 and 2700 keV originated from the

backscattering of probing ions on Xe atoms located in the matrix (the front of backscattering signal due to Xe atoms found at the surface of the crystal locates at 2737 keV). All those modifications of the random spectra are reproduced by the incorporation of Xe into UO_2 crystalline structure with a profile corresponding to implantation.

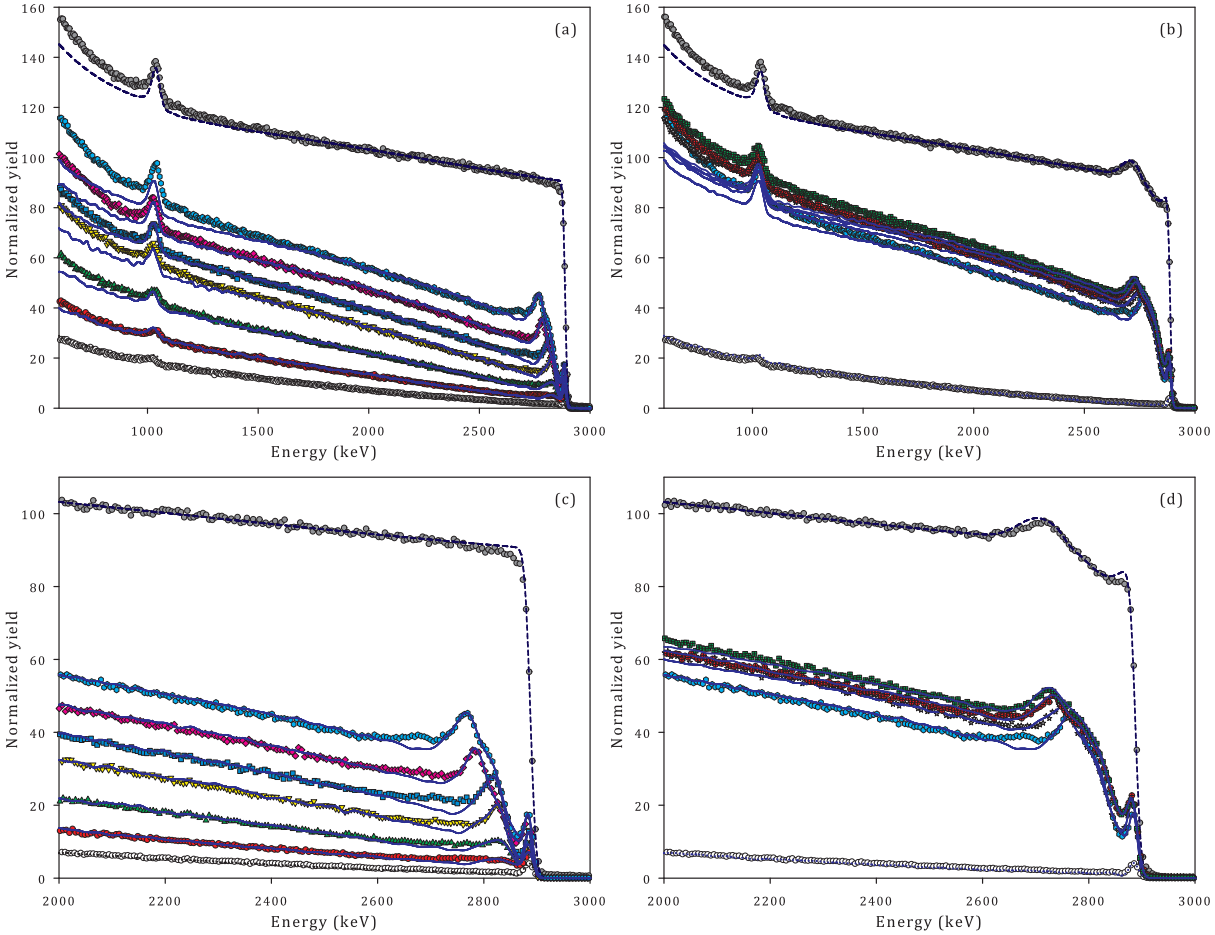

Figure 4-8: Best MC simulations to RBS/C spectra recorded for Ce-implanted UO_2 crystal at low (a) and high (b) fluences. The zooms on high energy part are shown on figure (c) and (d) respectively. Dashed lines and dotted lines denote the best fits to random and axial virgin spectra. Solid lines denote best MC simulations to axial aligned spectra recorded for irradiated crystal. Experimental channelling spectra are plotted in symbols for fluences of $\Phi = 2 \times 10^{14}$ cm^{-2} (red circle), $7{\times}10^{14}$ cm^{-2} (green triangle up), $8{\times}10^{14}$ cm^{-2} (yellow triangle down), $1{\times}10^{15}$ cm^{-2} (violet square), 2.5×10^{15} cm^{-2} (pink diamond), 5×10^{15} cm^{-2} (cyan hexagon), 1×10^{16} cm^{-2} (gray star), 3×10^{16} cm^{-2} (red crossed-circle) and 4×10^{16} cm^{-2} (green crossed-square). Fits were performed assuming $L = 5$ nm and $\eta = 1.5°$.

A similar analysis has been performed regarding channelling data recorded for crystal implanted with lanthanide atoms, i.e. $500-keV$ La and $500-keV$ Ce ions. Analyses have been performed employing the same procedure as for crystal implanted with Xe. The similar evolution of the radiation damage was considered for La and Ce implanted in UO_2. Figure 4-7 and figure 4-8 display best Monte-Carlo simulations to the experimental backscattering data obtained along the main crystallographic direction, recorded on both $La-$ and $Ce-$implanted single crystals, respectively. As it can be seen from the figures,

a good agreement between experimental and simulated spectra is revealed over a large energy range of the probing ions, as it was the case for $Xe-$implanted crystals. A discrepancy was also observed at the depths exceeding the damaged zone for some fluence below $\Phi = 1 \times 10^{16}\ cm^{-2}$. This discrepancy is systematic as it presents in all three analysis. However, this discrepancy does not limit the usefulness of the analysis with the complete model of defects. As a main conclusion of this section, all the results confirm that axial channelling spectra can be accurately reproduced by MC simulation with the assumption of defects comprising a profile of RDA and a constant concentration of BC-type of defects. It is remarkable that the simulation of the axial spectra can be performed with the same value of the BC parameters (L, η) over an extensive range of fluence. Such a feature allows a comparison of the parameters over the entire fluence range.

4.3.2 Evolution of the randomly displaced atoms defects

As already mentioned in the description (see section 3.3), irradiation on UO_2 single crystals have been performed with the implanted ion fluence ranges from 0 to 8×10^{16} cm^{-2}. For the sake of simplicity and after a careful interpretation of the data, the results obtained can be divided and hence discussed in three ranges according to the irradiated fluence: the small, the medium and the high fluence ranges. The small implanted fluence range varies from 0 to $\Phi \leq 1 \times 10^{15}\ cm^{-2}$, the medium implanted fluence range varies from $\Phi \geq 1 \times 10^{15}\ cm^{-2}$ to $\Phi \leq 1 \times 10^{16}\ cm^{-2}$ and the very high implanted fluence range refers to the fluences $\Phi \geq 1 \times 10^{16}\ cm^{-2}$.

(i) Figure 4-9.a depicts the distribution of RDA defects versus depth measured at low ion fluence for crystals irradiated with Xe, La and Ce. For irradiation with all the three elements, the creation of RDA shows a similar behaviour. The fraction of RDA is created mainly around the range of implanted ion. As observed from figure 4-9.a, the radiation damage centres around 80 nm, close to the implanted range of projectiles (see Table 1.2). This feature is similar for irradiation with Xe, La and Ce and appears clearly for a given implanted fluence. Let us take, for instance, $\Phi = 8 \times 10^{14}\ cm^{-2}$ and $\Phi = 1 \times 10^{15}\ cm^{-2}$, the maximum fraction of RDA are observed to locate exactly at same depths of 80 nm and 90 nm respectively. As the ion fluence increases, the fraction of created RDA increases progressively. These features, that are similar for irradiation with ions of different nature, clearly confirms that the irradiation with low energy ions lead to similar effects and is independent to the chemical nature of projectiles. It is also apparent that the depth-distributions of the RDA calculated by simulations for low ion fluence (below $\Phi = 1 \times 10^{15}\ cm^{-2}$) share similar features compared to the profiles of defects extracted by TBA approach (see figure 3.a, figure 5.c and figure 5.d, in chapter 3).

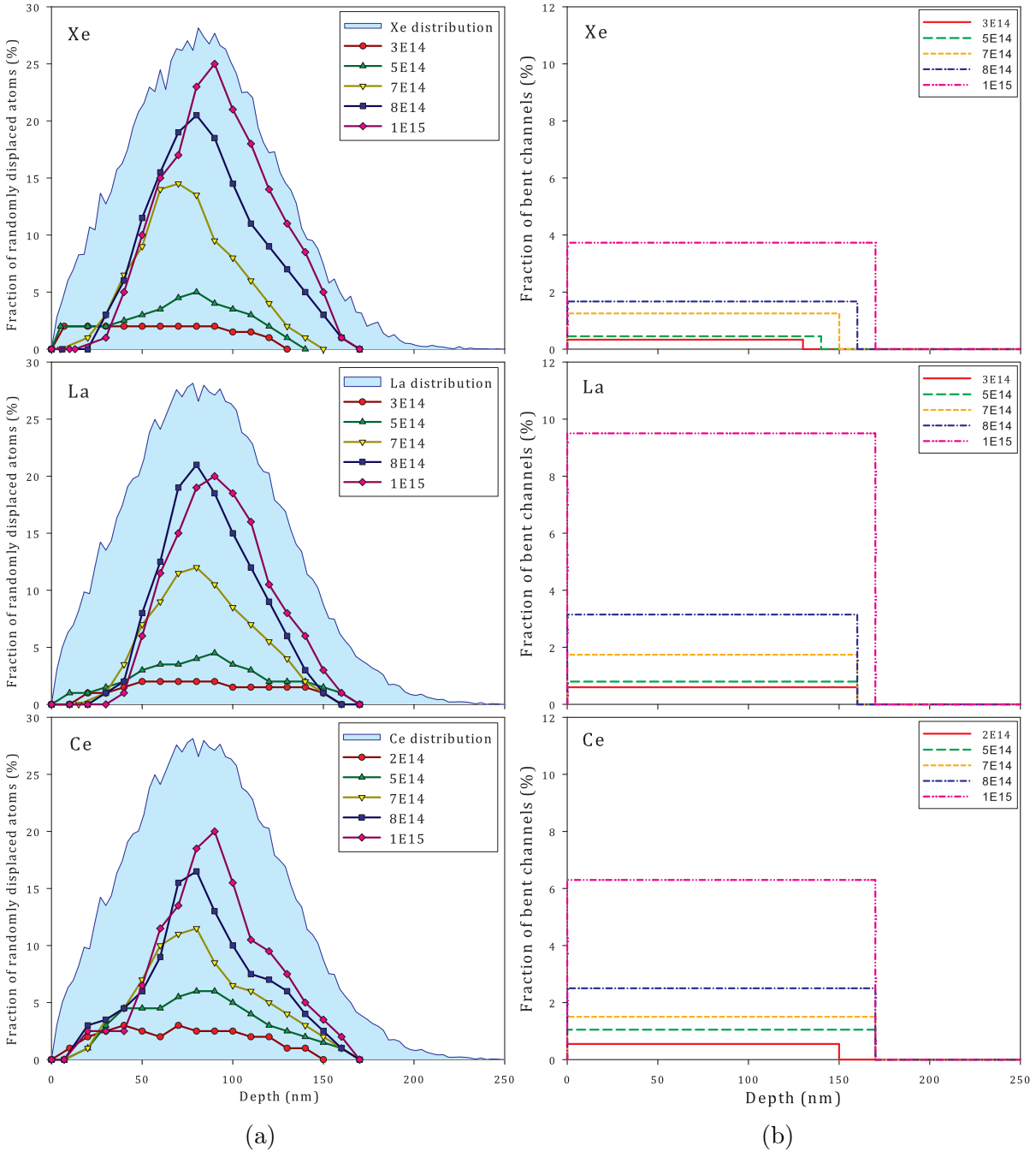

Figure 4-9: Distributions of RDA (a) and BC (b) versus depth measured for UO_2 crystal implanted with Xe, La and Ce at low fluence ($\Phi \leq 1 \times 10^{15}\ cm^{-2}$) extracted from MC simulations. BC is parameterized by $L = 5\ nm$ and $\eta = 1.5°$. Fluences are measured in the unit of cm^{-2}. Xe, La and Ce implantation profiles calculated by SRIM (represented by filled area) are plotted in arbitrary unit.

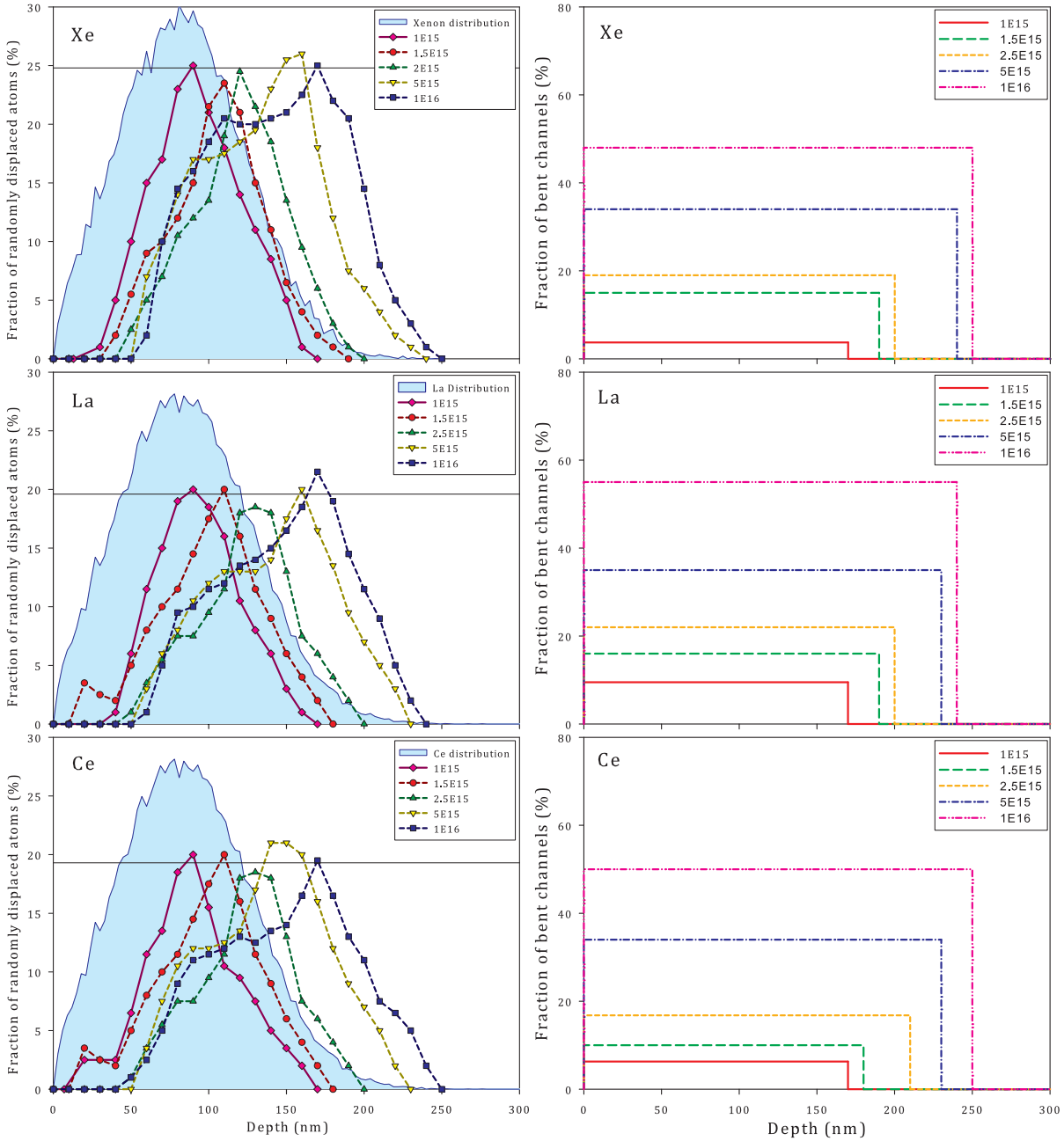

Figure 4-10: Distributions of RDA (a) and BC (b) versus depth measured for UO_2 crystal implanted with Xe, La and Ce at medium ion fluence derived from MC simulations. BC is parameterized by $L = 5\ nm$ and $\eta = 1.5°$. Fluences are measured in the unit of cm^{-2}. Horizontal solid lines plotted on figure a represents the average of the maximum fraction of RDA calculated over the medium ion fluence range. Xe, La and Ce implantation profiles calculated by SRIM (represented by filled area) are plotted in arbitrary unit.

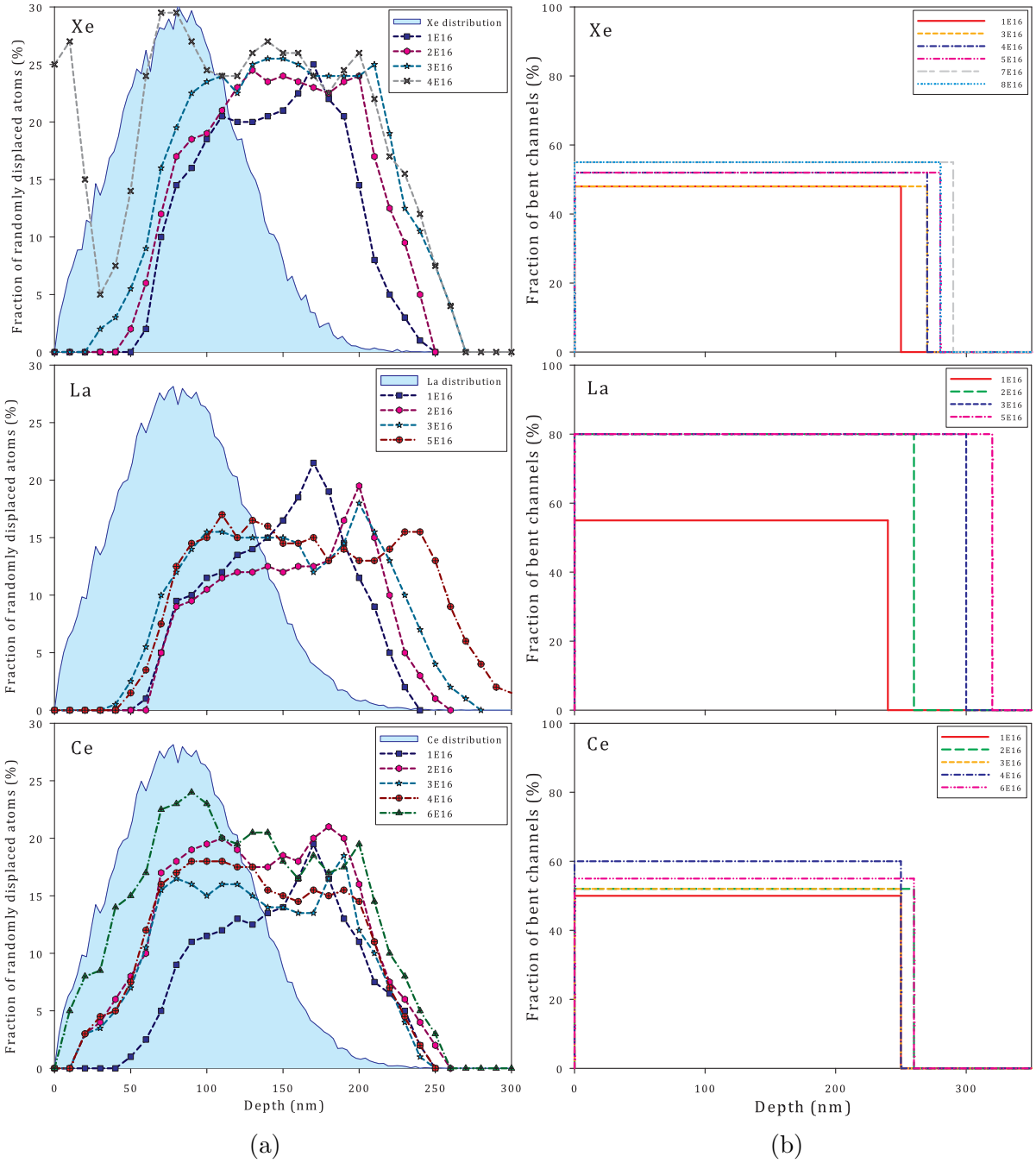

Figure 4-11: Distributions of RDA versus depth measured for UO_2 crystal implanted with Xe, La and Ce at high fluence derived from simulations. BC is parameterized by $L = 5\ nm$ and $\eta = 1.5°$. Fluences are measured in the unit of cm^{-2}. Xe, La and Ce implantation profiles calculated by SRIM (represented by filled area) are plotted in arbitrary unit.

(ii) In the medium ion range, the radiation damage follows a completely different behaviour compared to the low ion fluence range (see figure 4-10.a). Nevertheless, a similar behaviour of the radiation damage is once again observed for all the three implanted elements. Firstly, the radiation damage created is gradually shifted towards larger depths (larger than the implanted range $Rp+\Delta Rp$) with increasing ion fluence. As a consequence, the width of the distribution of RDA is progressively enlarged as the irradiation fluence increases. In other words, by increasing the accumulated ion fluence, the damage zone broadens (extends) versus the greater depth, for instance up to the depth of 250 nm, which is far larger beyond the implanted range of $(Rp+\Delta Rp) \sim 120$ nm, for $\Phi = 1 \times 10^{16}$ cm^{-2}. Secondly, over the whole medium ion fluence range, there is almost no variation of the maximum fraction of radiation damage. The maximum fraction of RDA saturates in all the three crystals. Radiation damage seems to be saturated over the medium ion fluence range. The only noticeable difference that can be observed is related to the nature of implanted ions. The radiation damage in the crystal implanted with $470 - keV$ Xe saturates at a higher level (the average of maximum RDA is 25 %) compared to the $La-$ and $Ce-$implanted crystals where this saturation is observed at a lower but almost identical value (the average of maximum RDA is 20 and 19 % for $La-$ and $Ce-$implanted crystals, respectively). The features discussed here, that concern the distribution of RDA, are similar to those observed on the profiles of defects extracted from TBA approach (that are represented on figure 3-4.b, figure 3-7.b and figure 3-9.b). Nonetheless, the level of saturations is lower for the distributions of RDA (25 % for irradiation with Xe and 20 % for irradiation with La and Ce) as compared to the profiles of defects extracted by TBA approach (30 % for irradiation with Xe and 25 % for irradiation with La and Ce). The difference is well understood since the model of defects applied into the simulation assumes two types of defects while the TBA approach gives a distribution of defects that contains all types of defects.

(iii) In the high fluence range, the distribution of RDA presents both similarities and differences for irradiation with noble gas Xe ion compared to La and Ce ions (figure 4-11.a). The figure shows that in all cases, the creation of radiation damage seems to reach a depth limit. To be precise, the creation of damage does not exceed a depth which is estimated to be 300 nm. Beyond this depth, no radiation damage is created. For the crystal irradiated with La and Ce ions, the distributions of RDA calculated are similar. As revealed on the figure 4-11.a, the creations of RDA both saturate at the same level, i.e 20 %. Distribution shows no dramatic increase of RDA even when the crystals are irradiated to very high fluence.

(iv) As when the crystal is implanted with Xe ions at very high fluence (corresponding to fraction of implanted Xe in the matrix of over 5 at. %), a striking behaviour is

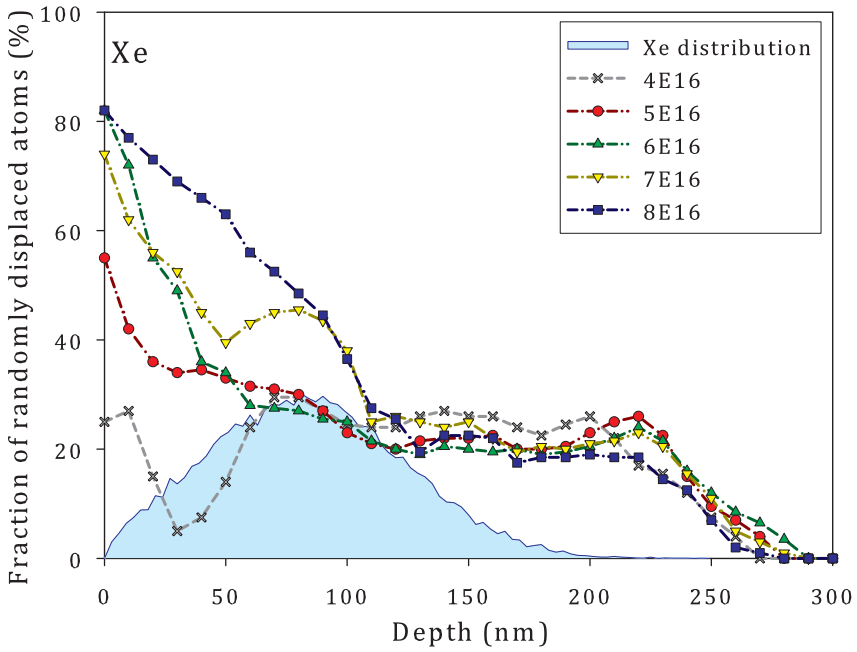

Figure 4-12: Distributions of RDA versus depth measured for $Xe-$ implanted UO_2 crystal at very high fluence (corresponding to over 5 at. % of implanted Xe in the matrix) derived from simulations. BC is parameterized by $L = 5\ nm$ and $\eta = 1.5°$. Fluences are measured in the unit of cm^{-2}. Xe implantation profile calculated by SRIM (represented by filled area) is plotted in arbitrary unit.

observed at the close surface layer. This phenomenon deserves a more detailed discussion. Figure 4-12 displays the depth-distribution of RDA extracted by MC simulation for $Xe-$implanted crystal up to very high concentration. As it can be observed from this figure, the distribution of RDA can be divided into two parts with respect to the maximum implanted range ($Rp + \Delta Rp \sim 120\ nm$) of Xe ions. On the deeper part, with corresponding depth $z > (Rp + \Delta Rp)$, the fraction of RDA stays constant with increasing ion fluence. The creation of RDA on this crystal's zone saturates at the same level that is observed for lower ion fluences, i.e around 25 %. On the contrary at the part located close to the surface of the crystal (with the corresponding depth $z < (Rp + \Delta Rp)$, a dramatic increase of RDA is observed for ion fluence of $\Phi \geq 4 \times 10^{14}\ cm^{-2}$ (which corresponds to the concentration of implanted Xe at maximum of ≥ 5 at. %). This dramatic increase in observed to be coincide with the implantation range of Xe in UO_2. It evolves literally towards the free surface of the crystal and reaches a very high fraction of RDA: up to 80 % for highest investigated fluence. Irradiation with insoluble Xe ions does lead to a distinguished behaviour of UO_2 crystalline structure as compared to soluble La or Ce ions.

4.3.3 Evolution of the bent channels defects

The distributions of BC versus depth have also been extracted from channelling data and MC simulation. Figure 4-9.b, figure 4-10.b and figure 4-11.b display the distribution of BC at the three ion ranges according to the previous classification of low, medium and high ion fluences. The BC has been extracted from channelling data recorded for crystal implanted with three different ions assuming that the BC is characterized by the same parameters ($L = 5\ nm$ and $\eta = 1.5°$).

(i) For the low ion fluence range, i.e. $\Phi \leq 1 \times 10^{15}\ cm^{-2}$ (see figure 4-9.b), the distribution of BC does not show any significant evolution even though the fraction of RDA increase regularly with increasing ion fluence. In fact, The fraction of BC increases by small steps with irradiation up to about 5 % observed at the fluence of $\Phi = 1 \times 10^{15}$ cm^{-2} while the RDA is estimated to reach 26 % for $Xe-$implanted crystal and 20 % for $La-$ and $Ce-$implanted crystals at this fluence. It can be thus concluded that over the low ion fluence range, the main class of defects that is formed due to irradiation is the RDA and only a minor fraction of BC is created. For irradiation with all three ions, the BC is created up to the thickness that is similar since the thickness of the damage zone is fixed to be identical for both RDA and BC (see section 4.1). Irradiation with low ion fluence range (that could be considered as the first step of irradiation) creates essentially point defect and defect clusters. BC is created with a low concentration only.

(ii) At the medium ion fluence range, where the maximum fraction of RDA does not vary with ion fluence but the thickness of the damage zone extended progressively towards greater depth (see figure 4-10.a), the fraction of BC is observed to dramatically increase in quantity and extend into the larger depth. As it can be seen on figure 4-10.b, a similar evolution of BC is observed for irradiation with all the three implanted ions irrespective to the nature of ions. The fraction of BC is observed to increase regularly from around 5 to $\sim$ 50 %, while the corresponding depth extends from 160 to 250 nm. It is more likely that the saturation of the RDA previously observed (see figure 4-10.a) is reached by the consequential transformation between two classes of defects. The creation of RDA up to a certain degree actually triggers the evolution of BC. When the saturation of RDA takes place, further irradiation lead to the creation of RDA that immediately transform into BC. BC appears to be as the second-step response on the evolution of the crystalline structure under irradiation, *a key feature of the evolution of the radiation damage in the crystal which remains totally unseen by the sole evolution of RDA.*

(iii) At high ion fluence range, when irradiation leads to the incorporation of the impurities to high concentration, the BC is observed to stay almost constant. As shown on figure 4-11.b, the fraction of BC is created around 80 %. In addition, the damage area

over which the BC is created remains almost constant at high ion fluence range. In all the three cases, the BC is created up to the thickness of about 260 to 300 nm. The almost constant BC fraction observed demonstrates that the creation of BC seems to saturate over the high ion fluence range. In fact, this phenomenon is not so surprising since the channelling of probing ion is known to be more sensitive to the low concentration than to the high concentration of defects. The presence of a higher concentration of defects might not necessarily results in the higher fraction of dechannelled ions as the crystal is already heavily damaged. For that reason, this phenomenon can be partially accounted for by the limited sensitivity of the analysing ion beam to the variation of damage at high concentration.

4.3.4 Choice of BC parameters, choice of L and η

By using a two-class model of defects, Monte-Carlo simulations have been successfully applied to reproduce channelling spectra recorded on different irradiated crystals over an extended range of fluence from $\Phi = 1 \times 10^{14}$ to 8×10^{16} cm^{-2} (see figures 4-6, 4-7 and 4-8). It is a great achievement for a simple model containing only two classes of defects. It is also important to note that in this investigation the characteristic length and angle of BC were reasonably chosen to be $L = 5$ nm and $\eta = 1.5°$ in accordance with values derived from TEM observations (see section 3.4). In fact, the definitive choice of L and η requires an in-depth examination of the channelling data, both recorded along axis and angular scan.

The choice of the values of these parameters (L, η) was tested against angular scans performed on the $Xe-$, $La-$ and $Ce-$implanted crystals recorded at several fluences. As a matter of fact, the reproduction by MC of the angular scans provides a very good test of the validity of both the two-defect model and of its parameters, since the constraints imposed by the reproduction is far more restricting in comparison to the reproduction of a single axial spectrum recorded in the main axis. Figure 4-13 displays an example of the experimentally measured angular scan and the corresponding results obtained by Monte-Carlo simulations for the $La-$implanted crystal at $\Phi = 2 \times 10^{16}$ cm^{-2}. This figure displays the experimental angular scans and the corresponding fits using the aforementioned model of defects in which the tilting angle was varied from $-3°$ to $3°$ across the main $\langle 100 \rangle$ axis. The dips are obtained over two different depth windows recorded on the U sub-lattice. The first dip is integrated in the depth windows from 40 to 130 nm below the crystal surface which corresponds to the sole backscattering signal on U sub-lattice on the damaged layer (i.e. without the contribution of impurities). The second one is integrated on the pristine part from 415 to 615 nm, i.e. on the dechannelling signal due to the backscattering on U sub-lattice.

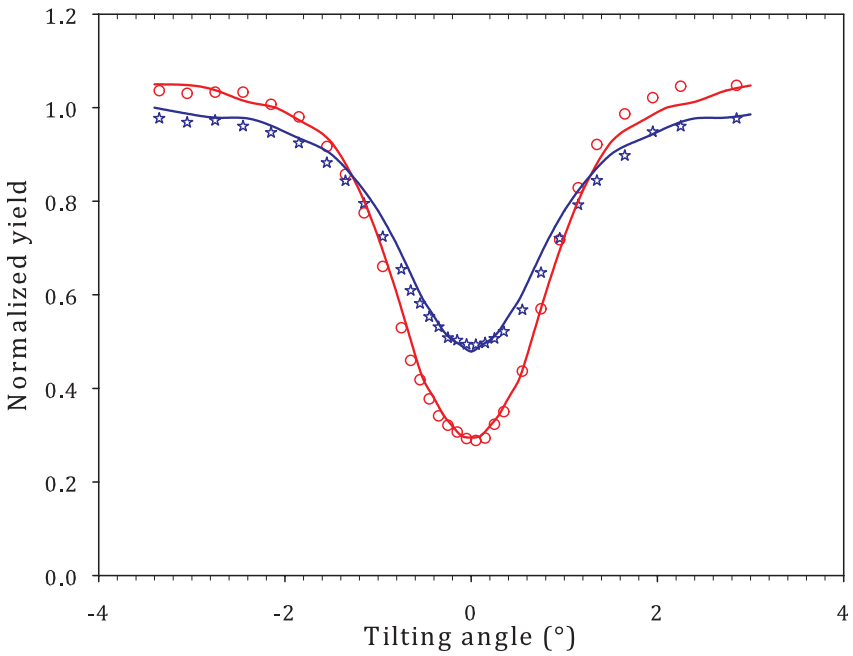

Figure 4-13: Experimental angular scans (symbols) recorded across the main ⟨100⟩ axis for UO_2 single crystal implanted with La ions at $\Phi = 2 \times 10^{16}\ cm^{-2}$. The yields are normalized to random yield. The angular scans are integrated from 40 to 130 nm (red circle) and from 415 to 615 nm (blue star). Solid lines are the corresponding Monte-Carlo simulations of angular scans. All the dips are reproduced by the two-class model of defects where BC was characterised by the length and angle of $L = 5\ nm$ and $\eta = 1.5°$, respectively.

As it can be seen, the bottom of the dip integrated from 40 to 130 nm, in comparison to the experimental data, was nicely fitted both the level and the width (i.e. the shape of the dips) supporting the idea that the model of defects used in this investigation together with the choice of L and η have totally accounted for the damage peak observed on the channelling spectra; a great achievement of the approach that was used to enlighten a new method to analysing channelling data.

Regarding the undamaged part of the crystal from 415 to 615 nm (corresponding to the energy window from 2370 to 2540 keV), the integration on this part of the channelling spectra have reproduced satisfactorily the level and the shape of the experimental dip. It is worth pointing out that the calculated width of the angular scan is fairly well simulated. However, the agreement is not as good as those obtained for the integration over the damage peak region. Angular scans recorded at lower fluence show a similar discrepancy but the difference is less. The limitation when fitting the angular scans might be necessary the use of other classes of defects along with the RDA and BC. These differences clearly point out the limitation of such an approach, where the two-class of defect model is supposed to reproduce all types of defects, from the low fluence range up to the highest one.

In summary, the two-class model of defects have been developed to analyse chan-

nelling data recorded on low-energy ion irradiated crystals. Such a model has been successfully applied with Monte-Carlo simulation to reproduce a large number of channelling spectra and angular scans recorded at various ion fluence for all crystals implanted with the three different ions. In this work, the length and angle of distortion were estimated based on analysis of HRTEM image (see figure 3-19) to be approximately $L = 5\ nm$ and $\eta = 1.5°$. The values used in this work have allowed a great success in analysing channelling data recorded for $Xe-$, $La-$ and $Ce-$ implanted crystals. Nevertheless, slight discrepancies still exist during analysis which would suggest a more complete model where other classes of defects (such as the polygonisation at high fluence) should be taken into consideration.

4.3.5 Estimation of uncertainties in the fraction of RDA and BC type defects

The channelling of ion (in case of well oriented along a crystallographic orientation of a crystal) depends strongly on the quality of the crystal. Every imperfection of the crystal results immediately in the dechannelling of ion thus increases the level of axial backscattering spectra recorded. In case of a crystal containing defects, the channelling of ion is affected by two way: the presence of defects leads to (i) direct obstruction or (ii) small angle scattering of channelled ion. However, the sensitivities of the direct obstruction and of the small angle scattering depend on the nature and concentration of defects in the crystal.

RDA refers to obstruction-type defects that directly results mostly in the direct backscattering of channelled ion. The backscattering of ion is so sensitive to the presence of RDA within the lattice that every small variation in the concentration of RDA will results immediately in the corresponding modification of the backscattering events. On the contrary, the presence of BC in the lattice, which refers to the distortion-type defects, affects the backscattering of ion in a different way. The backscattering of analysing beam is much more sensitive to the presence of BC at low concentration than at high concentration. As a consequence, a small variation at low concentration of BC leads to a more important modification of the backscattering event as compared to a larger variation at higher concentration.

Following these remarks, the uncertainties in the fraction of RDA and BC can be then specified. At first, the procedure used to fit a channelling spectrum described in section 4.2.4 is followed so as to obtain the best reproduction to the channelling spectra by simulation. Then in a second step, the uncertainties for RDA and BC can be specified as below:

- *Uncertainties for RDA:* To specify an uncertainty for RDA, the fraction of BC that

gives the best reproduction of axial channelling spectra was kept constant while the fraction of RDA was varied by small steps. In this case, a variation of 1 % of RDA can still give acceptable agreement between simulation and experimental channelling spectra. Any variation of larger than 1 % breaks this agreement since the backscattering of channelling ion is very sensitive to the concentration of RDA whether this concentration is low or high. Therefore, the errors bar for RDA was taken to be 1 % at all fluences.

- *Uncertainties for BC:* Conversely, in order to specify the error bar for BC, the fraction of RDA was kept constant while the constantly distributed fraction of BC was varied step by step. In this situation, the amount of BC variation that still gives an acceptable agreement between simulation and experimental channelling spectra depends on the concentration of BC. As the channelling of analysing ion is more sensitive to the low concentration of BC (at corresponding low ion fluence) than the higher concentration (at corresponding higher fluence), the uncertainty for BC varies from 0.1 % for low fluence to 5 % for high fluence, respectively. The exact value obtained varies, therefore, from fluence to fluence. For the sake of clarity, these values is displayed on the figure that shows the evolution of BC versus ion fluence (see figure 4-16).

4.3.6 Kinetics of damage accumulation

The kinetics of the created defects is established by following the evolutions of both RDA and BC defects are plotted. Figure 4-14 displays the evolution of the maximum fraction of RDA (i.e. recorded at the absolute maximum of the distribution at each ion fluence) and for the three studying cases as the function of the number of *dpa* and as the function of concentration of implanted species. All the evolutions of RDA induced in crystals implanted with Xe, La and Ce are plotted on the same figure in order to compare the radiation effects of ions of different nature and to compare the effects due to the incorporation of soluble versus insoluble species.

The evolutions of RDA show similar features that are observed on the evolutions of radiation damage extracted from channelling data by the TBA approach (see figure 3-10). That is to say, the evolutions of RDA reveal once again that: (i) a sharp increase step appears around 4 to 7 *dpa* (corresponding to the concentration of implanted ions of less than 0.1 at. %). This step is observed to appear at the same radiation condition regardless of the nature of ions. It is, therefore, a clear consequence due to the radiation effect (creation of defect due to nuclear stopping) and is totally independent of the nature of ions. (ii) After the steep increase, the creation of RDA saturates over a wide range of irradiation that is observed *via* the plateau of saturation from 10 to 300 *dpa*. In addition,

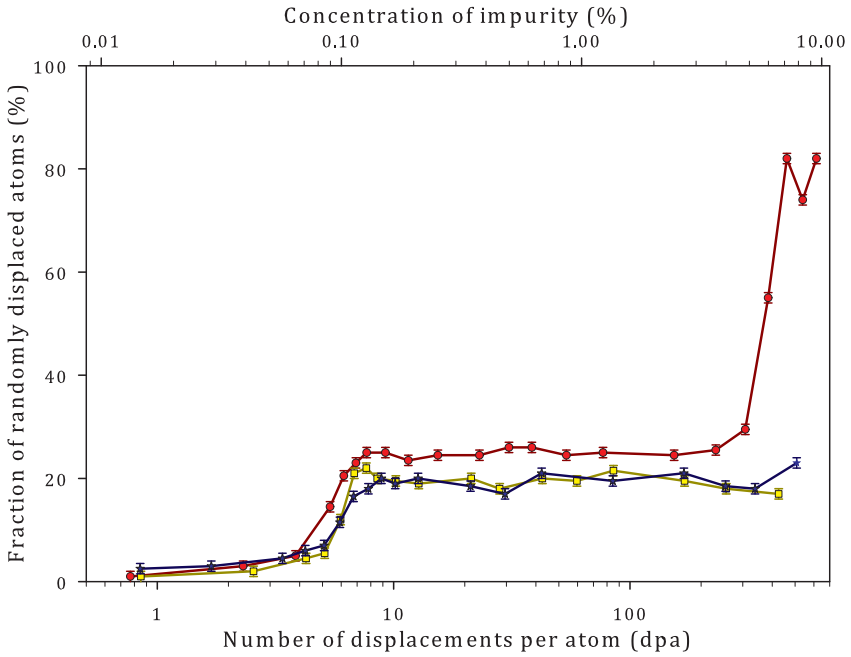

Figure 4-14: Evolutions of RDA extracted from channelling data by Monte-Carlo simulation for UO_2 crystals implanted with Xe (red circle), La (yellow square) and Ce (blue star) ions, respectively.

evolutions of RDA show the discrepancy due to the solubility (the gap observed between plateaus of saturation): the plateaus of saturation present a higher level ($\sim$ 25 %) for crystal irradiated with Xe ion than the crystal irradiated with La and Ce ion ($\sim$ 20 % and $\sim$ 19 % respectively). (iii) The second steep increase of the fraction of RDA is viewed only for crystal implanted with Xe ion to very high concentration, i.e., for irradiation condition that reaches over 200 *dpa* corresponding to the fraction of implanted Xe ions of higher than 5 % atomic. No second steep increase of RDA is observed for irradiation with La or Ce ions.

MSDA model

As to quantify the kinetic of damage creation under irradiation, evolutions of RDA can be fitted by the Multi-Steps Damage Accumulation model (MSDA) [116]. This model is based on the assumption that the damage accumulation process occurs *via* a series of structural transformations. Each step is described by a direct impact mechanism in which continuous irradiation results in the deposition of energy to the matrix hence cause the destabilization of the crystal at current structural state. The transformation of the irradiated material into a new structure is triggered by the destabilization of the current structural organization. That is to say, each new step occurs when the current structure of the irradiated material is destabilized by accumulated damage. The MSDA is the sum

of each individual step and can therefore be described by the following equation:

$$f_d = \sum_{i=1}^{m} \left(f_{d,i}^{sat} - f_{d,i-1}^{sat}\right) G\{1 - \exp\left[-\sigma_i \left(\Phi - \Phi_{i-1}\right)\right]\}$$

where f_d is the amount of accumulated damage; $f_{d,i}^{sat}$ is the level of damage at saturation at the step number i; σ_i is the cross section for the damage formation at the step i; Φ is the irradiated fluence; Φ_{i-1} is the value of accumulated fluence at which the step number i starts; G is a function that transforms negative values into 0 and leaves the positives unchanged; m represents the total number of individual steps.

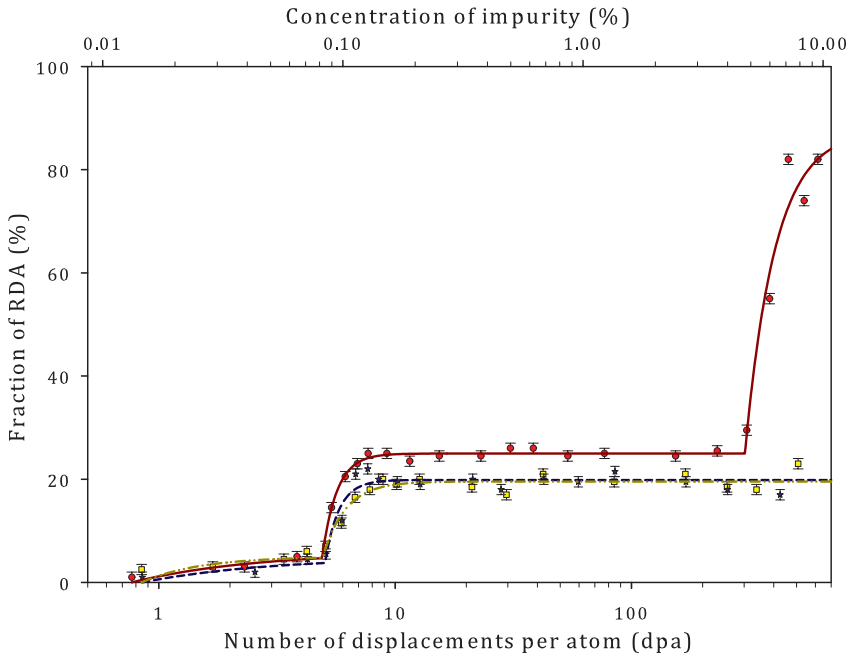

Figure 4-15: Fits to the evolution of RDA extracted from channelling spectra by MSDA model for UO_2 crystals irradiated with Xe (red circle), La (blue star) and Ce (yellow square). Solid, dashed and dash-dotted lines represent respectively the fits to the evolution of RDA.

Figure 4-15 depicts the fits to the evolutions of RDA performed in the framework of the MSDA model for all the three cases. The corresponding parameters that give the best fits are shown on table 4.1. For the crystal implanted with Xe ions, the evolution of the RDA in is fitted nicely by the MSDA model with three damage accumulation steps; the same feature that is observed on the evolution of radiation damage extracted by the TBA method. The first accumulation step is observed at low irradiated fluence. As observed on table 4.1, this accumulation step saturates at 6 % of RDA. The second damage accumulation step starts when the irradiation reaches 4.9 *dpa*. This step is characterized by the cross section of $\sigma_1 = (16 \pm 11)\ nm^2$ and by a fraction of RDA observed at the saturation of 25 %. The evolution of RDA passes to the final damage accumulation step when irradiation reaches 300 *dpa* ($\Phi = 4 \times 10^{16}\ cm^{-2}$). This step saturates at a high

fraction of RDA of 88 % and the characteristic cross section is observed to be $\sigma_2 = (8 \pm 2)$ nm^2.

As compared to the 3-step damage accumulation process in $Xe-$implanted crystal, the evolutions of RDA in $La-$ and $Ce-$irradiated crystals are fitted by the 2-step damage accumulation. As it can be seen on figure 4-15, the first damage accumulation step is observed on the same ion fluence range as compared with $Xe-$irradiated crystal. This step saturates at the fraction of RDA of 5 % for both $La-$ and $Ce-$implanted crystals. The second step begins essentially at the same irradiation condition (5 dpa) and saturates at similar level (19.9 % and 19.6 % respectively). It is evident that irradiations by soluble La and Ce ions lead to similar consequence while irradiation by soluble Xe ions leads to distinct effects compared to La and Ce ions: irradiations by soluble La and Ce ions do not lead to the third damage accumulation step.

	Fitted parameters	$Xe-$implanted crystal	$La-$implanted crystal	$Ce-$implanted crystal
Step 0	$f_{d,0}^{sat}(\%)$	6 ± 27	5 ± 17	5 ± 2
	$\Phi_0(dpa)$	0	0	0
	$\sigma_0(nm^2)$	2 ± 16	2 ± 11	4 ± 7
Step 1	$f_{d,1}^{sat}(\%)$	25 ± 1	19.9 ± 0.6	19.6 ± 0.6
	$\Phi_1(dpa)$	4.9 ± 0.3	5.0 ± 0.1	5.0 ± 0.1
	$\sigma_1(nm^2)$	16 ± 11	17 ± 5	10 ± 3
Step 2	$f_{d,2}^{sat}(\%)$	88 ± 6	–	–
	$\Phi_2(dpa)$	299 ± 1	–	–
	$\sigma_2(nm^2)$	8 ± 2	–	–

Table 4.1: Fits to the evolution of RDA by the MSDA model.

The evolution of the fraction of bent channels was also examined. The evolutions of BC exhibit a similar evolution for the three elements (see figure 4-16). At low fluence (before 7 dpa), the fraction of created BC is very small. Significant increase of BC is observed almost at the same irradiation condition for all the three case. BC starts to increase at about 7 dpa, i.e at higher ion fluence compared to the steep increase of RDA. Note that the fraction of BC at each fluence depends on the exact choice of length (L) and angle (η) of distortion (see section 4.3.4) but the evolution of BC, which reflects the effect of irradiation of the UO_2 structure, is independent of the choice of these parameters. That is to say, the three evolutions, in which the fraction of BC follows the similar evolution for all the three crystals, clearly demonstrate that irradiation has led to similar structural modifications.

At high implanted fluence, the creation of BC saturates. This saturation is observed in all three implanted crystals where the saturation level is observed to be higher in

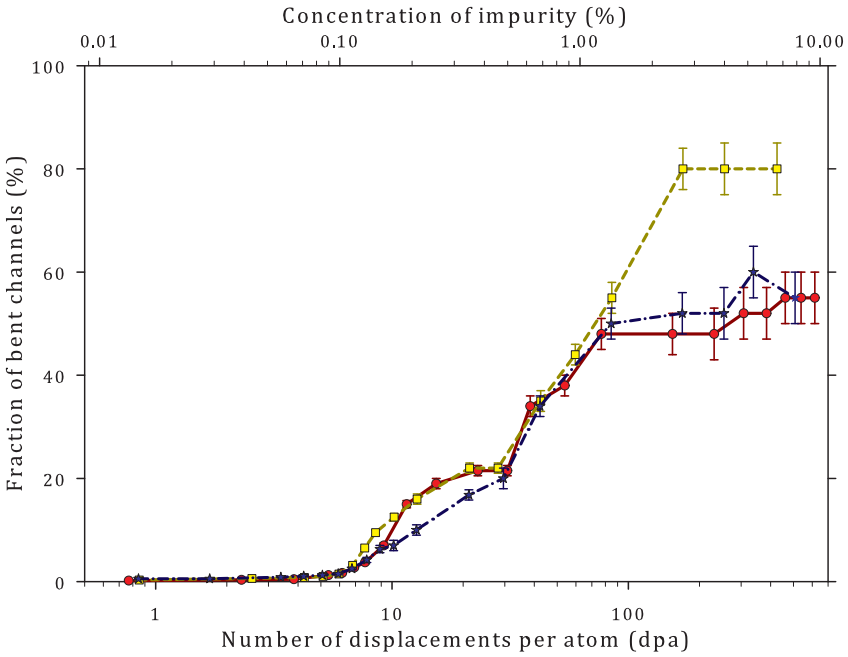

Figure 4-16: Evolutions of BC extracted from channelling data by Monte-Carlo simulation for UO_2 crystals implanted with Xe (red circle), La (yellow square) and Ce (blue star). Fits were performed assuming $L = 5\ nm$ and $\eta = 1.5°$.

$La-$ then in $Ce-$ and $Xe-$ implanted crystals. In fact, this difference is likely not as significant as it seems due to the following reason. Over this fluence range, the crystals were so heavily irradiated that the structural modification appears to be constant *via* the observation of BC. The fraction of the created defects reaches so high level that the indirect backscattering of channelled ions is almost insensible to a large variation of defects.

The comparison between RDA and BC shows that, the results reveal some following important features. First of all, the evolution of BC is shifted to larger fluence as compared to the steep increase of RDA observed at 4 to 7 *dpa*. This shift makes that the clear and significant increase of BC defect is observed when the saturation of RDA starts. The two phenomena, i.e. the saturation of RDA and the increase of BC, take place almost at the same irradiation condition (at about 7 *dpa*) and it indicates therefore that the processes of creation of BC and RDA are in fact strongly connected. The fraction of BC increases regularly with increasing ion fluence. At a given fluence, irradiation with Xe, La and Ce ion result in the similar fraction of BC. Discrepancy (the difference of fraction of BC) is observed only at the end of the evolution where the fraction of BC created reaches a high level (over 50 %). This discrepancy is more likely due to the relative insensibility of the analysing beam in a heavily damage crystal.

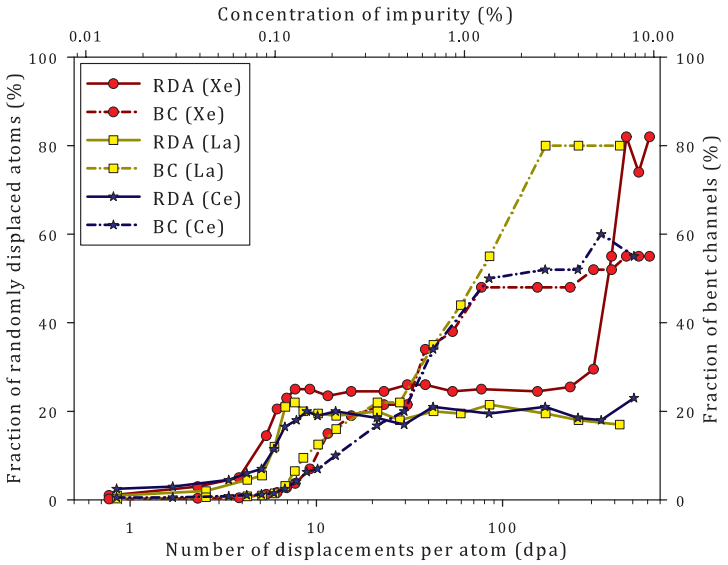

Figure 4-17: A comparison of the evolution of RDA and BC versus *dpa* and concentration. For the sake of clarity, the error bars are not shown on this figure.

4.4 General discussion

In the channelling analysis, the separation of the direct and indirect backscattering contribution (by the TBA method) gives the depth-distribution of the radiation damage in a crystal. However, the radiation damage extracted from channelling spectra is generally a mixture of many types of defects and it is quite impossible to distinguish and separate these classes of defects. Therefore the defects created are usually supposed to be of single type, RDA only. Since the separation of individual type of defects is impossible, the results may lead to a misunderstanding and/or to the incomplete knowledge regarding the radiation effects. For example, the evolution of radiation damage extracted form channelling spectra by the TBA method (see figure 3-10) clearly shows a steep increasing step around 4 to 7 *dpa*. After this step, the evolution of radiation damage saturates over a very wide range of irradiation (from 10 to 300 *dpa* for Xe irradiation and even larger for La and Ce irradiation). *It is seemingly that there is no modification of the crystalline structure over this range.* There might be some consequences due to irradiation on this range of ion fluence but it is in fact impossible to explore these consequences *via* the evolution of radiation damage extracted by the TBA approach.

Computer simulation offers the nice opportunity to allow such a separation of individual type of defects with an appropriate assumption, i.e with a relevant model of defects to be tested. Therefore, it might be possible to discover some modifications of the crystalline structure under irradiation which was hidden in the TBA analysis. As an attempt to analyse the channelling data with a new model of defect (in accordance with the obstruction and the distortion phenomena to the analysing beam), the channelling

data recorded for low-energy implanted UO_2 crystals have been analysed by Monte-Carlo simulations with the McChasy code using the two-class model of defects: (i) the randomly displaced atoms and (ii) the bent channels. The application of MC simulation into the channelling data analysis with the RDA and BC allows the user to take into account the presence of various classes of defects such as point defects, defect clusters, interstitials, stacking-faults, dislocations, dislocation loops, the presence of bubbles or precipitates and even the polygonisation. These defects give both contributions to the obstruction and distortion of the analysing beam which is eventually seen *via* the damage peak and the dechannelling signal. Such an obstructrion-type defects are most probably point defects, defect clusters, interstitials, stacking-faults, the presence of bubbles or precipitates and polygonisation while the distortion-type defects are dislocations, dislocation loops. As indicated in beginning of section 4.1, the presence of defects of any type in the matrix leads to the backscattering of analysing ion beam *via* direct backscattering and small angle scattering. Eventually, channelling spectra recorded is the consequence of the backscattering of probing ion that probes the defects as two main type: obstruction-type and distortion-type. Monte-Carlo simulation applied in this work enlightens a new method to analyse hence to extract more than one class of defects from channelling data. As an example, the RDA and BC have been extracted form channelling spectra recorded for crystals implanted with insoluble Xe and soluble La and Ce ions.

Let us start the discussion first with the model of defects itself. As used to analyse channelling data, the model of defects need to be consistent with the main features observed on channelling spectra. That is to say, since the damage peak and the dechannelling signal present as the two most important contributions of the channelling spectra (they reflect respectively the direct/indirect backscattering of analysing ion upon defected and matrix atoms), the choice of the model of defect containing the obstruction-type and the distortion-type defects is a good start that can allow the reproduction of both damage peak and dechannelling background. As there as many classes of defects are created during the irradiation process, it is possible (in principle) to assume as many classes of defect as we wanted in the simulation code but the eventual influence seen on channelling spectra is restricted to the obstruction and distortion influences. In addition, the use of many classes of defect is very complicated to interpret. A Two-class model of defects is therefore relevant and sufficient to enlighten a new approach.

The use of a model of defects containing the RDA and BC has clearly proved that it is totally possible to analyse channelling data by Monte-Carlo simulation to extract, afterwards, information regarding the radiation damage in the crystal including a profile of RDA (which reflects the local concentration of RDA at given depth) and a constant fraction of BC (that represents the modification of the crystalline structure). Channelling

spectra have been fitted satisfactorily up to the large depth using this model of defects (see figure 4-6, figure 4-7 and figure 4-8). Despite some discrepancy observed just after the damage peak for few fluence (see figure 4-6.c, figure 4-7.c and figure 4-8.c) where the underestimation of channelling spectra is observed around 2700 keV), the model of defect used in this work still succeeds in fitting most of the characteristic features of the channelling spectra and angular scans. This discrepancy is probably a limitation of the model of defects applied in this investigation; other classes of defects might be needed. It is also possible that since the BC is supposed to be constant over the whole damage region, the backscattering event drops down unexpectedly after the damage peak as the fraction of defect (more precisely the BC) goes suddenly down to 0. Likewise, the disagreement between simulation and experimental spectra observed at large depth (corresponding to the energy below 1000 keV) is due to the multiple scattering processes that were not taken into account in the computation program. However, these discrepancies do not limit any success of the channelling data analysis by Monte-Carlo simulation.

In the framework of this investigation, channelling data have been successfully analysed by Monte-Carlo simulations from which the distributions of RDA and BC versus depth and the consequential the kinetics of damage versus fluence are well extracted from channelling data. The results obtained can be summarised as follows.

(i) At low fluence range, a similar-to Gaussian-shaped distribution of RDA is created at the region that is similar to the ion implantation range. Regarding the creation of BC, the fraction of BC is created over the same area with respect to the RDA (as directly assumed by the model) and it is present with a low level. The two features demonstrate that the defects created are clearly due to the radiation effects *via* elastic nuclear interaction since the fraction of incorporated projectile is very small and hence their incorporation has a negligible effect on the process of damage formation in the crystal. Moreover, the similar depth observed for the distribution of defects and distribution of implanted ions (which is confirmed by TEM analysis, see section 3.4) indicates that the defects are created by the irradiation process is a clear fact. It is likely that irradiation at low fluence mainly creates point defects or more precisely Frenkel pair defect (pair of interstitial and vacancy) leading to the destabilization of the crystalline structure. Such a destabilisation has been observed *via* the buildup of strain/stress arising in the damaged layer (see section 3.3). The presence of RDA in interstitial position together with the presence of vacancies affects the regular arrangement of atoms in a row (modification of channels) that is eventually seen as the RDA and BC. It is worth stressing that the fraction of defect created at a given depth is essentially proportional to the concentration of implanted ions at that depth (similar position of the depth-distributions). It is also important to remind that due to the efficient reorganization of the crystalline structure (the annihilation of

Frenkel pair defect), we observed the residual effects as after annihilation atoms come back to regular lattice location and the modification is only affected by the creation RDA and vacancies.

Over this fluence range, irradiation is believed to created at first a small fraction of point defects. Afterwards, the accumulation of point defects transforms into the form of extended defects and/or defect clusters. The creation of point defects leads to the elastic deformation of the crystal and to the weak modification of the crystalline structure. This phenomenon is indirectly viewed *via* the presence of elastic strain arising in the damaged layer and *via* the very low level of BC (see figures 3-14.a and 4-9.b). Indeed, XRD measurement performed on $Ce-$implanted crystal over this fluence range reveals the presence of tensile elastic strain in the damaged layer. Such measurement is only possible for crystal submitted to elastic deformation, i.e, the distance between atomic planes was elongated but atoms still keep their strictly periodic arrangement. In case of crystal is plastically deformed, the use of an X-ray beam on the damaged layer never results in the constructive interference since there is no strict periodic arrangement of atoms. In this situation, the measurement of elastic strain is no longer possible.

In addition, as BC, which is characterised by the length (L) and the angle (η) of the distorted atomic arrangement, can be considered as extended defects in the crystal such as the formation of dislocations in the matrix. Indeed, the formation of a dislocations in the matrix consequently results in the bending of atomic rows around the dislocation edge. Since the presence of dislocation leads to the modification of not only one but several atomic arrangement surrounding (as observed on the FFT processed TEM image, see figure 3-19, where the presence of dislocation clearly leads to the modification of several atomic arrangements in the vicinity), it leads to the modification of atomic channels that eventually results in higher dechannelling signal of the channelling spectra. Such phenomenon is, to a large extent, similar to the presence of BC as the second class of defects or, conversely, the fraction of BC reflects the concentration of dislocations and/or network of tangled dislocations induced by irradiation. It reflects, therefore, a modification of the crystalline structure submitted to irradiation. This modification could be the gradual modification of the defective crystalline structure, which finishes by the formation of low angle boundary domain. A further step due to the radiation effects is possibly the sub-grains division process. Over this fluence range, the presence of BC at low concentration (see figure 3-9.b) reveals either that the modification of the crystalline structure is so weak that it simply leads to the elongation of distance between periodic atoms or that the BC measured over this fluence range is just a secondary effects of point defects that results in the small angle scattering of channelled ions. Both two assumptions were confirmed by the presence of elastic tensile strain measured by XRD analysis which

show that crystals were elastically deformed.

It is also at the low fluence range, the accumulation of point defects with increasing ion fluence lead to the transformation from point defects to extended defects. This phenomenon was observed *via* (i) the steep increase of RDA from 4 to 7 *dpa* and (ii) the relaxation of crystalline structure (observed *via* the strain/stress relief). The steep increase of RDA was observed to be independent to the nature of implanted ions.

(ii) In the medium fluence range, the accumulation of radiation effects results in significant destabilisation of the crystalline structure. Furthermore, the differences due to the irradiation of a soluble versus insoluble elements was seen. In general, the radiation damage effects over this fluence range reveal two important features.

As it can be observed *via* the distribution of defects versus depth (see figure 4-10), the creation of defects occurs at a larger depth as compared to the implantation range of ions. As increasing ion fluence, the profiles of defects literally shift towards greater depth and the damage zone broadens. This shift is observed on both two sides of the profiles of RDA, i.e. both on the shallower and the deeper part. More importantly, it extends to the depth that is much deeper with respect to the ions implantation profiles. This phenomenon is seemingly due to the diffusion of defects into the deeper layer. Such a process can be explained in the following two-stage process. In the early stage (i.e. at the corresponding low fluence range), the implanted and damage profiles are present under the Gaussian-shaped distributions which centre at the implantation range of 80 nm (see figure 4-9.a). The produced defects are present mainly as point defects as confirmed by XRD analysis. In the latter stage (at the medium fluence range), a high dose of irradiation results in significant accumulation of implanted ions and production of damage. The implanted ions and point defects produced by irradiation are mobile in collision cascades. The highly damaged zone initially develops near the implantation range and gradually grows deeper at higher fluence. The created damage finally reaches a saturation level and more defect diffuses through this damaged layer to grow new defects at deeper layer (see figure 4-10.a). This phenomenon seems to be due to the radiation-enhanced diffusion in the crystal. A high concentration of non-equilibrium point defects can readily annihilate within the irradiated region (saturation of defects) or diffuses out of the irradiated region and annihilates at sinks or form stable extended defect structures (expansion of damage zone). Only the inward fluxes of point defects were expected to contribute to the growth of defect structures beyond the irradiated region. Two factors could cause the inward flux including (a) the concentration of the generated point defects and (b) the strain/stress field induced by implanted ions and stabilized defects. Analysis by XRD technique presented in section 3.3 has confirmed the presence of the strain/stress in the damaged layer. This strain /stress field may provide a significant driving force for inward diffusion of point

defects into deeper depths. This atomistic mechanism was also reported for YSZ single crystal irradiated by $400-keV\ Xe$ ions where the damage layer was observed to extend to 160 nm well beyond the maximum irradiated depth of 110 nm below the crystal surface [40].

Over the medium fluence range the RDA saturates while the BC increase regularly. This feature was totally hidden according to the TBA approach since this approach assumes the presence of only randomly distributed atoms. *This feature reveals, therefore, an important structural modification under irradiation.* However, this phenomenon is not visible *via* the RDA as the fraction of RDA remains almost constant. More precisely, the creation of RDA reaches its limitation and therefore no further structural modification is observed. Conversely, the increase of the BC defects with increasing ion fluence is clearly seen. Irradiation agglomeration does not lead to the higher fraction of point defects but to the higher fraction of extended defects; a feature that reveals the structural modification due to irradiation. Such that structural modification can be mostly explained by the formation of dislocations at higher density that they finally aggregate to form a networks of tangled dislocations (extended defects). Worth mentioning is that the two phenomena (i.e. the saturation of RDA and the regular increase of BC) are observed to occur at the same irradiation condition ($\sim 7\ dpa$). It is a strong evidence confirming that when the ion fluence increases, the inward accumulation of point defects transforms into the extended defects which is finally observed *via* the increase of BC.

The extension of the damage region and the increase of BC (observed besides the saturation of RDA) can be considered as the second response of the UO_2 crystalline structure submitted to irradiation over the medium fluence range. In fact, at low fluence we observe the strain/stress build-up arising in the damage layer as a consequence of the creation of point defect. It is also at low fluence range we observed the transformation from point defects to extended defects (most probably defects clusters). After this first step, irradiation seems to not affect the UO_2 crystalline structure but evolution of BC defect shows that UO_2 crystalline structure undergoes dramatic transformation that could weaken its stability. Such that transformation from RDA to BC can be considered as the second response of UO_2 crystalline structure under irradiation.

As indicated in section 4.3.6, the fraction of RDA observed at saturation plateaus (i.e. over the medium fluence range) due to insoluble versus soluble species is clearly different. Insoluble Xe ion results in higher level whilst soluble La and Ce ions both result in the same lower saturation plateaus. The difference of plateaus of saturation can be mostly explained by the size and the solubility of implanted species. Being an inert noble gas, the size of atomic Xe atoms is much higher as compared to La and Ce atoms in the matrix. Inert Xe does not form any compound with UO_2 while La and Ce (that

are totally soluble in UO_2) form compound with UO_2 at the possible charge state of +3 for La and +3 or +4 for Ce. However, due to the charge compensation, Ce has probably the charge state of +3 in UO_2. The radius of inert Xe atom is $r_{Xe} = 218\ pm$ while the radii of La and Ce at charge state +3 are $r_{La} = 117\ pm$ and $r_{Ce} = 115\ pm$, respectively [117]. Compared to the radius of U in the crystal ($r_U = 97\ pm$), the radius of Xe is greater than twice the radius of U while the radii of La or Ce in compound is totally comparable to that of U. It is clear that Xe creates a higher stress field than La or Ce. It can affect the position of all surrounding atoms and pushes them into the location where they appear as an obstruction to the analysing beam. As a consequence, the fraction of defects created is higher as compared to La or Ce ions.

A second mechanism may explain the observed difference in the saturation plateaus: since Xe is present as an insoluble species in UO_2 matrix, Xe ions tend to gather together forming nano-size bubbles. Such a presence of Xe bubbles in UO_2 matrix was clearly reported [70, 77, 78, 79, 118, 119, 120] while La and Ce are totally soluble in UO_2. They can form solid solution with UO_2 up to high concentration (up to 80 %) [103, 121, 122, 123, 124, 125, 126], and stay most probably in substitutional or empty octahedral positions matrix [127, 128]. Indeed, Monte-Carlo simulations with McChasy program performed along the main $\langle 100 \rangle$ type axis assuming that implanted species are located in substitutional and octahedral positions in UO_2 matrix reveal no difference. Therefore, the position of implanted species does not seem to explain the difference of the fraction of RDA observed on the satuation plateaus.

As Xe ions form bubbles in UO_2 matrix, they create a much stronger stress field in UO_2 crystalline structure. On the contrary, La and Ce stay most probably as individual impurities in substitutional or octahedral position (since there are 4 octahedral positions are available in a UO_2 basic cell structure), they create a much weaker stress field in UO_2. The fact that UO_2 can accommodate La and Ce in substitutional and empty octahedral positions to a large concentration somehow eliminates the formation of precipitates and hence diminishes to the large extent the stress field arising in the crystal. Such a situation is not the case in Xe-implanted crystal where Xe does not form any compound with UO_2 and thus sticks together in the form of nano-size bubbles. The presence of nano-size bubbles affects the process of damage creation twofold. They limit on one hand the annihilation of point defect and vacancy during a collision cascade and create on the other hand a very strong stress field that leads to the creation of supplement defects in the crystal. Taking into account the size and the formation of Xe bubbles in the crystal as compared to La and Ce ions, the difference in saturation plateaus can be explained by the solubility of implanted species. In practice, it would have been nice to be able to locate Xe, La and Ce in UO_2 to verify this assumption but it is impossible to perform

by channelling technique, since U atoms are too heavy compared to Xe, La and Ce.

(iii) In the high fluence range, irradiation with Xe leads to the dramatically creation of RDA as Xe ions are incorporated at high concentration (over 5 at. %).It is seemingly that starting from the fluence of $\Phi = 4 \times 10^{16}\ cm^{-2}$, the incorporation of Xe at high concentration leads likely to the formation of Xe bubbles of larger size. The impact of Xe bubbles becomes so strong that they lead to the frustration of the UO_2 crystalline structure, known as the polygonisation of UO_2 single crystal, which is the origin of the dramatically increase of RDA at the surface. It is worth recalling that the dramatically increase of RDA is solely observed on this part (from the surface to 120 nm correspond to $Rp + \Delta Rp$ of Xe implantation profile) where the large fraction of Xe is present. While on the deeper part, which is located beyond the maximum implantation range of Xe, the implanted Xe ion is always present at low concentration. Therefore, the radiation damage on the deeper part (deeper than the depth $z > Rp + \Delta Rp$) remains essentially unchanged; no dramatically increase of RDA is observed. It is undoubtedly that this frustration occurs on the area of the highest concentration of Xe and evolves towards the free surface not to the constrained part (which is attached to the thick underlying substrate). The dramatic damage creation of RDA observed at the close surface is obviously the consequence of the incorporation of a non soluble atom of larger size in the crystal at very high concentration. At the highest implanted fluence ($\Phi = 8 \times 10^{16}\ cm^{-2}$) the maximum fraction of RDA created reaches 80 % which is much higher compared to the saturation plateau observe on the medium fluence range but it is lower compared to the maximum damage fraction extracted from the channelling spectrum by the TBA approach, i.e. at almost 100 %. This fact indicates that the defects created in UO_2 crystal irradiated at very high fluence are actually a mixture of complex defects and that UO_2 crystal implanted with Xe to very high concentration still remains the crystalline structure. It is similar to the situation where the crystalline structure becomes structure with small domains that slightly miss-oriented one with respect to each other by small angle; it was never amorphised as the case of swift heavy ion irradiation in UO_2.

Over this fluence range, the creation of BC seems to reaches the limitation as observed *via* the constant fractions (see figure 4-16). Such a phenomenon was observed in the three cases. It is seemingly that the crystals were so heavily irradiated that the structural modification appears to be constant. It is also possible that since the fraction of the created defects reaches so high level that their variation leads to negligible influences on the small angle scattering of channelling ions. As a consequence, the fraction of BC, which reflects essentially the indirect backscattering of channelled ions, remains constant.

To summarise, channelling data recorded for UO_2 crystals implanted with low-energy ions have been analysed in much more details with an advanced method. Such a method

is based on the application of Monte-Carlo simulation using a two-class defect model comprising the randomly displaced atoms and the bent channels. In the framework of this investigation, the new advanced approach has been successfully applied to the analysis of a large number of channelling data recorded for UO_2 crystals implanted with different ions. Along with the similar results (similar to that obtained by the TBA approach), the new method has helped exploring important information regarding the radiation effects which was totally hidden in the analysis by TBA method. Despite some limitations of the model of defects, *the new method developed in this work is very promising and can be applied to the analysis of channelling data recorded for low-energy ion irradiated crystal.*

Channelling data analysis by Monte-Carlo simulation can be further improved in several ways, both experimentally or theoretically.

From the experimental point of view, the channelling measurement using an analysing beam at various energies can be performed on the defective crystals to test the energy-dependence of the spectra recorded in the channelling axis at selected fluence. In such an experiment, the backscattering of the analysing beam on different types of defects will be a crucial evidence to determine the nature of defects. Similarly, angular scans performed on selected fluence with an analysing beam at different energies will gives a more decisive conclusion on the exact nature of defects. As a matter of fact, defects cross-sections exhibit a different behaviour depending on the exact nature of defect; for instance, the dechannelling cross section for point defects decreases with the analysing beam energy, while constrained regions leads to an increase of the cross section. Though these experiments were performed in the past for simple systems, involving one defect type only, their extensions to complex irradiated systems would require the need of a large number of beam-time day and a full analysis by Monte-Carlo simulation. An "Energy-dependence" experiment of channelling technique could be therefore a crucial key in order to analyse channelling data by Monte-Carlo simulation at a better level.

On a theoretical point of view, a better channelling data analysis by Monte-Carlo simulation can be improved by testing a more complex model of defects. For instance, a model comprising the polygonisation along with the RDA and BC could be worth tested. In this situation, a more realistic model of defect could allow a better reproduction of the channelling data, thus better interpretation. On the contrary, a more realistic defective crystalline structure can be assumed to take into account a true defective structure. For example, a new structure in which the true form of a dislocation can be incorporated can be tested. This possibility allows to take into account both the presence of the dislocation edge and of the distortion of the surrounding atomic arrangements. In another possibility, a more complex structure which assumes the incorporation of impurities under the form of precipitates or bubbles would be worth tested, especially for crystals implanted at

high concentration of impurities. Recently, A new version of the McChasy Monte-Carlo computational program is being developed to take into account the presence of the realistic dislocation. This version will be tested against an experimental data in the future.

Conclusions and perspectives

This PhD thesis has been focused on studying the behaviour of uranium dioxide single crystals submitted to low-energy ion irradiation. For this purpose, a literature review was given on the behaviour of ceramics materials in general and uranium dioxide in particular. From the bibliographical review, it is found that uranium dioxide is radiation tolerant; amorphisation was never reported. However, a full knowledge of the mechanisms of radiation damage remains unclear in particular the knowledge of the behaviour of uranium dioxide due to the irradiations with soluble versus insoluble elements. To our knowledge, the problem of doping in UO_2 by a soluble versus insoluble elements to high concentration was never explored before. As in a real situation, the fuel is literally poisoned by a mixture of all possible fission products, such an investigation of the behaviour due to individual species is necessary for a full understanding. For these reasons, a series of *in situ* experiments was performed to investigate the radiation damage effects in uranium dioxide single crystal submitted to external irradiation of well-defined condition. Low-energy irradiations were used for studying the behaviour of uranium dioxide crystal due to (i) radiation effect and (ii) effects due to the doping to high concentration of a soluble versus insoluble elements at normal temperature condition. Due to their importance in the nuclear fuel - since their abundance as fission products is high - Xe, La and Ce with similar masses were chosen.

The experiments were designed to apply the ion implantation technique to induce damage in the crystalline structure of UO_2. The creation of defects was monitored principally with the ion channelling technique. Channelling data recorded were first analysed by the Two-Beam approximation which can gives a reasonably accurate information regarding the damage creation. Monte-Carlo simulation with McChasy computer program that allows the simulation of the channelling phenomenon of ion in a crystalline structured material was applied afterwards for a thorough analysis of the experimental data. With the Monte-Carlo simulation, channelling data were analysed in much more details with a model of defects comprising the Randomly Displaced Atom (RDA) and the Bent Channels (BC). The RDA and BC are supposed to model, in a first approach, many classes of actual defects including point defects, extended defects such as defects clusters or dislocations and even the polygonisation of the solid. The results obtained can be summarised as below:

- At very low ion fluence ($\Phi \leq 7 \times 10^{14}$ cm^{-2} corresponding to a dose less than 5.9 *dpa*), irradiation leads to the elastic deformation of the crystal. The main type

of defect induced is point defects and their presence at low dimension results in the strain/stress build-up in the crystal. The damage layer exhibits a tensile strain along the direction normal to the surface of the crystal. The crystal's relaxation takes place when the irradiation exceeds 5.9 *dpa*. A partial strain/stress relief is observed. At this stage, there is a transformation from point defects to extended defects in the crystal.

- After the relaxation the radiation damage increases rapidly. This steep increase of is observed at the fluence range between 4 to 7 *dpa* regardless of the nature of ions. This fluence range corresponds to the very small fraction of implanted ions of less than 0.1 at. % which is too small to play any important role due to the nature of ions. Therefore, the steep increase of defects clearly demonstrates that the radiation damage is due to elastic nuclear collision in the crystal, leading to collision cascades.

- The saturation of RDA is observed over a wide range (from 10 to 300 *dpa*) of irradiation for all three crystals. It is at this stage a clear difference due to irradiations by soluble versus insoluble ions was revealed. Insoluble species results in higher fraction of defects (higher saturation plateau) as compared to soluble species. The difference is believed to be due to the solubilities of implanted species. Soluble La and Ce species form solid solution with UO_2 and locate most probably at substitutional or octahedral positions. Because UO_2 can accommodate a large fraction of these elements in its structure (up to 80 %) and because their radii in solid solution form (i.e. at corresponding charge state of +3 for both species) are totally comparable to the radius of U^{+4}, the consequential stress field arising from their presence in the crystal is much smaller as compared to the presence of insoluble Xe in the matrix. Since the radius of insoluble Xe is almost twice the radius of U^{+4} and that Xe tends to accumulate together forming nanometre-size bubbles in the matrix, they create a higher stress field and thus higher fraction of defects in the UO_2 single crystal.

- Significant structural modification is observed in correlation with the saturation of randomly distributed defects (RDA) observed on the saturation plateaus. As revealed by Monte-Carlo analysis, the significant structural modification (observed via the regular increase of BC) occurred at the same fluence ($\sim$ 7 *dpa*) where the saturation of RDA took place. At this stage, the inward accumulation of RDA seems to transform into other classes of defects which modifies the crystalline structure. The steep increase of RDA can be considered as the first-step response of the UO_2 crystalline structure submitted to irradiation while such evolution of BC can be considered as the next-step response. A more complete picture on the behaviour of UO_2 single crystal is revealed considering the BC. Such that feature was totally hidden based on the sole observation of the saturation plateaus of RDA.

- When the crystals are implanted to very high fluence (corresponding to the concentration of implanted ions of over 5 at. %), distinct behaviours were observed between crystals implanted with soluble versus insoluble elements. The fraction of RDA induced by soluble La and Ce ions stays almost unchanged. The saturation plateaus of RDA are still observed. On the contrary, the dramatical increase of RDA is observed in the crystal implanted with insoluble Xe ions. The fraction of RDA observed at highest fluence reaches 80 %, far larger compared to the saturation plateau. This huge increase of RDA is due to the formation of Xe bubbles of larger than nanometre-size in crystal which eventually leads to the frustration of the crystal. Likewise, the BC is observed to be unchanged in all three case, the feature that reveal either the saturation of structural modification and the good resistance to irradiation of UO_2 crystalline structure.

This work opens several questions to be answered. Each and everyone of them could figure as an interesting reseach topic.

First of all, a characterisation of the defect by ion channelling technique at various energies for the crystals irradiated at selected fluences should be performed. Angular scans will be very useful for a more detailed investigation. According to the classified ion fluence ranges, the angular scan can be performed (i) at low fluence range for instance at $\Phi = 5 \times 10^{14}\ cm^{-2}$) where the elastic deformation of the crystal is observed and at and $\Phi = 7 \times 10^{14}\ cm^{-2}$) where the steep increase of RDA is observed, (ii) at medium fluence range where the saturation of RDA and the regular increase of BC are visible (for instance at $\Phi = 2 \times 10^{15}$ and $\Phi = 5 \times 10^{15}\ cm^{-2}$) and (iii) at high fluence range, say $\Phi = 2 \times 10^{16}$ and $\Phi = 5 \times 10^{16}\ cm^{-2}$, where the dramatical increase of RDA in the $Xe-$implanted crystal takes place. Such that angular scans by ion channelling technique at various energies (at indicated fluences) will allow a more detailed access to the radiation damage, particularly to the true nature of RDA and BC assuming a complete simulation of the data by Monte-Carlo.

Secondly, a better description of radiation-induced defects created by ion irradiation should be performed. The two-type defect model developed in this thesis is only a first step towards this description. The description of a realistic model for dislocation, involving dislocation core and distorted row is currently being developed at Warsaw. In a similar spirit, the description of a heterogeneous system, precipitates or gas bubbles embedded into a crystalline structure, would be a good model system to obtain a better description of the evolution of the irradiated crystal at high fluence.

Last but not least, in a real situation the nuclear fuel is bombarded by fission fragments at operating temperature. Therefore, the behaviour of the fuel is different due

to the high mobility of defects and implanted ions. Two major features can be predicted at high temperature concerning (i) the high mobility of atoms which enhances the Frenkel pair annihilation during a collision cascade and eventually reduces to large extent the creation of defects and (ii) the high mobility of implanted ions (especially of insoluble species) which is supposed to lead to the formation of precipitates or inert gas bubbles at lower fluence. This question figure as a very interesting research topic. For example, a research topic could be dedicated to the investigation of the radiation effects in UO_2 single crystals at high temperature, say 500℃, where the formation of the RIM effect at the periphery of the fuel is observed. This investigation would be event more interesting in the framework of an *in situ* experiment where the crystal can be alternatively irradiated and characterised by ion channelling technique at high temperature. The coupling of the implantation and characterisation lines at the JANNuS Orsay facility will be available in the near future where such investigation could be realised.

List of Figures

1-1 Uranium dioxide crystal with uranium atoms located at fcc positions (black) and oxygen atoms located at tetrahedral positions (red). 11

1-2 Equilibrium diagram of zirconia [14]. 13

1-3 Schematic drawing of the two-bodies elastic collision. 15

1-4 Maximum energy transferred versus m_1/m_2. 17

1-5 Stopping power of Cerium ions in UO_2 calculated according to the SRIM code. . 20

1-6 Damage accumulation recorded in $FSZs$ [39]. 27

1-7 Damage accumulation in YSZ measured by RBS/C at irradiated temperature of 303 and 183 K [40]. 28

1-8 Typical images of ion tracks in UO_2 under irradiation with 210 MeV Xe^{14+} ions to fluence of 5×10^{11} cm^{-2} at room temperature [69]. 35

1-9 Calculated evolution of the UO_2 radial temperature distribution along a track in UO_2 as a function of time. The calculations are for 11.4 MeV/u U ions in the first nm of the target, i.e. $dE/dx = 60$ keV/nm with $\lambda = 6$ nm and a melting temperature of $Tm = 3150$ K [35]. 37

1-10 Molecular dynamic simulation of displacement cascade induced by $80 - keV$ U ion irradiated in UO_2 at two different times: (a) at 2.15 ps after injection and (b) at 20 ps corresponding to the very end of the cascade [76]. 38

2-1 JANNuS nuclear facility, located at Orsay and managed by the **"Centre de Sciences Nucléaire et de Sciences de la Matière" (CSNSM)**, belongs to CNRS-IN2P3-Université Paris-Sud. It couples a 2 MV Tandem accelerator (ARAMIS) and a 190 kV ion implanter (IRMA) to a 200 kV Transmission Electron Microscope (TEM FEI Tecnai G^2 20). 43

2-2 RBS geometry 45

2-3 Sketch of channelling phenomenon 46

2-4 Typical channelling spectrum recorded on a crystal containing defects in a region of the crystal (red). Blue line represents the random spectrum and the green line represents the channelling spectrum recorded for perfect crystal. 47

2-5 Derivation of the Laue diffraction condition 50

2-6 Construction of the Ewald's Sphere 51

2-7 Schematic diagram of a High Resolution Transmission Electron Microscope. . . 55

3-1 Typical (a and b) and high-energy part (c and d) of RBS/C spectra recorded in random (full circle) and $\langle 100 \rangle -$aligned directions (empty circle) on un-implanted and implanted UO_2 crystal with $470 - keV\ Xe$ ions. Fluences are measured in unit of cm^{-2}. 60

3-2 Typical example of a decomposition of channelling spectrum applying the TBA approach (a) and the corresponding distribution of defects versus depth (b). The channelling spectrum is fitted with three components: the dechannelling signal (red long-dashed), the Gaussian-shaped surface peak (pink short-dashed) and the Gaussian-shaped damage peak (blue dash-dotted). 63

3-3 Decomposition of a channelling spectrum recorded at high implanted fluence taking into account the contribution of implanted impurities (indicated on figure a) and the corresponding distribution of defects versus depth (b). 64

3-4 Distribution of randomly displaced atoms versus depth for (a) low, (b) medium and (c) high fluence ranges. Depth distribution were extracted from analysis of channelling spectra using the two-beam approximation method. Fluences are expressed in unit of cm^{-2}. Filled area represents the distribution of implanted Xe calculated by the SRIM calculation code (in arbitrary unit). 65

3-5 Evolution of the fraction of randomly displaced atoms calculated at the maximum of the profile damage accumulation in the UO_2 single crystal as a function of ion fluence. 66

3-6 Channelling spectra (a and b) and high energy part of channelling spectra (c and d) recorded for UO_2 crystals irradiated with La ions. Fluences are measured in unit of cm^{-2}. 68

3-7 Distributions of the defects versus the depth extracted (using the same TBA method discussed here before) for UO_2 crystals implanted with La ions. Fluences are expressed in unit of cm^{-2}. The distribution of La (filled area) calculated by SRIM program is plotted in arbitrary unit. 69

3-8 Channelling spectra (a and b) and high energy part of channelling spectra (c and d) recorded for UO_2 crystals irradiated with Ce ions. Fluences are measured in unit of cm^{-2}. 70

3-9 Distributions of the defects versus the depth extracted (using the same TBA method discussed here before) for UO_2 crystals implanted with Ce ions. Fluences are expressed in unit of cm^{-2}. The distribution of Ce (filled area) calculated by SRIM program is plotted in arbitrary unit. 71

3-10 Evolution of the damage accumulation (fraction of randomly displaced atoms at maximum) in crystals implanted with $470 - keV\ Xe$ (red circle), $500 - keV\ La$ (blue star) and $500 - keV\ Ce$ (green square) as a function of the number of *dpa* as well as a function of the maximum concentration of implanted species. 72

3-11 $\theta-2\theta$ experimental scan recorded around the (400) Bragg reflection for $\langle 100\rangle-$oriented UO_2 crystals implanted to indicated fluences. The arrows indicate the last peak arising from the maximum strain value exhibited by the damaged layer. 73

3-12 $\theta - 2\theta$ experimental scan around the (222) atomic planes for $\langle 111\rangle-$oriented UO_2 crystals implanted to indicated fluences. The arrows indicate the last peak arising from the maximum strain value exhibited by the damaged layer. 74

3-13 Evolution of the maximum total strain as a function of implantion fluence for $\langle 100\rangle-$ and $\langle 111\rangle-$oriented crystals. 75

3-14 Evolution of the maximum elastic normal strain (a) and the maximum in-plane fixation stress (b) as a function of implantation dose expressed in *dpa* for both $\langle 100\rangle-$ and $\langle 111\rangle-$oriented UO_2 crystals implanted with Ce ions. The evolutions of damage fraction measured by RBS/C technique are also plotted (c). 78

3-15 Plan view image of a UO_2 single crystal irradiated with $500 - keV\ Ce$ ions, at a fluence of $5 \times 10^{14}\ cm^{-2}$. Dislocations loops are marked with arrows. The white arrows show two linked dislocations. 81

3-16 Plan view image of a UO_2 single crystal irradiated with $500 - keV\ Ce$ ions, at a fluence of $5 \times 10^{14}\ cm^{-2}$; Projectile impact, close to the surface of the specimen, and associated SAD pattern. The zone axis is of $\langle 100\rangle$ type, as attested by the four-fold symmetry of the diffraction pattern. 81

3-17 Cross-section image of a UO_2 single crystal irradiated with $500 - keV\ Ce$ ions, at a fluence of $5 \times 10^{14}\ cm^{-2}$. Figure (b) is displayed as rotating 180° from figure (a) for easy following. 82

3-18 Cross-section image of a UO_2 single crystal irradiated with $500 - keV\ Ce$ ions, at a fluence of $5 \times 10^{14}\ cm^{-2}$. Enlarged view (a) on the top of the composite image (upper region marked as (1) with a rectangle in figure 3-17b) and (b) in the middle of the composite image (lower region marked as (2) with a rectangle in figure 3-17b). The black arrows in figure (b) indicate selected dislocation loops lying in the (111) planes. 83

3-19 Processed image, filtered FFT and the corresponding power spectrum of UO_2 single crystal irradiated with $500 - keV\ Ce$ ions, at a fluence of $5 \times 10^{14}\ cm^{-2}$ and associated SAD pattern. The white arrows indicate selected dislocation edges. 84

4-1 A simplified model of defects: a profile of RDA defects (blue) and a constant fraction of BC defects (red) are incorporated on the damaged layer. 89

4-2 A schematic representation of bent channel defect characterised by the length (L) and the angle (η) of the distortion with respect to the channel direction. . . 90

4-3 Fits to channelling spectra (b and d) assuming that RDA distributions are the sole type of defects (a and c). The red solid lines denotes the distribution of RDA (in figure (a), indicated in the legend as TBA) (see chapter 3) and the corresponding spectrum obtained from simulation (in figure (b)) with the profile of defects derived from the TBA. Long-dashed green lines denote distribution of RDA (in figure (a) and (c), indicated in the legend as RDA) that allows reproducing the damage peak and the corresponding spectrum (figure (b) and (d)). Short-dashed blue lines represent the distribution of RDA (indicated in the legend as extended RDA) that allows fitting the entire spectrum over the whole energy range of backscattered ions. 92

4-4 Fit to channelling spectrum assuming the sole presence of bent channels as radiation-induced defects ($L = 5\ nm$ and $\eta = 1.5°$). The red solid line denotes the simulated spectrum and the corresponding distribution of BC assuming both the depth distribution and the concentration derived from the TBA. Long-dashed green line denotes the simulated spectrum and the corresponding sharp distribution of BC (up to 95 % of BC). Short-dashed blue line represents the calculated spectrum assuming a constant distribution of BC from the surface up to a given depth. Dotted line help showing that the sharp distribution of BC is centred at the ion's implanted range. 94

4-5 Examples showing the influence of (a) the length L and (b) the angle η of distorted channels to the simulated channelling spectra. The distribution of RDA and the constant distribution of BC are fixed according to the best fit which is obtained for $L = 5\ nm$ and $\eta = 1.5°$. 97

4-6 Best MC simulations to RBS/C spectra recorded for $Xe-$implanted crystal in random condition (dashed line) and in axial aligned condition for virgin (dotted) and UO_2 implanted crystal (solid line). Experimental channelling spectra are plotted in symbols and the fluences are expressed in unit of cm^{-2}. (c) and (d) are zooms in the surface region of figure (a) and (b). Fits were performed assuming $L = 5\ nm$ and $\eta = 1.5°$. 99

4-7 Best MC simulations to RBS/C spectra recorded for La-implanted UO_2 crystal at low (a) and high (b) fluences. The zooms on high energy part are shown on figure (c) and (d) respectively. Dashed and dotted lines denote the best MC simulations to random and axial virgin spectra. Solid lines denote best fits to axial aligned spectra recorded for irradiated crystal. Experimental channelling spectra are plotted in symbols for fluences of $\Phi = 3 \times 10^{14}\ cm^{-2}$ (red circle), $7 \times 10^{14}\ cm^{-2}$ (green triangle up), $8 \times 10^{14}\ cm^{-2}$ (yellow triangle down), $1 \times 10^{15}\ cm^{-2}$ (violet square), $2.5 \times 10^{15}\ cm^{-2}$ (pink diamond), $5 \times 10^{15}\ cm^{-2}$ (cyan hexagon), $1 \times 10^{16}\ cm^{-2}$ (gray star), $2 \times 10^{16}\ cm^{-2}$ (orange cross) and $3 \times 10^{16}\ cm^{-2}$ (red crossed-circle). Fits were performed assuming $L = 5\ nm$ and $\eta = 1.5°$. 100

4-8 Best MC simulations to RBS/C spectra recorded for Ce-implanted UO_2 crystal at low (a) and high (b) fluences. The zooms on high energy part are shown on figure (c) and (d) respectively. Dashed lines and dotted lines denote the best fits to random and axial virgin spectra. Solid lines denote best MC simulations to axial aligned spectra recorded for irradiated crystal. Experimental channelling spectra are plotted in symbols for fluences of $\Phi = 2 \times 10^{14}\ cm^{-2}$ (red circle), $7 \times 10^{14}\ cm^{-2}$ (green triangle up), $8 \times 10^{14}\ cm^{-2}$ (yellow triangle down), $1 \times 10^{15}\ cm^{-2}$ (violet square), $2.5 \times 10^{15}\ cm^{-2}$ (pink diamond), $5 \times 10^{15}\ cm^{-2}$ (cyan hexagon), $1 \times 10^{16}\ cm^{-2}$ (gray star), $3 \times 10^{16}\ cm^{-2}$ (red crossed-circle) and $4 \times 10^{16}\ cm^{-2}$ (green crossed-square). Fits were performed assuming $L = 5\ nm$ and $\eta = 1.5°$. 101

4-9 Distributions of RDA (a) and BC (b) versus depth measured for UO_2 crystal implanted with Xe, La and Ce at low fluence ($\Phi \leq 1 \times 10^{15}\ cm^{-2}$) extracted from MC simulations. BC is parameterized by $L = 5\ nm$ and $\eta = 1.5°$. Fluences are measured in the unit of cm^{-2}. Xe, La and Ce implantation profiles calculated by SRIM (represented by filled area) are plotted in arbitrary unit. 103

4-10 Distributions of RDA (a) and BC (b) versus depth measured for UO_2 crystal implanted with Xe, La and Ce at medium ion fluence derived from MC simulations. BC is parameterized by $L = 5\ nm$ and $\eta = 1.5°$. Fluences are measured in the unit of cm^{-2}. Horizontal solid lines plotted on figure a represents the average of the maximum fraction of RDA calculated over the medium ion fluence range. Xe, La and Ce implantation profiles calculated by SRIM (represented by filled area) are plotted in arbitrary unit. 104

4-11 Distributions of RDA versus depth measured for UO_2 crystal implanted with Xe, La and Ce at high fluence derived from simulations. BC is parameterized by $L = 5\ nm$ and $\eta = 1.5°$. Fluences are measured in the unit of cm^{-2}. Xe, La and Ce implantation profiles calculated by SRIM (represented by filled area) are plotted in arbitrary unit. 105

4-12 Distributions of RDA versus depth measured for $Xe-$ implanted UO_2 crystal at very high fluence (corresponding to over 5 at. % of implanted Xe in the matrix) derived from simulations. BC is parameterized by $L = 5\ nm$ and $\eta = 1.5°$. Fluences are measured in the unit of cm^{-2}. Xe implantation profile calculated by SRIM (represented by filled area) is plotted in arbitrary unit. 107

4-13 Experimental angular scans (symbols) recorded across the main $\langle 100 \rangle$ axis for UO_2 single crystal implanted with La ions at $\Phi = 2 \times 10^{16}\ cm^{-2}$. The yields are normalized to random yield. The angular scans are integrated from 40 to 130 nm (red circle) and from 415 to 615 nm (blue star). Solid lines are the corresponding Monte-Carlo simulations of angular scans. All the dips are reproduced by the two-class model of defects where BC was characterised by the length and angle of $L = 5\ nm$ and $\eta = 1.5°$, respectively. 110

4-14 Evolutions of RDA extracted from channelling data by Monte-Carlo simulation for UO_2 crystals implanted with Xe (red circle), La (yellow square) and Ce (blue star) ions, respectively. 113

4-15 Fits to the evolution of RDA extracted from channelling spectra by MSDA model for UO_2 crystals irradiated with Xe (red circle), La (blue star) and Ce (yellow square). Solid, dashed and dash-dotted lines represent respectively the fits to the evolution of RDA. 114

4-16 Evolutions of BC extracted from channelling data by Monte-Carlo simulation for UO_2 crystals implanted with Xe (red circle), La (yellow square) and Ce (blue star). Fits were performed assuming $L = 5\ nm$ and $\eta = 1.5°$. 116

4-17 A comparison of the evolution of RDA and BC versus dpa and concentration. For the sake of clarity, the error bars are not shown on this figure. 117

List of Tables

1.1 Some selected physical properties. 12

1.2 Stopping power in UO_2 calculated by SRIM. 19

2.1 Summary of physical properties and relevant characteristics of implantations performed in UO_2 single crystals. Range and range straggling are calculated by SRIM program assuming the displacement thresholds for uranium and oxygen sub-lattices are $E_d(U) = 40\ eV$ and $E_d(0) = 20\ eV$, respectively [81]. The stopping power is calculated at indicated initial energy of ions The maximum *dpa* and concentration are calculated for highest expected fluence of $\Phi = 8 \times 10^{16}$ cm^{-2} 44

4.1 Fits to the evolution of RDA by the MSDA model. 115

Bibliography

[1] B. T. M. Willis. Structures of UO_2, UO_{2+x} and U_4O_9 by neutron diffraction. *Journal de Physique*, 25(5):431, 1964. 10

[2] H. Hausner. Determination of the melting point of uranium dioxide. *Journal of Nuclear Materials*, 15(3):179 – 183, 1965. 12

[3] P.W. Winter and D.A. MacInnes. A theoretical analysis of the electronic specific heat of solid urania. *Journal of Nuclear Materials*, 137(2):161 – 166, 1986. 12

[4] V.A. Kurepin. Thermodynamic properties of hyperstoichiometric urania in the UO_2-$UO_{2.25}$ solid solution range. *Journal of Nuclear Materials*, 303(1):65 – 72, 2002. 12

[5] M. Sheindlin, D. Staicu, C. Ronchi, L. Game-Arnaud, B. Remy, and A. Degiovanni. Experimental determination of the thermal conductivity of liquid UO_2 near the melting point. *Journal of Applied Physics*, 101(9):093508, 2007. 12

[6] J. Banerjee, S.C. Parida, T.R.G. Kutty, A. Kumar, and S. Banerjee. Specific heats of thoria urania solid solutions. *Journal of Nuclear Materials*, 427(1-3):69 – 78, 2012. 12

[7] B. Leclercq, R. Mévrel, V. Liedtke, and W. Hohenauer. Thermal conductivity of zirconia-based ceramics for thermal barrier coating. *Materialwissenschaft und Werkstofftechnik*, 34(4):406–409, 2003. 12

[8] C. Degueldre, P. Tissot, H. Lartigue, and M. Pouchon. Specific heat capacity and Debye temperature of zirconia and its solid solution. *Thermochimica Acta*, 403(2):267 – 273, 2003. 12

[9] AZOM. Zirconia - ZrO_2, Zirconium Dioxide. http://www.azom.com/properties.aspx?ArticleID=133. 12

[10] G. A. Slack. Thermal conductivity of MgO, Al_2O_3, $MgAl_2O_4$, and Fe_3O_4 crystals from 3 to 300 K. *Phys. Rev.*, 126:427–441, Apr 1962. 12

[11] R. Devanathan, N. Yu, K. E. Sickafus, and M. Nastasi. Structure and mechanical properties of irradiated magnesium aluminate spinel. *Journal of Nuclear Materials*, 232(1):59 – 64, 1996. 12

[12] Stephan Klemme and Martin Ahrens. Low-temperature heat capacities of $MgAl_2O_4$ and spinels of the $MgCr_2O_4$-$MgAl_2O_4$ solid solution. *Physics and Chemistry of Minerals*, 34(2):59–72, 2007. 12

[13] St. Burghartz and B. Schulz. Thermophysical properties of sapphire, AlN and $MgAl_2O_4$ down to 70 K. *Journal of Nuclear Materials*, 212 - 215, Part B(0):1065 – 1068, 1994. 12

[14] H.G. Scott. Phase relationships in the zirconia-yttria system. *Journal of Materials Science*, 10(9):1527–1535, 1975. 13, 131

[15] S. T. Murphy, C. A. Gilbert, R. Smith, T. E. Mitchell, and R. W. Grimes. Non-stoichiometry in $MgAl_2O_4$ spinel. *Philosophical Magazine*, 90(10):1297–1305, 2010. 12, 13

[16] K. E. Sickafus, J. M. Wills, and N. W. Grimes. Structure of spinel. *Journal of the American Ceramic Society*, 82(12):3279 – 3292, 1999. 12, 13

[17] K. D. Rouse, M. W. Thomas, and B. T. M. Willis. Space group of the spinel structure: A neutron diffraction study of $MgAl_2O_4$. *Journal of Physics C: Solid State Physics*, 9(9):L231, 1976. 13

[18] D. Schmidtmeier, G. Büchel, and A. Buhr. Magnesium aluminate spinel raw materials for high performance refractories for steel ladles. *Materiały Ceramiczne/Ceramic Materials*, 61 issue 4:223 – 227, 2009. 13

[19] B. M. Penetrante, J. N. Bardsley, D. DeWitt, M. Clark, and D. Schneider. Evolution of ion-charge-state distributions in an electron-beam ion trap. *Phys. Rev. A*, 43:4861 – 4872, May 1991. 18

[20] V. E. Anderson, R. H. Ritchie, C. C. Sung, and P. B. Eby. Relativistic corrections to stopping powers. *Phys. Rev. A*, 31:2244–2247, Apr 1985. 19

[21] H. A. Bethe. *Ann. Phys. (Leipz.), 5*, page 325, 1930. 20

[22] F. Bloch. *Ann. Phys. (Leipz.), 16*, page 285, 1933. 20

[23] B. S. Yarlagadda, J. E. Robinson, and W. Brandt. Effective-charge theory and the electronic stopping power of solids. *Phys. Rev. B*, 17:3473 – 3483, May 1978. 21

[24] N. Bohr. Scattering and stopping of fission fragments. *Phys. Rev.*, 58:654 – 655, Oct 1940. 21

[25] N. Bohr. Velocity-range relation for fission fragments. *Phys. Rev.*, 59:270 – 275, Feb 1941. 21

[26] W. E. Lamb. Passage of uranium fission fragments through matter. *Phys. Rev.*, 58:696 – 702, Oct 1940. 21

[27] W. Brandt and M. Kitagawa. Effective stopping-power charges of swift ions in condensed matter. *Phys. Rev. B*, 25:5631 – 5637, May 1982. 21

[28] J. Lindhard and M. Scharff. Energy dissipation by ions in the keV region. *Phys. Rev.*, 124:128 – 130, Oct 1961. 21

[29] O. B. Firsov. *Zh. Eksp. Teor. Fiz. [Engl. transl. Sov. Phys. JETP 5, p1192-1196(1957)]*, 32:1464, 1957. 21

[30] O. B. Firsov. *Zh. Eksp. Teor. Fiz. [Engl. transl. Sov. Phys. JETP 6, p5340-537(1958)]*, 33:696, 1957. 21

[31] O. B. Firsov. *Zh. Eksp. Teor. Fiz. [Engl. transl. Sov. Phys. JETP 7, 308- 311(1958)]*, 34:447, 1958. 21

[32] O. B. Firsov. *Zh. Eksp. Teor. Fiz. [Engl. transl. Sov. Phys. JETP 9, 1076-1080(1959)]*, 36:1517, 1959. 21

[33] G. H. Kinchin and R. S. Pease. The displacement of atoms in solids by radiation. *Reports on Progress in Physics*, 18(1):1, 1955. 22

[34] M. Toulemonde, C. Dufour, and E. Paumier. Transient thermal process after a high-energy heavy-ion irradiation of amorphous metals and semiconductors. *Phys. Rev. B*, 46:14362 – 14369, Dec 1992. 24

[35] T. Wiss, Hj. Matzke, C. Trautmann, M. Toulemonde, and S. Klaumünzer. Radiation damage in UO_2 by swift heavy ions. *Nuclear Instruments and Methods in Physics Research Section B: Beam Interactions with Materials and Atoms*, 122(3):583 – 588, 1997. 24, 36, 37, 131

[36] R. L. Fleischer, P. B. Price, and R. M. Walker. Ion explosion spike mechanism for formation of charged-particle tracks in solids. *J. Appl. Phys.*, 36:3645 – 3652, 1965. 24

[37] I. M. Lifshits, M. I. Kaganov, and L. V. Tanatarov. On the theory of radiation-induced changes in metals. *Journal of Nuclear Energy. Part A. Reactor Science*, 12(1 - 2):69 – 78, 1960. 24

[38] M. C. Wittels, J. O. Stiegler, and F. A. Sherrill. Radiation effects in uranium-doped zirconia. *Journal of Nuclear Energy. Parts A/B. Reactor Science and Technology*, 16(5):237 – 244, 1962. 26

[39] K. E. Sickafus, Hj. Matzke, Th. Hartmann, K. Yasuda, J. A. Valdez, P. Chodak III, M. Nastasi, and R. A. Verrall. Radiation damage effects in zirconia. *Journal of Nuclear Materials*, 274(1-2):66 – 77, 1999. 26, 27, 131

[40] N. Yu, K. E. Sickafus, P. Kodali, and M. Nastasi. In situ observation of defect growth beyond the irradiated region in yttria-stabilized zirconia induced by 400 keV xenon ion-beam at -90 and 30°C. *Journal of Nuclear Materials*, 244(3):266 – 272, 1997. 27, 28, 122, 131

[41] D. Z. Xie, D. Z. Zhu, D. X. Cao, and Z. Y. Zhou. A study of single crystal zirconia implanted with platinum ions. *Nuclear Instruments and Methods in Physics Research Section B: Beam Interactions with Materials and Atoms*, 132(3):425 – 429, 1997. 27

[42] K. E. Sickafus, H. Matzke, K. Yasuda, P. Chodak, R. A. Verrall, P. G. Lucuta, H. R. Andrews, A. Turos, R. Fromknecht, and N. P. Baker. Radiation damage effects in cubic-stabilized zirconia irradiated with 72 MeV I^+ ions. *Nuclear Instruments and Methods in Physics Research Section B: Beam Interactions with Materials and Atoms*, 141(1-4):358 – 365, 1998. 28

[43] L. M. Wang, S. X. Wang, and R. C. Ewing. Amorphization of cubic zirconia by caesium-ion implantation. *Philosophical Magazine Letters*, 80(5):341 – 347, 2000. 28, 30, 39

[44] I. V. Afanasyev-Charkin and K. E. Sickafus. Effect of sputtering in Xe ion irradiated yttria-stabilized zirconia. *Journal of Nuclear Materials*, 306(2-3):112 – 120, 2002. 29

[45] K. Yasuda, C. Kinoshita, S. Matsumura, and A. I. Ryazanov. Radiation-induced defect clusters in fully stabilized zirconia irradiated with ions and/or electrons. *Journal of Nuclear Materials*, 319(0):74 – 80, 2003. 29

[46] T. Hojo, H. Yamamoto, J. Aihara, S. Furuno, K. Sawa, T. Sakuma, and K. Hojou. Radiation effects on yttria-stabilized zirconia irradiated with He or Xe ions at high temperature. *Nuclear Instruments and Methods in Physics Research Section B: Beam Interactions with Materials and Atoms*, 241(1 - 4):536 – 542, 2005. 29

[47] L. Thomé, J. Fradin, J. Jagielski, A. Gentils, S. E. Enescu, and F. Garrido. Radiation damage in ion-irradiated yttria-stabilized cubic zirconia single crystals. *The European Physical Journal Applied Physics*, 24:37–48, 2003. 29

[48] J. Jagielski, A. Gentils, L. Thomé, L. Nowicki, F. Garrido, and S. Klaumünzer. Channeling study of the damage induced in zirconia irradiated with high-energy

heavy ions. *Nuclear Instruments and Methods in Physics Research Section B: Beam Interactions with Materials and Atoms*, 219-220(0):626 – 630, 2004. 30

[49] A. Gentils, L. Thomé, J. Jagielski, L. Nowicki, S. Klaumünzer, F. Garrido, and M. Beauvy. Damage production in cubic zirconia irradiated with swift heavy ions. *Nuclear Instruments and Methods in Physics Research Section B: Beam Interactions with Materials and Atoms*, 218(0):457 – 460, 2004. 30

[50] S. Moll, L. Thomé, F. Garrido, L. Vincent, G. Sattonnay, J-M. Costantini, J. Jagielski, A. Benyagoub, and M. Behar. Radiation effects in yttria-stabilized zirconia: Comparison between nuclear and electronic processes. *Nuclear Instruments and Methods in Physics Research Section B: Beam Interactions with Materials and Atoms*, 266(12-13):3048 – 3051, 2008. 30

[51] F. W. Clinard-Jr., G. F. Hurley, and L. W. Hobbs. Neutron irradiation damage in MgO, Al_2O_3 and $MgAl_2O_4$ ceramics. *Journal of Nuclear Materials*, 108 - 109(0):655 – 670, 1982. 31

[52] K. E. Sickafus, A. C. Larson, N. Yu, M. Nastasi, G. W. Hollenberg, F. A. Garner, and R. C. Bradt. Cation disorder in high dose, neutron-irradiated spinel. *Journal of Nuclear Materials*, 219(0):128 – 134, 1995. 31

[53] K. E. Sickafus, N. Yu, and M. Nastasi. Radiation resistance of the oxide spinel: the role of stoichiometry on damage response. *Nuclear Instruments and Methods in Physics Research Section B: Beam Interactions with Materials and Atoms*, 116(1-4):85 – 91, 1996. 31

[54] M. Ishimaru, Y. Hirotsu, I. V. Afanasyev-Charkin, and K. E. Sickafus. Atomistic structures of metastable and amorphous phases in ion-irradiated magnesium aluminate spinel. *Journal of Physics: Condensed Matter*, 14(6):1237, 2002. 31

[55] S. J. Zinkle and V. A Skuratov. Track formation and dislocation loop interaction in spinel irradiated with swift heavy ions. *Nuclear Instruments and Methods in Physics Research Section B: Beam Interactions with Materials and Atoms*, 141(14):737 – 746, 1998. 31

[56] N. Kishimoto, Y. Takeda, N. Umeda, V. T. Gritsyna, C. G. Lee, and T. Saito. Metal nanocrystal formation in magnesium aluminate spinel and silicon dioxide with high-flux Cu^- ions. *Nuclear Instruments and Methods in Physics Research Section B: Beam Interactions with Materials and Atoms*, 166 - 167(0):840 – 844, 2000. 32

[57] T. Soeda, S. Matsumura, C. Kinoshita, and N. J. Zaluzec. Cation disordering in magnesium aluminate spinel crystals induced by electron or ion irradiation. *Journal of Nuclear Materials*, 283-287, Part 2(0):952 – 956, 2000. 32

[58] C. G. Lee, Y. Takeda, and N. Kishimoto. Disordering and annealing effects of magnesium aluminate spinel implanted with high-flux 60 keV Cu^-. *Nuclear Instruments and Methods in Physics Research Section B: Beam Interactions with Materials and Atoms*, 191(1-4):591 – 595, 2002. 32

[59] M. Shimada, S. Matsumura, K. Yasuda, C. Kinoshita, Y. Chimi, N. Ishikawa, and A. Iwase. Radiation-induced disordering in magnesium aluminate spinel subjected to ionizing radiation. *Journal of Nuclear Materials*, 329333, Part B(0):1446 – 1450, 2004. 33

[60] T. Yamamoto, M. Shimada, K. Yasuda, S. Matsumura, Y. Chimi, and N. Ishikawa. Microstructure and atomic disordering of magnesium aluminate spinel irradiated with swift heavy ions. *Nuclear Instruments and Methods in Physics Research Section B: Beam Interactions with Materials and Atoms*, 245(1):235 – 238, 2006. 33

[61] L. Thomé, J. Jagielski, A. Gentils, L. Nowicki, and F. Garrido. Quantitative analysis of radiation-induced disorder in spinel crystals. *Nuclear Instruments and Methods in Physics Research Section B: Beam Interactions with Materials and Atoms*, 242(12):643 – 645, 2006. 33

[62] J. Jagielski and L. Thomé. Accumulation of radiation damage in spinel crystals: Quantitative analysis and interpretation of RBS/C data. *Nuclear Instruments and Methods in Physics Research Section B: Beam Interactions with Materials and Atoms*, 261(12):1155 – 1158, 2007. 33

[63] S. E. Enescu, L. Thomé, A. Gentils, F. Garrido, and T. Thomé. High-temperature behavior of zirconia and spinel doped with cesium. *Nuclear Instruments and Methods in Physics Research Section B: Beam Interactions with Materials and Atoms*, 242(1-2):409 – 412, 2006. 33

[64] K. Yasuda, T. Yamamoto, S. Seki, K. Shiiyama, and S. Matsumura. Production and stability of radiation-induced defects in $MgAl_2O_4$ under electronic excitation. *Nuclear Instruments and Methods in Physics Research Section B: Beam Interactions with Materials and Atoms*, 266(1213):2834 – 2841, 2008. 33

[65] A. D. Whapham and B. E. Sheldon. Radiation damage in uranium dioxide. *Philosophical Magazine*, 12(120):1179–1192, 1965. 34

[66] X. F. Tian, T. Gao, C. Long, J. Li, G. Jiang, and H. Xiao. Dynamical simulations of radiation damage induced by 10 keV energetic recoils in UO_2. *Nuclear Instruments and Methods in Physics Research Section B: Beam Interactions with Materials and Atoms*, 269(15):1771 – 1776, 2011. 34

[67] K. Nogita and K. Une. High resolution TEM of high burnup UO_2 fuel. *Journal of Nuclear Materials*, 250(2 - 3):244 – 249, 1997. 34

[68] K. Nogita, K. Hayashi, K. Une, and K. Fukuda. Depth profiles of damage accumulation in UO_2 and $(U,Gd)O_2$ pellets irradiated with 100 MeV iodine ions. *Journal of Nuclear Materials*, 273(3):302 – 309, 1999. 34

[69] T. Sonoda, M. Kinoshita, N. Ishikawa, M. Sataka, A. Iwase, and K. Yasunaga. Clarification of high density electronic excitation effects on the microstructural evolution in UO_2. *Nuclear Instruments and Methods in Physics Research Section B: Beam Interactions with Materials and Atoms*, 268(19):3277 – 3281, 2010. 35, 131

[70] T. Sonoda, M. Kinoshita, I. L. F. Ray, T. Wiss, H. Thiele, D. Pellottiero, V. V. Rondinella, and Hj. Matzke. Transmission electron microscopy observation on irradiation-induced microstructural evolution in high burn-up UO_2 disk fuel. *Nuclear Instruments and Methods in Physics Research Section B: Beam Interactions with Materials and Atoms*, 191(1-4):622 – 628, 2002. 35, 123

[71] Hj. Matzke, P. G. Lucuta, and T. Wiss. Swift heavy ion and fission damage effects in UO_2. *Nuclear Instruments and Methods in Physics Research Section B: Beam Interactions with Materials and Atoms*, 166 - 167(0):920 – 926, 2000. 36

[72] F. Garrido, C. Choffel, J.-C. Dran, L. Thomé, L. Nowicki, and A. Turos. Structural modifications in uranium dioxide irradiated with swift heavy ions. *Nuclear Instruments and Methods in Physics Research Section B: Beam Interactions with Materials and Atoms*, 127 - 128(0):634 – 638, 1997. 36

[73] F. Garrido, S. Moll, G. Sattonnay, L. Thomé, and L. Vincent. Radiation tolerance of fluorite-structured oxides subjected to swift heavy ion irradiation. *Nuclear Instruments and Methods in Physics Research Section B: Beam Interactions with Materials and Atoms*, 267(8-9):1451 – 1455, 2009. 37

[74] F. Garrido, L. Vincent, L. Nowicki, G. Sattonnay, and L. Thomé. Radiation stability of fluorite-type nuclear oxides. *Nuclear Instruments and Methods in Physics Research Section B: Beam Interactions with Materials and Atoms*, 266(12 - 13):2842 – 2847, 2008. 37

[75] B.J. Lewis. Fission product release from nuclear fuel by recoil and knockout. *Journal of Nuclear Materials*, 148(1):28 – 42, 1987. 38

[76] L. V. Brutzel, M. Rarivomanantsoa, and D. Ghaleb. Displacement cascade initiated with the realistic energy of the recoil nucleus in UO_2 matrix by molecular dynamics simulation. *Journal of Nuclear Materials*, 354(13):28 – 35, 2006. 38, 131

[77] C. Sabathier, L. Vincent, P. Garcia, F. Garrido, G. Carlot, L. Thome, P. Martin, and C. Valot. In situ tem study of temperature-induced fission product precipitation in UO_2. *Nuclear Instruments and Methods in Physics Research Section B: Beam Interactions with Materials and Atoms*, 266(12-13):3027 – 3032, 2008. 38, 39, 123

[78] A. Michel, C. Sabathier, G. Carlot, O. Kaïtasov, S. Bouffard, P. Garcia, and C. Valot. An in situ TEM study of the evolution of Xe bubble populations in UO_2. *Nuclear Instruments and Methods in Physics Research Section B: Beam Interactions with Materials and Atoms*, 272(0):218 – 221, 2012. 39, 123

[79] B. Marchand, N. Moncoffre, Y. Pipon, N. Bérerd, C. Garnier, L. Raimbault, P. Sainsot, T. Epicier, C. Delafoy, M. Fraczkiewicz, C. Gaillard, N. Toulhoat, A. Perrat-Mabilon, and C. Peaucelle. Xenon migration in UO_2 under irradiation studied by SIMS profilometry. *Journal of Nuclear Materials*, 440(13):562 – 567, 2013. 39, 123

[80] Hj. Matzke and C. Ronchi. Precipitation of Xe and Cs into bubbles, kinetics of bubble migration and alternative release processes. *Eur. Appl. Res. Rep. Nucl. Sci. Technol.*, 5(6):1105–1158, 1984. 39

[81] J. Soullard. High voltage electron microscope observations of UO_2. *Journal of Nuclear Materials*, 135(2 - 3):190 – 196, 1985. 43, 44, 68, 137

[82] Frédérico Garrido, Lech Nowicki, and Lionel Thomé. Channeling investigation of the crystalline structure of U_4O_{9-y}. *Phys. Rev. B*, 74:184114, Nov 2006. 44

[83] L. C. Feldman, J. W. Mayer, and S. T. Picraux. *Materials Analysis by Ion Channeling: Submicron Crystallography*. Academic Press, New York, 1982. 44

[84] Pathak. Study of crystal defects using ion channeling and channeling radiation. *Bull Mater. Sci.*, 10:105, 1988. 44

[85] L. Shao and M. Nastasi. Methods for the accurate analysis of channeling rutherford backscattering spectrometry. *Applied Physics Letters*, 87:064103, 2005. 44

[86] M. L. Swanson. The study of lattice defects by channelling. *Report on Progress in Physics*, 45:47–93, 1982. 44

[87] M. L. Swanson, L. M. Howe, T. E. Jackman, and J. A. Moore. Channeling studies of defects. *Nuclear Instruments and Methods*, 194:165, 1982. 44

[88] L. Thomé, S. Moll, A. Debelle, F. Garrido, G. Sattonnay, and J. Jagielski. Use of channeling for the study of radiation effects in nuclear materials. *Nuclear Instruments and Methods in Physics Research Section B: Beam Interactions with Materials and Atoms*, 290(0):6 – 12, 2012. 44

[89] W. K. Chu, J. W. Mayer, and M. A. Nicolet. *Backscattering spectrometry*. Academic Press, 1978. 45

[90] B. Blanpain, P. Revesz, L. R. Doolittle, K. H. Purser, and J. W. Mayer. The use of the 3.05 MeV oxygen resonance for ^{4}He backscattering near-surface analysis of oxygen-containing high Z compounds. *Nuclear Instruments and Methods in Physics Research Section B: Beam Interactions with Materials and Atoms*, 34(4):459 – 464, 1988. 46

[91] L. Thomé, A. Gentils, J. Jagielski, S. E. Enescu, and F. Garrido. On the use of the ^{16}O(^{4}He,^{4}He)^{16}O resonance for the evaluation of radiation damage in oxides. *Nuclear Instruments and Methods in Physics Research Section B: Beam Interactions with Materials and Atoms*, 219-220(0):99 – 104, 2004. 46

[92] J. R. Tesmer, M. Nastasi, J. C. Barbour, C. J. Maggiore, and J. W. Mayer. *Handbook of Modern Ion Beam Materials Analysis*. Materials Research Society, Pittsburgh, 1994. 48

[93] A. Turos, L. Nowicki, A. Stonert, K. Pagowska, J. Jagielski, and A. Muecklich. Monte carlo simulations of ion channeling in crystals containing extended defects. *Nuclear Instruments and Methods in Physics Research Section B: Beam Interactions with Materials and Atoms*, 268(11-12):1718 – 1722, 2010. 56

[94] P. J. M. Smulders and D. O. Boerma. Computer simulation of channeling in single crystals. *Nuclear Instruments and Methods in Physics Research section B*, 29:471–489, 1987. 56

[95] J. Jagielski, A. Turos, L. Nowicki, P. Jozwik, S. Shutthanandan, Y. Zhang, N. Sathish, L. Thomé, A. Stonert, and I. Jozwik-Biala. Monte carlo simulations of channeling spectra recorded for samples containing complex defects. *Nuclear Instruments and Methods in Physics Research Section B: Beam Interactions with Materials and Atoms*, 273(0):91 – 94, 2012. 56

[96] L. R. Doolittle. Algorithms for the rapid simulation of rutherford backscattering spectra. *Nuclear Instruments and Methods in Physics Research Section B: Beam Interactions with Materials and Atoms*, 9(3):344 – 351, 1985. 56

[97] John H. Barrett. Monte carlo channeling calculations. *Phys. Rev. B*, 3:1527–1547, Mar 1971. 56

[98] John H. Barrett. Methods of channeling simulation. *Nuclear Instruments and Methods in Physics Research Section B: Beam Interactions with Materials and Atoms*, 44(3):367 – 372, 1990. 57

[99] James F. Ziegler and Jochen P. Biersack. The stopping and range of ions in matter. In D.Allan Bromley, editor, *Treatise on Heavy-Ion Science*. Springer US, 1985. 58

[100] L. Nowicki, A. Turos, R. Ratajczak, A. Stonert, and F. Garrido. Modern analysis of ion channeling data by Monte-Carlo simulations. *Nuclear Instruments and Methods in Physics Research section B*, 240:277–282, 2005. 58

[101] E. Bøgh. Defect studies in crystals by means of channeling. *Canadian Journal of Physics*, 46(6):653–662, 1968. 61

[102] G. F. Cerofolini, F. Corni, G. Ottaviani, and R. Tonini. A fast technique for the quantitative analysis of channeling RBS spectra. *Nuclear Instruments and Methods in Physics Research Section B: Beam Interactions with Materials and Atoms*, 71(4):441 – 444, 1992. 62

[103] H. Kleykamp. The chemical state of the fission products in oxide fuels. *Journal of Nuclear Materials*, 131(2 - 3):221 – 246, 1985. 67, 123

[104] P. H. Dederichs. The theory of diffuse X-ray scattering and its application to the study of point defects and their clusters. *Journal of Physics F: Metal Physics*, 3(2):471, 1973. 74

[105] A. Debelle, A. Declémy, L. Vincent, F. Garrido, and L. Thomé. XRD contribution to the study of Cs-implanted cubic zirconia. *Journal of Nuclear Materials*, 396(2-3):240 – 244, 2010. 74, 76

[106] A. Debelle, A. Boulle, F. Garrido, and L. Thomé. Strain and stress build-up in He-implanted UO_2 single crystals; an x-ray diffraction study. *Journal of Materials Science*, 46:4683–4689, 2011. 74, 79

[107] S. Moll, L. Thomé, G. Sattonnay, A. Debelle, F. Garrido, L. Vincent, and J. Jagielski. Multistep damage evolution process in cubic zirconia irradiated with mev ions. *Journal of Applied Physics*, 106(7):073509, 2009. 74

[108] G. Sattonnay, S. Moll, M. Herbst-Ghysel, C. Legros, J.-M. Costantini, and L. Thomé. Mechanical stresses induced in ceramic oxides by ion irradiation. *Nuclear Instruments and Methods in Physics Research Section B: Beam Interactions with Materials and Atoms*, 266(12-13):3052 – 3056, 2008. 74

[109] S. I. Rao and C. R. Houska. The measurement of elastic stresses and energy in cubic single-crystal films by x-ray diffraction. *J. Appl. Phys.*, 52:6322, 1981. 76, 77

[110] A. Debelle and A. Declémy. XRD investigation of the strain/stress state of ion-irradiated crystals. *Nuclear Instruments and Methods in Physics Research Section B: Beam Interactions with Materials and Atoms*, 268(9):1460 – 1465, 2010. 76, 77

[111] J. B. Wachtman-Jr., M. L. Wheat, H. J. Anderson, and J. L. Bates. Elastic constants of single crystal UO_2 at 25°C. *Journal of Nuclear Materials*, 16(1):39 – 41, 1965. 77

[112] A. Debelle, A. Boulle, F. Rakotovao, J. Moeyaert, C. Bachelet, F. Garrido, and L Thomé. Influence of elastic properties on the strain induced by ion irradiation in crystalline materials. *Journal of Physics D: Applied Physics*, 46(4):045309, 2013. 77, 80

[113] A. W. Pryor. Thermal vibration amplitudes in fluorite lattices. *Journal of Physics and Chemistry of Solids*, 26(12):2045 – 2049, 1965. 91

[114] F. Garrido, L. Nowicki, A. Stonert, A. Pietraszko, and E. Wendler. ^{4}He channelling studies of U_4O_9. *Nuclear Instruments and Methods in Physics Research Section B: Beam Interactions with Materials and Atoms*, 249(1 - 2):497 – 500, 2006. 91

[115] G. Dolling, R. A. Cowley, and A. D. B. Woods. The crystal dynamics of uranium dioxide. *Canadian Journal of Physics*, 43(8):1397–1413, 1965. 91

[116] J. Jagielski and L. Thomé. Multi-step damage accumulation in irradiated crystals. *Applied Physics A*, 97(1):147–155, 2009. 113

[117] John Emsley. *The Elements*. Oxford chemistry guides. Oxford University Press, Incorporated, 3 edition, June 1998. 123

[118] H. Matzke. Fission gases in nuclear fuels. *Annales de chimie*, 14(1-2):133, 1989. 123

[119] C. Baker. The fission gas bubble distribution in uranium dioxide from high temperature irradiated SGHWR fuel pins. *Journal of Nuclear Materials*, 66(3):283 – 291, 1977. 123

[120] K. Nogita and K. Une. High resolution TEM observation and density estimation of Xe bubbles in high burnup UO_2 fuels. *Nuclear Instruments and Methods in Physics*

Research Section B: Beam Interactions with Materials and Atoms, 141(1 - 4):481 – 486, 1998. 123

[121] Takeo Fujino. Thermodynamics of fluorite type solid solutions containing plutonium, lanthanide elements or alkaline earth metals in uranium dioxide host lattices. *Journal of Nuclear Materials*, 154(1):14 – 24, 1988. 123

[122] R. W. Grimes and C. R. A. Catlow. The stability of fission products in uranium dioxide. *Philosophical Transactions: Physical Sciences and Engineering*, 335(1639):609 – 634, 1991. 123

[123] H. G. Diehl and C. Keller. Das system UO_2-UO_3-$LaO_{1.5}$. *Journal of Solid State Chemistry*, 3(4):621 – 636, 1971. 123

[124] L. Gmelin, L. Berg, R. Keim, Gmelin-Institut für anorganische Chemie (Frankfurt am Main), and Deutsche chemische Gessellschaft (Berlin). *Gmelin handbuch der anorganischen chemie: U, Uran. Ternére und polynére oxide des urans. systemnummer 55. Erbd. T. C3.* Gmelin Handbuch der anorganischen Chemie. Springer-Verlag, 1975. 123

[125] G. Brillant, F. Gupta, and A. Pasturel. Fission products stability in uranium dioxide. *Journal of Nuclear Materials*, 412(1):170 – 176, 2011. 123

[126] S. Imoto. Chemical state of fission products in irradiated UO_2. *Journal of Nuclear Materials*, 140(1):19 – 27, 1986. 123

[127] R. W. Grimes, R. G. J. Ball, and C. R. A. Catlow. Site preference and binding of iodine and caesium in uranium dioxide. *Journal of Physics and Chemistry of Solids*, 53(4):475 – 484, 1992. 123

[128] A. Turos, Hj. Matzke, and O. Meyer. Lattice location of fission products in UO_2 single crystals. *Nuclear Instruments and Methods in Physics Research Section B: Beam Interactions with Materials and Atoms*, 65(1 - 4):315 – 318, 1992. 123